2020

Investigating intraplate seismicity in the Central and Eastern US: Linking observations and numerical models

Arushi Saxena

Recommended Citation

Saxena, Arushi, "Investigating intraplate seismicity in the Central and Eastern US: Linking observations and numerical models" (2020). *Electronic Theses and Dissertations*. 2755.
https://digitalcommons.memphis.edu/etd/2755

INVESTIGATING INTRAPLATE SEISMICITY IN THE CENTRAL AND EASTERN US: LINKING OBSERVATIONS AND NUMERICAL MODELS

by

Arushi Saxena

A Dissertation

Submitted in Partial Fulfillment of the

Requirements for the Degree of

Doctor of Philosophy

Major: Earth Sciences
Concentration: Geophysics

The University of Memphis

May 2020

-This work is dedicated to my friends and family for their constant love and support.

Acknowledgments

My journey through Ph.D. would not have been possible without the help of others.

First, I want to extend my sincere gratitude to my advisor, Dr. Eunseo Choi, for planting the seed of interest for geodynamics in me, for showing tremendous patience whenever I was stuck in my research, for always lending an open ear to my questions, and for unfaltering support throughout these years. He maintained a perfect balance between giving me independence in my projects and, at the same time, nudging me in the right direction. He always encouraged me to attend conferences and workshops, which exposed me to various research groups and ideas, and made me confident to present my research work. He has mentored me not only in my research projects but also in my career goals. I have learned a lot from his innovative teaching style and research outlook regarding open-source practices and data sharing. Thank you, Eunseo, for mentoring my work and instilling scientific qualities in me.

I would also like to thank my co-advisors, Dr. Christine Powell "Chris," and Dr. Charles Langston "Chuck." I have closely worked with Chris on most of my research projects. She has guided me on observation seismology and geology, whenever I was lost in my research. As a graduate student advisor, she has always been very empathetic and advocated for any student's needs. She has a calm and caring influence, which has de-stressed me in my most difficult times. She is one of the most humble scientists I have ever met. She has her unique and fun presentation style, which I have always admired and wished to incorporate in myself. Thank you, Chris, for all your help and your motivation all these years. I also worked on a project with Chuck. He is full of new and exciting research ideas on almost everything related to seismology. Although at first, I was intimidated by the "Langston" expressions, I soon realized that he is very approachable and helpful. I have always been amazed at how he could remember the tiniest detail about my project while juggling administration duties as the head of the department, and

advising a dozen students. Thank you, Chuck, for spending time and effort in explaining to me the most basic concepts of seismology whenever I needed them.

Thanks to my other committee members, Dr. Robert Smalley"Bob" and Dr. Randel Cox "Randy", for always supporting me and sharing their publishing and research experiences. Bob- I always enjoyed listening to you on physics, airplanes and Antarctica. You are filled with interesting facts on almost everything. Also, thank you, for giving me the opportunity to use your glider. Thank you, Randy, for encouraging me and helping me with my problems on geology.

I want to thank all the present CERI faculty members for teaching me various aspects of geophysics, and always keeping their offices open for any question. I have learned a lot from all of their courses and discussions. I also want to thank the emeritus faculty, Dr. Arch Johnson and Dr. James Dorman, for the talks about the history of the department and seminar on moonquakes. It has been my sincere honor to interact with you both. Also, thank you, faculty, for sponsoring the coffee hours at CERI, it was a refreshing time away from my research into another scientific research conversation.

I also want to thank my undergraduate professors for laying the foundation of geophysics in me, and giving me an opportunity to present my research.

A special thanks to the CERI staff for managing all the CERI seismic networks and always willing to help the students. Thank you for all your kindness and for making the students feel at home. Thank you, Kent Moran, for playfully pulling my leg to work hard and for all the engaging conversations. Thank you, Gary Patterson, for always being so welcoming and sharing your garden produce with the students. I also want to thank Michelle Smith "Michelle" for all the administrative help throughout these years. Thank you, Michelle, for spreading your infectious laugh and helping me during these years.

I want to thank CERI for providing me the research assistance and travel support to conferences all through these years.

I also want to acknowledge the high performance computing resources provided by the University of Memphis.

The geodynamic codes used in the majority of my projects were developed and supported by the Computational Infrastructure of Geodynamics. Thank you for making these codes open-source, and funding the various workshops and hackathons. Through these workshops, I learned how to use and modify them for my research. I would particularly like to thank the developers of PyLith and Aspect for being extremely responsive whenever I was stuck with technical issues in these codes.

The tomography used in two of my projects was provided by Dr. Cecilia Nyamwandha and Dr. Berk Biryol. Thank you for making your work available to me.

Thanks to my office mates, Jerome “Jerry” Kutliroff, and Oluwaseun Fadugba. Jerry- you have always patiently listened to me whenever I had moments of self-doubts. Oluwaseun- you are one of my great friends in CERI. We shared many courses, workshops, and the different milestones of the Ph.D. in CERI. You have a very calm demeanor, which has encouraged me to persevere in my difficult times.

Thanks to all my friends I made at CERI. Khurram Aslam- you and your family have always made me felt at home. Thank you for sharing your lunch almost every day and for all the discussions on machine learning and life that came up during the lunch. You are a great researcher and a great friend. Hee Choi- you made the two years in my journey extra fun. You are funny, helpful, and smart. Thank you for all the after-work times we spent together. I hope that our paths as numerical modelers will cross soon. Elizabeth Gilmor- thank you for being there through the gym, swimming, and climbing sessions. I am glad to know you and Bivu during my stay in Memphis. Chunyu Liu- thank you for participating in all the outdoor activities with me, you are a great friend to have. Thank you, Oluwaseyi Bolarinwa, for all the fun breaks in CERI. And a further thanks to all my other friends, and students at CERI for being wonderful fellows- Sabber Ahamed, Roshan Bhattarai, Urbi Basu, Benjamin Gemballa, Yu Geng, Chloe Glover, Naeem Khoshnevis, Monsurul Huda, Ariful Islam, Hao Lu, Christopher Marlow, Philip Ogweno, Sandaruwan Ratnayake, Shima Azizzadeh-Roodpish, Trevor Satterfield, Jiayan Tan, Yang Yang, Jia Zhang, and Yixin Zhang.

A special thanks to my friends outside Memphis, my best friends-Shivani Gupta, and Pranshu Ratre. Shivani- you are amazing! Thank you for always being there in my life's ups and downs, near or far. You have been very honest about your opinions, which continues to motivate me to be a better person. Pranshu- you are simply awesome. I am lucky to be able to share my research and life problems with you. You have been so supportive and encouraging throughout these years, thank you! I also want to thank my friends from Nigeria- Rohit Chaurasia and Rituparana Raha. You both rooted for me when I decided to get a Ph.D., and I am grateful for that.

I want to thank my fiancè, Aaron Van Alstine, for making the last year of this journey cherished. I was studying geophysics, but he taught me about rocks. I look forward to years of learning more from you.

Lastly, I want to thank my parents, Alka Saxena and Rakesh Saxena, and my brother, Ekansh Saxena, for showering me with their love and blessings. I am very fortunate to have you all in my life. You have made me who I am today.

To all the other people I did not have room to thank here, you know who you are.

PREFACE

Chapter 2 of this dissertation is based on the manuscript submitted to Journal of Geophysical Research, Solid Earth.

Saxena, A., Choi, E., Powell, C. and Langston, C. "Possible orthopyroxene enrichment in the upper mantle below the Mississippi Embayment"

Chapter 3 of this dissertation is based on the manuscript submitted to Geophysical Journal International.

Saxena, A., Choi, E., Powell, C. and Aslam, K. (in-review). "Stress concentration in the Central and Southeastern US seismic zones due to upper mantle heterogeneity"

Chapter 4 of this dissertation is completed for submission to Journal of Geophysical Research, Solid Earth.

Saxena, A. and Langston, C. "Detecting lithospheric discontinuities beneath the Mississippi Embayment using S wave receiver functions"

Chapter 5 of this dissertation is under preparation for submission.

Saxena, A., Choi, E. and Powell, C. "A possible geodynamic model to explain the observed Pn anisotropy beneath the New Madrid seismic zone"

ABSTRACT

Earthquakes far from the plate boundaries pose a significant hazard to human life, and damage to property. Intraplate seismicity has piqued interest among many researchers to understand the risks associated with it. Several models have been proposed to explain seismicity in regions far from the influence of tectonic stresses, the nature of which depends on the depth and time scale of the geological process invoked in the model. However, these mechanisms are debatable and often require revision compatible with new observations.

The Central and Eastern US (CEUS) is an ideal location for investigating intraplate seismicity. The CEUS hosts numerous seismic zones, including the largest intraplate seismic zone of the US, the New Madrid Seismic Zone (NMSZ), and has undergone extensive deformation from past episodes of the Wilson cycle. The recent deployment of a dense seismic network by EarthScope Transportable Array in the CEUS has revealed complex upper-mantle heterogeneity of unknown physical origin. The link between these current upper-mantle observations and the ongoing crustal seismicity in the CEUS is not yet understood and needs attention for a comprehensive model of seismicity within the CEUS. Additionally, the network coverage has presented an opportunity to image the structure beneath the CEUS better and answer new research questions in this region.

The presented work provides new and updated models that can illuminate better than before on the factors responsible for the seismicity and the unexplained anisotropy within the CEUS, that are consistent with the seismological observations. Lithospheric layering is also constrained using receiver functions in this region. A systematic analysis of the possible origins of large negative Vp and Vs anomaly found beneath the NMSZ shows that in addition to temperature effects, an increase in orthopyroxene contents is required to explain the observed Vp and Vs magnitudes. Viscoelastic models based on all of the possible scenarios show concentration of differential stress from the upper mantle into the upper crust of the NMSZ. However, it is demonstrated that among the three factors considered—temperature, water content, and orthopyroxene content—, the temperature is most sensitive to the computed differential stress. Another model, which includes all the major CEUS seismic zones and the upper mantle extends down to 660 km depth, employs diffusion and dislocation creep with temperatures inverted from a different P-wave tomography study. Results from this model show stress concentration at all the seismic zones due to the buoyancy flow arising from the upper-mantle heterogeneity. The third work on the upper mantle within the CEUS using S-wave receiver functions shows a continuous low-velocity mid-lithospheric layer starting at depths of 60 to 100 km in the Mississippi Embayment. A detailed investigation using the synthetic seismograms points to both temperature and compositional variations to explain the origin of this layer. Lastly, a numerical model is found that incorporates an ancient mafic pluton and a low-velocity structure beneath the NMSZ, to explain the observed spiral-like Pn anisotropy.

TABLE OF CONTENTS

Contents **Pages**

List of Tables **xiii**

List of Figures **xiv**

1 Introduction **1**
- Tectonic history of the study area . . . 1
- Proposed origins of the CEUS seismicity . . . 4
  - Inherited tectonic structures . . . 4
  - Large-scale geological processes . . . 5
  - Local stress perturbations . . . 6
- Recent seismological observations . . . 7
- Overview of the thesis . . . 8

2 Possible orthopyroxene enrichment in the upper mantle below the Mississippi Embayment **12**
- Introduction . . . 13
- Seismic Tomography . . . 16
- Methodology . . . 18
  - Viscosity Calculations . . . 18
  - Case I: Temperature only . . . 18
  - Case II: Temperature and water content . . . 20
  - Case III: Temperature and Opx content . . . 21
  - Differential Stress Calculations . . . 22
- Model Results . . . 23
  - Case I: Temperature only . . . 23
  - Case II: Temperature and water content . . . 24
  - Case III: Temperature and Opx content . . . 26
- Discussion . . . 28
- Conclusions . . . 34
- Appendix A . . . 35

3 Stress concentration in the Central and Southeastern US seismic zones due to upper mantle heterogeneities **37**
- Introduction . . . 38
- Seismic tomography and upper mantle heterogeneities . . . 40
- Modeling instantaneous mantle flow . . . 42
  - Temperature Calculations . . . 42
  - Model Setup . . . 44
  - Differential and Coulomb stress changes . . . 46
- Model results . . . 49
- Discussion and Summary . . . 53
- Appendix B . . . 61

Supplementary figure . . . 66

4 **Detecting lithospheric discontinuities beneath the Mississippi Embayment using S wave receiver functions** **67**
Introduction . . . 68
Data . . . 70
Methodology . . . 71
Receiver Functions and Interpretation . . . 77
Discussions . . . 84
Conclusions . . . 89
Supplementary figure . . . 90

5 **A possible numerical model to explain the unusual Pn anisotropy in the Central and Eastern US** **91**
Introduction . . . 92
Data assimilation strategy . . . 95
Numerical methodology . . . 97
  Model setup . . . 97
  Model outputs for anisotropy . . . 99
Results . . . 100
  Effects of isolated anomalies . . . 101
  Effects of the mafic intrusion density . . . 102
  Effects of the lower crustal viscosity . . . 103
Discussion and summary . . . 103
Supplementary figure . . . 107

6 **Conclusions** **108**
Summary . . . 110
Scope . . . 112

References **113**

LIST OF TABLES

Tables **Pages**

2.1 Rheological constants used in our model simulations 19

2.2 Elastic moduli, their temperature derivatives and anelasticity parameters . . 36

3.1 Values for dislocation and diffusion creep 46

3.2 Seismic Zones* and their associated dominant fault geometries 49

3.3 Mineral physics data used in this study 62

LIST OF FIGURES

Figures **Pages**

1.1 Map of the Central and Eastern US as well as of the inherited tectonic features from two episodes of the Wilson cycle and the present-day seismic zones. Green lines indicate the intracratonic rifts. The blue line indicates the leading edge of the Appalachian-Ouachita orogeny formed during the assembly of Pangaea. The orange line marks the boundary of the Mississippi Embayment and the coastal plain. Red dots denote the epicenters of the earthquakes recorded in the past twenty years (Jan 2000 to Jan 2020). AO: AlabamaOklahoma transform, MCR: MidContinent Rift, IS: Induced Seismicity in Oklahoma due to fluid injection (Llenos & Michael 2013), OR: Ouachita rift, RCG: Rough Creek Graben, GF: Grenville Front, OFS: Oklahoma Fault system, NMSZ: New Madrid Seismic Zone, ETSZ: Eastern Tennessee Seismic Zone, SCSZ: South Carolina Seismic Zone and CSV: Charleston Seismic Zone. The stars represent the epicenters of the large earthquakes in the CEUS (refer to text for details). The earthquake catalog is obtained from the United States Geological Survey at `https://earthquake.usgs.gov/earthquakes/search/`. (Tectonic features modified from Basu & Powell (2019)) 3

1.2 The three anomalous features recently observed in seismic tomography and anisotropy studies. (1)The low-velocity anomaly of high and similar magnitudes in Vp and Vs, found by Nyamwandha et al. (2016), outlined by dashed lines. (2) Large positive P-wave anomaly observed by Biryol et al. (2016). (3) Map of the region showing the spiral-shaped Pn-anisotropy found by Basu & Powell (2019) in a box and the profiles of cross-sections, shown in left. . . . 8

1.3 S-wave receiver functions for a simple velocity model illustrating the conversions at velocity contrasts. (a) Cartoon showing conversion of the incident S-wave to P-wave at an interface. (b) A simple velocity model with two velocity jumps: one high-velocity for Moho and another low-velocity for Lithosphere-asthenosphere boundary (LAB). (c) The computed seismogram components and the resultant S-wave receiver function for the velocity model shown in (b). S_Mp and S_Lp are the converted phases from the Moho and the LAB, respectively. 10

2.1 A shaded relief map of earthquake epicenters (>Mw2.0) in the New Madrid Seismic Zone (NMSZ) from May, 2002 to May, 2017.The color and size of symbols represent the depth and magnitude, respectively. The black dashed line marks the boundary of the Mississippi Embayment and the Reelfoot Rift is contained within the blue dashed line. The inset shows a part of the North American and the U.S. state borders providing a geographic reference for the location of the NMSZ (black square). The earthquake catalogue is obtained from the United States Geological Survey at `https://earthquake.usgs.gov/earthquakes/search/` 14

2.2 Reference P and S wave velocities (V_{P0} and V_{S0}) used by Nyamwandha et al. (2016) for their tomography results, and reference temperature (T_0) from Zhan et al. (2016), based on which the temperature anomalies are calculated. T_0 is discretized with depth from average geotherm for CEUS (Goes & van der Lee 2002) and is constant within each depth interval. 17

2.3 P and S wave tomography results, modified after Nyamwandha et al. (2016), at depth of 120 km and 160 km. Vp and Vs anomalies have similar magnitudes and spatial distributions. Purple and black dashed line marks the reelfoot rift and the Mississippi Embayment, respectively. 18

2.4 (a) Model domain and the P wave velocity anomalies from Nyamwandha et al. (2016). The domain has 3 layers: 20 km-thick upper crust, 20 km-thick lower crust, and mantle. The purple line through the NMSZ marks the location of vertical profiles of model results shown in the subsequent figures. The rectangle on the surface represents the spatial extent of the tomography model. (b) Model domain representing the S wave velocity anomalies from Nyamwandha et al. (2016) at 100 km depth. Arrows denote the velocity boundary conditions applied on the side walls. 19

2.5 Minimum and maximum temperatures (blue lines) calculated from P wave velocity anomalies as in Case I; and the solidus (red line) from Katz et al. (2003) 21

2.6 Conversion of the velocity anomalies into model viscosities at cross-section CC' in Fig. 2.4a. Thin vertical gray lines mark the boundaries of the tomography domain of Nyamwandha et al. (2016) (see Fig. 2.4a). Vertical axis is exaggerated by a factor of 3. (a) P-wave velocity anomalies (∂V_p) from Nyamwandha et al. (2016). (b) Temperature anomalies calculated based on ∂V_p. (c) Viscosities computed based on the temperatures anomalies in (b) and the reference temperature shown in Fig. 2.2 24

2.7 Scatter plots of temperature anomalies calculated from P wave (ΔT_p) and S wave (ΔT_s) anomalies with the best-fitting lines (black). The red line has a slope equal to 1, representing the case where both Vp and Vs anomalies are due to temperature only. 25

2.8 Selectively-added water contents calculated in case II are plotted as contours over the velocity anomalies converted from the temperatures in the super-solidus region on a cross-section along the latitude of 36.2° (left), which approximately coincides with CC' in Fig. 2.4 and on a layer at 100 km depth (right). The higher magnitude negative velocity anomalies correspond to higher calculated water contents. 26

2.9 Depth profiles of (a) viscosity (b) differential stresses within the NMSZ (profile location shown by the purple line in Fig. 2.4) for the model with selectively-added water in blue and the model computed from Vp-based temperatures calculated in Case I in black. Differential stresses (b) are zoomed out to observe the concentration in upper crust on the right 26

2.10 Inverted Opx contents and temperature anomalies at depths of 80 and 160 km. (left) Vp anomalies overlain by the contours of the Opx volume fraction. (right) Vs anomalies overlain by the contours of the temperature variations. 27

2.11 Same as Fig. 2.9 but for the models corresponding to the three possible effects of Opx enrichment on viscosity relative to Ol: Viscosity strengthening (red), viscosity weakening (blue) and the same viscosity as olivine (green). 28

2.12 Depth profiles of differential stress from all the cases (Case I to III) presented in this study. Case I: temperatures converted from the ∂V_p (black); Case II: selective addition of water in super-solidus regions and temperature calculated from Case I using ∂V_p (blue); Case III: temperatures inverted using ∂V_p and ∂V_s and Opx for its strengthening (red), weakening (green) and no (yellow) viscosity effects on Opx. The blue and black curves are indistinguishable. 32

3.1 A shaded relief map of the study area including the central and southeastern US seismic zones: New Madrid Seismic Zone (NMSZ), eastern Tennessee Seismic Zone (ETSZ) South Carolina Seismic Zone (SCSZ), Giles County Seismic Zone (GCSZ) and Central Virginia Seismic Zone (CVSZ). White dashed line represents the well-sampled region in the tomography results by Biryol et al. (2016) at a depth 130 km. The earthquakes that occurred over the period December 2011 - December 2018 and had $M_w > 2.5$ are plotted as colored circles. The size and color of a circle represent the event's magnitude and depth. The earthquake catalog is obtained from the United States Geological Survey at `https://earthquake.usgs.gov/earthquakes/search/`. 39

3.2 P wave tomography results of (Biryol et al. 2016) at a depth of 170 km. Panels A and B are cross-sections at 36° latitude and −86° longitude, respectively. Dashed black lines on the cross-sections mark the approximate boundaries of the high-density anomalies interpreted as a foundering lithospheric root. Dashed magenta lines on A indicates the low-velocity region interpreted by Biryol et al. (2016) as asthenospheric return flow due to the foundering lithosphere. The white arrow on A shows the direction of the return flow as speculated by Biryol et al. (2016). 42

3.3 P wave anomalies (left) from Biryol et al. (2016) and the inverted temperatures (right) at depths of 200 (top) and 605 km (bottom). Black dashed line in the depth layer 605 km marks the boundary of the high-velocity structure interpreted as a foundering drip by Biryol et al. (2016). 43

3.4 Model setup with the computed rheology based on the regional tomography by Biryol et al. (2016) and the boundary conditions applied. Gray isosurface represents P-wave anomalies > 2 % in the region interpreted as lithospheric foundering. Instantaneous flow along slice AA' passing through the ETSZ and NMSZ is discussed in Fig. 3.12. Black lines indicate the state boundaries and red dots are epicenters for the earthquake catalog used in Fig. 3.1. Temperature depth profile of the crust is shown on the left. 45

3.5 Cartoon sketch showing the sign convention for the strike, dip, and normal to the fault surface. 47

3.6 Cross-section along latitude=36° across model setups for which stress calculations are done in this study. HT, HM, and HR represent the HeTerogeneous, Homogeneous Mantle and Homogeneous Root models, respectively. The models, HT−HM and HT−HR isolates the effects of upper mantle heterogeneity and lithospheric drip, respectively. 48

3.7 (a) Differential stress changes in the HT−HM case ($\Delta\sigma_{\mathrm{diff}}^{\mathrm{HT-HM}}$) at a depth of 15 km. Black dots are earthquake epicenters from USGS data between 2011-2018. Gray lines denote the US state boundaries. Seismic zones investigated in this study are the northeastern arm of the New Madrid Seismic Zone (NMSZ_NE), Eastern Tennessee Seismic Zone (ETSZ), South Carolina Seismic Zone (SCSZ), Giles County Seismic Zone (GCSZ) and Central Virginia Seismic Zone (CVSZ). F_1 and F_2 indicates the areas of anomalously high values of $\Delta\sigma_{\mathrm{diff}}^{\mathrm{HT-HM}}$. Dashed magenta line marks the boundary of the foundering at 605 km depth. The box BB'CC' indicates the region enlarged in subsequent figures. (b) Differential stress change for HT−HR ($\Delta\sigma_{\mathrm{diff}}^{\mathrm{HT-HR}}$) in a region centered on the ETSZ. 50

3.8 Coulomb stress change (ΔC) for HT−HM calculated for different fault orientations in Table **??**) at 15 km depth. Seismic zone(s) and their corresponding optimal fault geometries are mentioned for each subplot: (a) Eastern Tennessee Seismic Zone (ETSZ) and Giles County Seismic Zone (GCSZ), left lateral vertical fault striking EW, (b) ETSZ and North-eastern arm of the New Madrid Seismic Zone (NMSZ_NE) and right lateral vertical fault strikingt N10°E, (c) Central Virginia Seismic Zone (CVSZ) and thrust fault dipping 50° SE striking N30°E, (d) South Carolina Seismic Zone (SCSZ) and thrust fault dipping 40° W striking N-S. 51

3.9 Same as Fig. 3.8 but for HT−HR. 52

3.10 Proposed fault planes from observational studies based on focal mechanism and earthquake hypocenters (Table 3.2) versus fault planes at which ΔC_{HT-HM} is maximum. The markers represent each of the seimic zones: New Madrid Seismic Zone (NMSZ), Eastern Tennessse Seismic Zone (ETSZ) South Carolina Seismic Zone (SCSZ), Giles County Seismic Zone (GCSZ) and Central Virginia Seismic Zone (CVSZ). The sense of fault slip is indicated with the color of the marker as thrust(T), right-lateral strike-slip (SS, RL), left-lateral strike slip (SS, LL) and normal (N). Encircled markers represent the orientations maximizing ΔC_{HT-HM}. A double-ended arrow pairs the observed and modeled fault orientations for each seismic zone. 55

3.11 Maximum horizontal stress directions (S_H) at all the seismic zones for the heterogeneous (HT) model (black lines) overlain over the stress regime (R) computed using the principal stresses at these seismic zones. 57

3.12 Velocity (arrows) and viscosity fields from the model HT on the slice AA′ (marked in Fig 3.4). The extreme high-velocity vectors observed west of the NMSZ and out of the plane are from the upward return flow due to the downward pull of the lithospheric drip and are likely an artifact due to fixed boundary conditions at the sides. 58

3.13 Residual topography calculated from densities based on the regional tomography by Biryol et al. (2016) used in this study and from global models. (a) Crustal thickness from CRUST1.0 (Laske et al. 2013). (b) Lithospheric thickness from LITHO1.0 (Pasyanos et al. 2014) (c) Residual topography calculated using (a) and (b). (d) Residual topography based on the densities calculated using the regional tomography. Encircled letters, A, B, and C, mark the regions where residual topography are strongly positive in both models. The dashed blue line delineates the topographic low due to the lithospheric drip. 59

S1 Coulomb stress change, ΔC, for HT−HM in the seismic zones for possible strikes, dips, and slip directions: right-lateral, left-lateral strike-slip, normal, and thrust faulting. Subplots are also labeled with maximum ΔC, and a triangular marker denoting the orientation and dip where the maximum occurs. 66

4.1 (a) Polar plot showing the number and azimuthal directions of the earthquake hypocenters between Jan, 2010 to Dec, 2017 with respect to the receivers used in this study.(b) The study region showing all the broadband stations from various networks (filled triangles) overlying with the number of RFs in each bin of size 1° x 1° with an overlap of 0.5°. NELE: Northern Embayment Lithospheric Experiment, TA: EarthScope Transportable Array, NM: New Madrid network. Earthquake data is obtained from United States Geological Survey at `https://earthquake.usgs.gov/earthquakes/search/`. Inset shows our study region relative to the map of US. 70

4.2 Velocity model used for computing the synthetic seismograms, based on the CRUST1.0 (Laske et al. 2013) and IASP91 (Kennett & Engdahl 1991) Earth models with an added negative velocity contrast (NVC) at depth 120 km. . . 72

4.3 Radial and vertical components from one earthquake recorded at HICK station in the Mississippi Embayment in black and the corresponding waveform data generated using the noise model utilized in our study. 74

4.4 Noise-free and noisy synthetic seismograms computed following the approach by Langston & Hammer (2001). Each row represents the different noise levels, i.e., 0, 0.5, 1, 1.5, in the vertical component, the radial component, and the S-wave receiver function. The converted S_NP phase at the top of low-velocity zone (marked in Fig. 4.2) is shown in the top right receiver function. 75

4.5 Normalized S-wave receiver function (SRF) with and without added coda noise after stacking and the corresponding misfit of the Sp phase converted at the top of negative velocity zone (S_Np) between noisy and noise-free seismograms. (Left) Black solid and dotted waveforms are the calculated RFs from noise-free and noisy seismogram components, respectively. The SRF functions calculated after stacking 100 bootstrapped noisy seismograms (COMP_stacked) and receiver functions (SRF_stacked) are shown in blue and red, respectively, at different coda noise levels governed by constants, C_V, C_R. The vertical line marks the maximum amplitude of S_Np. (Right) Mean misfit between the noisy and the noise-free S_Np along with one standard deviation after 500 bootstrap iterations plotted with the number of samples used in component and RF stacking. 77

4.6 Map showing the amplitude of the S_Np phase in the stacked SRFs. Black and cyan dashed line marks the boundary of the Mississippi Embayment and the Reelfoot rift, respectively. 78

4.7 (left) Inferred depths to the negative velocity gradient, which is estimated after depth migration and stacking the S receiver functions across the study region. The contour of the low-velocity anomaly found by Nyamwandha et al. (2016) at 100 km depth is marked by white. Black and magenta dashed line marks the boundary of the Mississippi Embayment and the Reelfoot rift, respectively. (right) Latitudinal and longitudinal profiles, corresponding to the letters and locations marked by magenta lines in the map view on the left, showing the stacked depth migrated RFs. The depth to the Moho and the negative upper mantle discontinuity is picked using cyan and magenta lines, respectively. 79

4.8 Various velocity models documented for Mississippi Embayment. These models are used to generate synthetic receiver functions for comparison with the observed receiver functions. 80

4.9 Observed and synthetic seismograms for the Mississippi Embayment using various velocity models plotted in Fig. 4.8. Each subplot marks the Sp phase converted from the negative velocity gradient in the observed and synthetic seismogram using black and dashed blue lines, respectively. 81

4.10 (a)Interpretation of the observed negative Sp phase (S_Np) using a suite of synthetic velocity models modified using a velocity model combined after Langston (1994) and Chen et al. (2016). (b)The difference in the width of the observed and synthetic S_Np for different separations between the two low-velocity layers in (a). The filled circle represents the minimum misfit in the observed and the modeled S_Np phase for separation of 10 km. (c) RFs from three models employing varying separations in (b) to illustrate the single peak, overlapping and double-lobed S_Np in plots A, B, and C, respectively. 82

4.11 (left) The best-fit modeled (blue) and observed (black) receiver function with the window of the S_Np phase. (right) The velocity model used to generate the synthetic RF, and the low-velocity zone (LVZ) marked for reference. . . . 83

4.12 Thermal lithosphere-asthenosphere boundary defined for the continental interior at the intersection of the Vp based geotherm taken from Goes & van der Lee (2002) and mantle adiabat with a potential temperature of 1300°. 86

S1 (left) Inferred depths to the negative velocity gradient, which is estimated after depth migration and stacking the seismogram components following the technique by Abt et al., (2010). The contour of the low-velocity anomaly found by Nyamwandha et al. (2016) at 80, 100 and 160 km depth is marked by grey, white and black, respectively. Black and magenta dashed line marks the boundary of the Mississippi Embayment and the Reelfoot rift, respectively. (right) Latitudinal and longitudinal profiles, corresponding to the letters and locations marked by magenta lines in the map view on the left, showing the stacked RFs. The depth to the Moho and the negative upper mantle discontinuity is picked using cyan and magenta lines, respectively. 90

5.1 The disparity in the observed Pn anisotropy (left) (Basu & Powell 2019) and SKS splitting results (right) (Nyamwandha & Powell 2016) in the Central and Eastern US. Each subplot also shows the direction of the absolute plate motion (APM) from the HS3-NUVEL-1A model (Gripp & Gordon 2002) in black, and the outline of the Mississippi Embayment (ME) in magenta. The spiral-like Pn anisotropy is centered at the New Madrid Seismic Zone (NMSZ). The lengths of the blue (Pn anisotropy) and green (SKS splitting) lines are proportional to the seismic anisotropy. 94

5.2 Vote maps outlining (a) the mafic intrusion (MI) in the lower crust and (b) the low-velocity zone (LVZ) in the upper mantle. The geometry of each feature, suggested by a study, is represented by a unique color in the legend. The dashed-dotted line marks the geometry of the MI and the LVZ used in numerical models, where vote count is more than three. The cross-section along BB' is shown in Fig. 5.3. 96

5.3 Cross-section BB' through the northern Mississippi Embayment from Nyamwandha et al. (2016) (refer to Fig. 5.2 for plane view) illustrating the depth structure of the low-velocity zone (LVZ) and the mafic intrusion (MI). Red dots represent the approximate hypocenter locations. 96

5.4 Reference model used in ASPECT for the calculations of stress and strain fields. The model domain consists of three depth layers: upper crust, lower crust, and mantle. Blue and red iso-surfaces represent the anomalous mafic intrusion, and the low-velocity zone, respectively. The corresponding densities and viscosities of all the features are indicated for our reference model. Black lines mark the state boundaries. Magenta line outlines the Mississippi Embayment. The initial adiabatic temperature profile used is shown in the top left corner. 98

5.5 Division of the observed anisotropy results into zones I, II, III and IV. The output stress/strain at 40 km depth is used for comparison with the observations. The zones are distinguished by different bounding box colors. 100

5.6 The observed anisotropy results (blue lines) along with the reference model output, ϵ_1 (left) and S_H (right), directions every five model points (red lines). Each zone is bounded by green box and the filled region shows areas with good correspondence between the modeled and the observed anisotropy. The black solid line marks the boundary of the mafic intrusion at depth 40 km. Tangents to the maroon curve in each plot are approximately parallel to the local fast directions, which are circular and radial in the output ϵ_1 and S_H, respectively. 101

5.7 Correlation ratio of the model outputs used as anisotropy indicators, ϵ_1 (blue) and S_H (green) within each zone for different model setups: (a) the reference model, (b) the model with only the high-density MI, and (c) the model with only the LVZ. The average correlation ratio is noted for each model setup in the top right. 102

5.8 Same as Fig. 5.7(a) but for different density contrasts of the mafic intrusion with the lower crust ($\Delta\rho_m$). 102

5.9 Same as Fig. 5.7(a) but for different viscosities of the lower crust (η_{LC}). . . . 103

5.10 SKS splitting results (green lines) by Nyamwandha & Powell (2016) and the modeled maximum finite strain (red lines) at depth 250 km in our study region. The gray areas shows good correspondence between the observed anisotropy and the model results. State lines are shown in black. 105

S1 The computed maximum finite strain directions (ϵ_1) for a simplified models from Fig. 5.4 having an idealized spherical high-density body with density contrast +200kg/m^3 (left), and a model with a semi-spherical low-density body with density contrast −100kg/m^3 (right). The white lines shows the direction of the ϵ_1 and the red contour in the left shows the contour marking the dense body 107

6.1 A cartoon showing the conclusions from all the chapters along latitude 36°. Data analysis from Chapter 2 indicates that low-velocity anomaly in the upper mantle below the NMSZ could be explained by orthopyroxene (Opx) enrichment. It is proposed that increased Opx content occurs from the reaction of hydrous fluids rising from a stalled fragment of the Farallon slab. Numerical model results from Chapter 3 demonstrates that the upper-mantle heterogeneity promotes the preexisting faults to slip in the seismic zones of the Central and Eastern US. The S-wave receiver functions (SRF) study in Chapter 4 reveals a negative velocity lithospheric discontinuity around depths 60 to 100 km, interpreted as a mid-lithospheric discontinuity. Chapter 5 explores the origins of observed Pn anisotropy using numerical models incorporating the low-velocity zone and the mafic intrusion observed beneath the NMSZ. . . . 109

Chapter 1

Introduction

The following sections outline the tectonic history of the CEUS, previously proposed models for seismicity in the region, recent seismic tomography models for the CEUS, and the questions addressed in this work along with its main findings.

Tectonic history of the study area

The Central and Eastern United States (CEUS) is the region east of the Rocky Mountains in the conterminous US. It is part of the stable continental craton with a present surface deformation rate of 3×10^{-9} yr^{-1} (Boyd et al. 2015). Despite the low strain rates, the CEUS has experienced large destructive earthquakes, such as the three 1811-1812 (Mw > 7) earthquakes in the New Madrid seismic zone (Nuttli 1973), the 1866 (Mw ~ 7) earthquake at Charleston, South Carolina (Boyd & Cramer 2014), and the recent 2011 (Mw $= 5.8$) earthquake at Mineral, Virginia (Hough 2012). Additionally, the CEUS frequently experiences low to moderate magnitude earthquakes—mostly at upper to mid-crustal depths (Johnston 1996)— in localized zones, i.e., the New Madrid Seismic Zone (NMSZ), the Eastern Tennessee Seismic Zone (ETSZ), the Central Virginia Seismic Zone (CVSZ), South Carolina Seismic Zone (SCSZ) and the Charleston Seismic Zone (CSZ) (Fig. 1.1).

The tectonic evolution of the CEUS provides some explanation for the observed seismicity. The crust of the CEUS comprises different geological provinces accreted to the eastern margin of the paleo-North American plate. The region experienced two Wilson cycle episodes since the Mesoproterozoic (Thomas et al. 2006). The first episode started with the assembly of the Rodinia supercontinent (1.3 to 1 Ga), which formed during the Grenville orogeny as the Grenville province collided with the paleo North American plate called Laurentia. The collision near the plate boundary triggered intracratonic rifting, creating the Mid-continental rift (1.1 Ga) (Whitmeyer & Karlstrom 2007). The first cycle ended when Rodinia split apart, opening the Iapetus ocean, separating Laurentia from the other continental plates and creating the failed rift arms including the Reelfoot Rift, and Oklahoma aulacogen (600 to 500 Ma) (Whitmeyer & Karlstrom 2007). The second episode began with the closing of the Iapetus Ocean and the formation of Pangea (300 to 250 Ma). The Appalachian-Ouachita orogeny resulted in the assembly of Pangea. The second episode continues as Pangaea segregated into the present-day continental plates with the opening of the Atlantic ocean. The breakup of Pangea led to thick sedimentation in the Mississippi valley. These episodes have left behind several expressions of weakness in the crust of the CEUS at the rift/accretionary margins, such as fractures, faults, and shear zones. The locations of some of the weaknesses correlate with the present-day locations of the seismic zones (Sykes 1978) (Fig. 1.1).

Both observational studies and numerical modeling have been utilized in a complementary way to understand the risks associated with earthquakes in the CEUS. The observations are needed to infer the physical parameters of the Earth (i.e., temperature, density, rheology), which are used to set up the numerical models. Since direct measurements of stress on the existing fault structures are not available, numerical geodynamic modeling has become a useful tool to model the stress state within this region. Various types of data such as gravity, magnetic anomalies, and seismic tomography have been used for imaging the structure beneath the CEUS, but better-resolved images are always desirable. Similarly, it is essential to update the existing geodynamic models so that they are consistent with the recent observations, and can provide some hints into the outstanding questions in the CEUS.

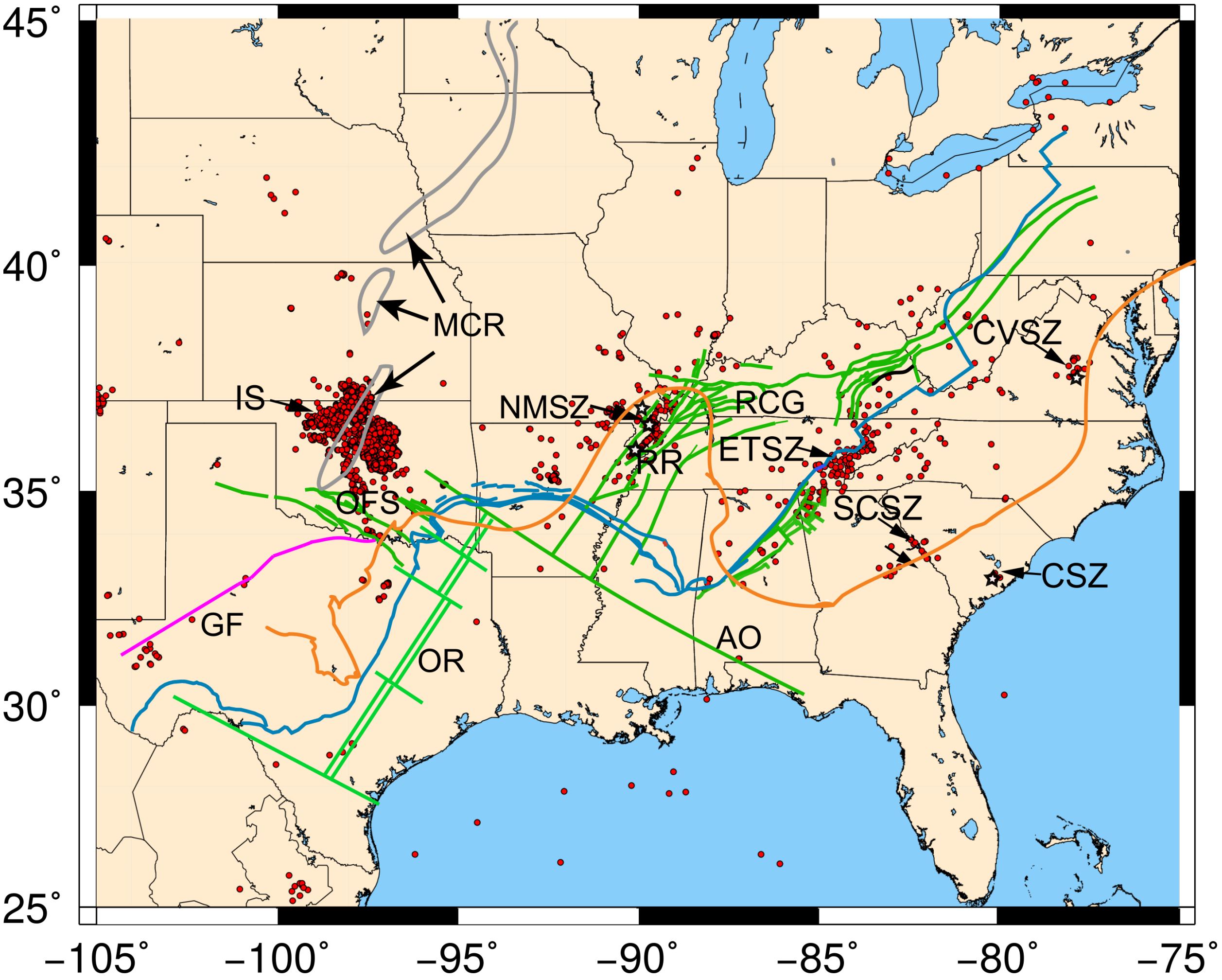

Fig. 1.1: Map of the Central and Eastern US as well as of the inherited tectonic features from two episodes of the Wilson cycle and the present-day seismic zones. Green lines indicate the intracratonic rifts. The blue line indicates the leading edge of the Appalachian-Ouachita orogeny formed during the assembly of Pangaea. The orange line marks the boundary of the Mississippi Embayment and the coastal plain. Red dots denote the epicenters of the earthquakes recorded in the past twenty years (Jan 2000 to Jan 2020). AO: AlabamaOklahoma transform, MCR: MidContinent Rift, IS: Induced Seismicity in Oklahoma due to fluid injection (Llenos & Michael 2013), OR: Ouachita rift, RCG: Rough Creek Graben, GF: Grenville Front, OFS: Oklahoma Fault system, NMSZ: New Madrid Seismic Zone, ETSZ: Eastern Tennessee Seismic Zone, SCSZ: South Carolina Seismic Zone and CSV: Charleston Seismic Zone. The stars represent the epicenters of the large earthquakes in the CEUS (refer to text for details). The earthquake catalog is obtained from the United States Geological Survey at `https://earthquake.usgs.gov/earthquakes/search/`. (Tectonic features modified from Basu & Powell (2019))

Proposed origins of the CEUS seismicity

Inherited tectonic structures

The presence of preexisting geological and tectonic structures under the influence of plate-boundary stresses is considered to be important at the New Madrid Seismic Zone (NMSZ), the largest intraplate seismic zone of the US. The correlation of the preexisting geological structures with the seismicity in the NMSZ was probably first recognized by Hildenbrand et al. (1977). They postulated that the anomalies delineated from gravity and magnetic data could influence the seismicity in the northern arm of the NMSZ. A following study by Braile et al. (1982) suggested a seismotectonic model in which the faults associated with the existing rift complex in the northern NMSZ could get reactivated in the presence of the regional stress field. However, they do not explain why only some faults tend to get reactivated, and others do not. The calculations by Rydelek & Pollitz (1994) indicated that post-seismic relaxation from the 1811-1812 NMSZ earthquakes (Mw > 7) could load the existing faults and influence the present-day seismicity within the NMSZ. A 2-D numerical model incorporating a weak crust and a simplified fault structure for the NSMZ was proposed by Gangopadhyay et al. (2004) to explain the observed seismicity. Grana & Richardson (1996) suggested a 2-D finite element model in which sinking of a high-density mafic pluton (or “rift pillow”) within a strong lower crust and mantle could generate earthquakes at the preexisting rift structures. This model was later modified by Pollitz et al. (2001), who proposed the sinking of the “rift pillow” in a weakened lower crust as a driving mechanism for earthquake generation in the NMSZ. A more recent study by Levandowski et al. (2016) developed a 3-D density model from the gravity, magnetic and seismic datasets and found an anomalous lower crust beneath the NMSZ. Their results from the finite element simulations of the model indicated high buoyancy stress localized in the crust of the NMSZ, which adds to the far-field tectonic stress directions, causing the observed seismicity.

The tectonic structures formed during the past episodes of Wilson cycles in the

CEUS have been exploited in other seismic zones as well. Powell et al. (1994) proposed a seismotectonic model in the Eastern Tennessee Seismic Zone in which they invoked the boundary between two geological blocks of different strengths as a concentrator of the region's earthquakes. This model was updated in Powell & Thomas (2016) using all the available geological and geophysical datasets. Powell & Thomas (2016) suggested that the sheared basement rocks, bounded by a major transform fault, are reactivated, which are responsible for the observed seismicity. A similar study on the eastern US earthquakes, including the Central Virginia Seismic Zone, by Soto-Cordero et al. (2018) suggested that lateral variations in the crust arising from the past tectonic events could play an essential role in concentrating stress and generating earthquakes. Another work by Gangopadhyay & Talwani (2005) suggests that the earthquakes in the Charleston Seismic Zone are a consequence of weak crust and intersecting preexisting faults.

Large-scale geological processes

Long-wavelength processes have also been considered as sources of stress responsible for earthquake generation in the CEUS. Cox & Van Arsdale (1997) suggested that the passage of Bermuda hotspot during the Cretaceous weakened the already rifted lithosphere in the Eastern US and Mississippi Valley Graben, which are the locations of current seismic zones: NMSZ, CSZ (Fig. 1.1). The work by Grollimund & Zoback (2001) investigates the stress effects from deglaciation of the Laurentide ice sheet (between 19 and 8 ka) on the structurally layered lithosphere of the NMSZ. The numerical model results showed that the Laurentide ice retreat might have increased the seismic activity of the NMSZ in the Holocene. Another model by Calais et al. (2010) proposed that the unbending of the lithosphere due to glacial erosion (between 18 and 10 ka) reduces the normal stress on the preexisting faults of the NMSZ, triggering earthquakes. A similar model is proposed by Gallen & Thigpen (2018) to explain the seismicity in the ETSZ. They suggested that preferential erosion of a weak zone reduced the clamping stress on the preexisting basement faults in the ETSZ, causing the faults to slip and generate earthquakes.

Local stress perturbations

The concentration of stress through a rheologically weak zone has been invoked as a likely mechanism for intraplate earthquakes. Liu & Zoback (1997) proposed that a weak upper mantle and lower crust reduces the cumulative lithospheric strength such that it could be deformed easily by the forces acting on the North American lithosphere. They applied this hypothesis to the NMSZ, which, according to their calculations, has a hotter lower crust and upper mantle. Their results of stress partitioning showed that the majority of deformational stress is transmitted in the upper crust of the NMSZ. Kenner & Segall (2000) proposed a time-dependent 3-D numerical model that can explain the repeated earthquakes in the NMSZ with the crustal-level weak zone. Their model included a weak lower crustal zone embedded in an elastic lithosphere under far-field tectonic stress. According to their model results, the weak zone in the lower crust concentrates stress over time and causes faults in the overlying brittle upper crust to fail. The energy released from the coseismic slip is partially transferred into the weak lower crustal zone, which could generate another earthquake in the future. Their model results present a recurrence interval of 500 to 2000 years in the NMSZ until the cumulative energy dissipates in areas surrounding the weak zone after each earthquake.

Contributions from the upper mantle heterogeneities have also been considered. Pollitz & Mooney (2014) found a low-velocity zone in the upper mantle beneath the NMSZ. Zhan et al. (2016) utilized their tomography results to infer viscosities in the Central US, assuming the seismic tomography represents temperature variations from a geotherm used to setup numerical models. Under the regional compressive stress, the finite element model results showed a local concentration of differential stress through the low-velocity zone into the overlying upper crust of the NMSZ.

The previous models have successfully demonstrated varied origins of seismicity in the CEUS, but some common inferences could be made from these studies. Firstly, most of the studies invoked preexisting zone of weakness, such as faults or sheared rocks, in their mechanisms to explain the seismicity. However, not all weak structures generate earthquakes, and a mechanism for an increase in stress at the preexisting structures is required for the fault to slip. Secondly, it can be seen that limited models are available in the literature to explain other seismic zones of the CEUS (Fig. 1.1), besides the NMSZ. Thirdly, it can be noted that the effects of deeper upper mantle heterogeneity (> 80 km) on the crustal seismicity of the CEUS have not been studied extensively. This is probably due to a lack of available good-resolution seismic data until 2011, when the US Array seismic stations were deployed in the CEUS. Lastly, only a handful of studies have made deductions about the physical state of this region (temperature, density, or composition), because of insufficient observational and experimental data.

Recent seismological observations

A recent deployment of the EarthScope Transportable Array and the FlexArray Northern Embayment Lithospheric Experiment in the CEUS that began in 2011 provided a large quantity of seismic data, with which several new features were revealed (Fig. 1.2). One of them is a pronounced low-velocity zone of unknown physical origin beneath the NMSZ (Fig. 1.2-1), first imaged by Pollitz & Mooney (2014) at depths of 60-200 km in a surface wave tomography study. The following study by Nyamwandha et al. (2016) observed this feature beneath the NMSZ at much higher resolution in the teleseismic tomography of the Mississippi Embayment. They found very low (up to -6%) anomalies of similar magnitude in both P-wave and S-wave velocities at depths of 80-150 km beneath the NMSZ. Another intriguing result is an eastward dipping large positive P-wave anomaly in the lithosphere by Biryol et al. (2016) (starting at 200 km and extending to 660 km) between the NMSZ and the ETSZ, interpreted as a foundering lithosphere (Fig. 1.2-2). A third observation is by Basu & Powell (2019), in which they found a unique spiral-shaped Pn anisotropy pattern centered at the NMSZ (Fig. 1.2-3) of unexplained origin.

These observations, in conjunction with previous models, have raised new research questions mainly regarding the role of the upper mantle heterogeneities in generating the

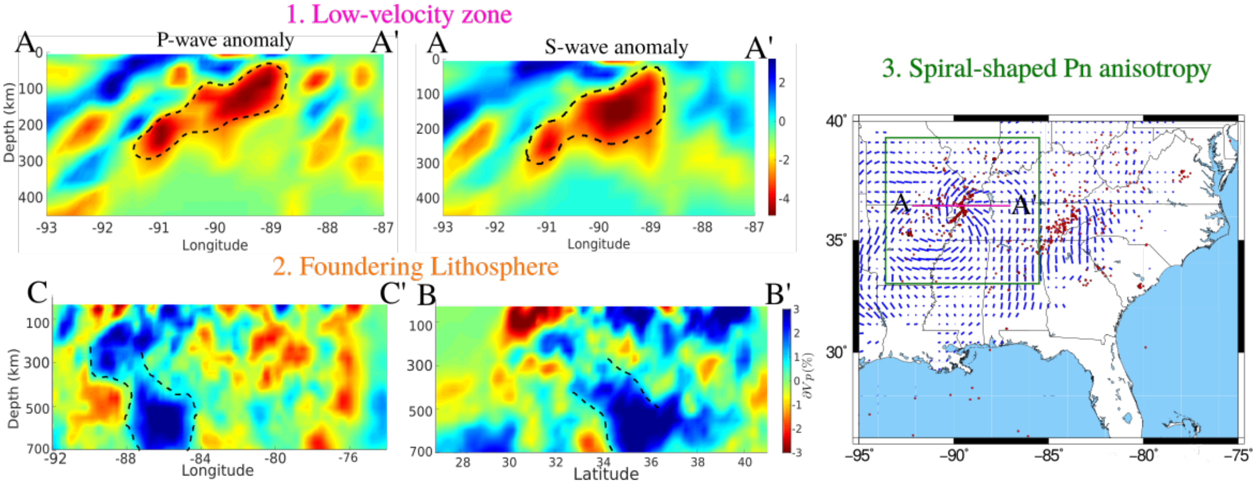

Fig. 1.2: The three anomalous features recently observed in seismic tomography and anisotropy studies. (1)The low-velocity anomaly of high and similar magnitudes in Vp and Vs, found by Nyamwandha et al. (2016), outlined by dashed lines. (2) Large positive P-wave anomaly observed by Biryol et al. (2016). (3) Map of the region showing the spiral-shaped Pn-anisotropy found by Basu & Powell (2019) in a box and the profiles of cross-sections, shown in left.

CEUS seismic zones. This dissertation is a collection of efforts to advance this question towards a better understanding of the CEUS seismicity through data interpretation and numerical modeling.

Overview of the thesis

Chapter 2 explores the possible physical sources of the observed tomography by Nyamwandha et al. (2016) (illustrated in Fig. 1.2-1), and the stresses arising from it in the upper crust of the NMSZ. The motivation behind exploring the origins of the seismic tomography is the unique similarity of a very low-velocity (up to -6%) feature in both Vp and Vs anomalies observed in the upper mantle beneath the NMSZ. Usual interpretations for a decrease in velocity is temperature, which affects S-wave velocity more than P-wave velocity. Therefore, additional factors, such as composition or water content, are investigated to explain this anomalous feature. Forward calculations of velocity anomalies assuming water content and temperatures affirmed that an additional factor that decreases P-wave velocity more than S-wave velocity is required. Simultaneous inversion of both Vp and Vs anomalies shows that an increase in orthopyroxene (Opx) content and temperatures could satisfy the tomography results. The influence of each of the possible cases involving a combination of temperature variations with water content and Opx content is explored using numerical models assuming viscoelastic rheology. The models are simulated using NE-SW compression until the differential stress at 10 km is approximately equal to 200 MPa (a condition based on Byerlee's law (Zoback et al. 1993)). Differential stress calculations from all of these models show a concentration of stress from the weaker upper mantle into the stronger upper crust, corroborating with the previous models by Kenner & Segall (2000), Zhan et al. (2016). Additionally, these models show that temperature is most influential for the viscosity, and therefore to differential stress compared to the other factors considered.

The next chapter (Chapter 3) applies a similar modeling approach to computing the stress fields due to upper mantle heterogeneities at five seismic zones in the CEUS. The study presented in this chapter covers much greater lateral and depth extents than the one in Chapter 2, incorporating the regional tomography results from Biryol et al. (2016) (Fig. 1.2-2). The main goal of this work is to investigate any stress concentration due to upper-mantle heterogeneity and the foundering lithosphere at existing fault orientations of the seismic zones in the CEUS (shown in Fig. 1.1). Temperatures are inverted from the P-wave anomaly considering effects of composition, anelasticity, and phase transition with depth. The models are setup using a dislocation and diffusion rheology for two possible cases: one isolating all the upper mantle heterogeneity below 60 km depth and another, which isolates the large positive P-wave anomaly, interpreted as the foundering lithosphere. The instantaneous mantle flow generated in the models causes an increase in Coulomb stress at all the seismic zones when all the upper-mantle heterogeneity is taken into account. However, in the presence of foundering lithosphere only, the Coulomb stress concentration is much weaker and limited to nearby seismic zones, the ETSZ, and the northern arm of the NMSZ.

Chapter 4 shifts focus to an observational investigation of lithospheric layering

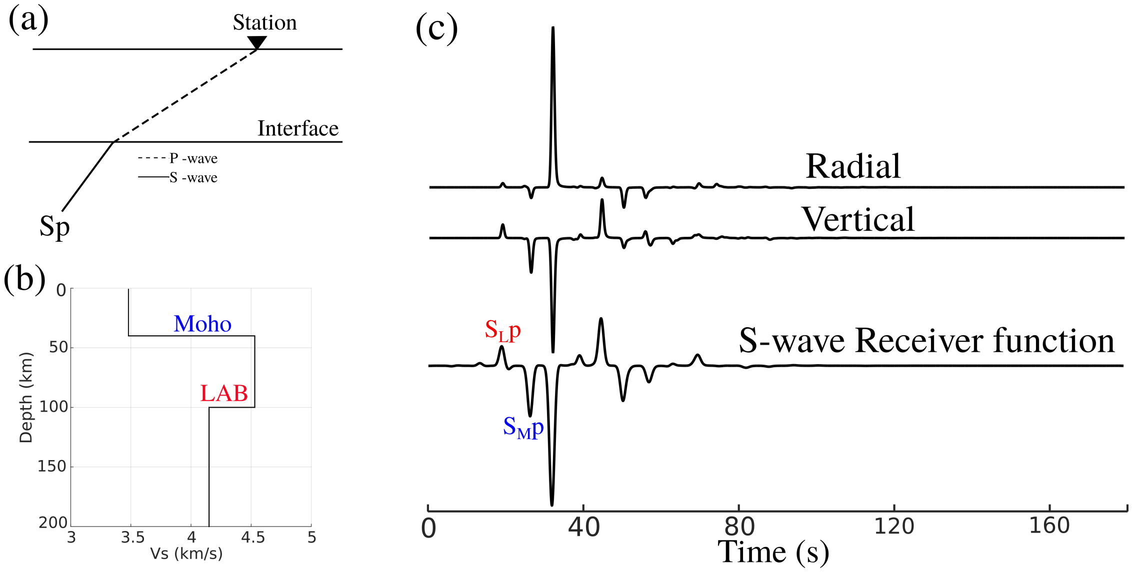

Fig. 1.3: S-wave receiver functions for a simple velocity model illustrating the conversions at velocity contrasts. (a) Cartoon showing conversion of the incident S-wave to P-wave at an interface. (b) A simple velocity model with two velocity jumps: one high-velocity for Moho and another low-velocity for Lithosphere-asthenosphere boundary (LAB). (c) The computed seismogram components and the resultant S-wave receiver function for the velocity model shown in (b). S_Mp and S_Lp are the converted phases from the Moho and the LAB, respectively.

beneath the Mississippi Embayment using teleseismic S-wave receiver functions. The motive is to determine lithospheric thinning beneath the NMSZ as suggested by Cox & Van Arsdale (1997), Biryol et al. (2016) and verify the low-velocity anomaly found by Nyamwandha et al. (2016) in the receiver functions. The basic principle of S-wave receiver functions is to deconvolve the radial component from the vertical component, such that the common source function is removed, and the structure near the receiver is highlighted. Fig. 1.3 illustrates this concept using a simplified velocity model. Before computing the receiver functions on event data, the methodology was tested using a suite of synthetics with an added noise model developed after Langston & Hammer (2001). The synthetic tests show that at low-to-moderate noise levels, the converted Sp phase at a negative velocity contrast could be recovered if enough receiver functions (> 50) are used in stacking. Earthquake data from 2011 until 2018 recorded at 178 seismic stations, part of the permanent New Madrid broadband network and temporary network by EarthScope, revealed a continuous negative Sp phase at depths of 60 to 100 km. Since these depths are much shallower than the expected depth of the lithosphere-asthenosphere boundary, this phase was interpreted as a mid-lithospheric discontinuity. Quantitative analysis of possible sources for this discontinuity showed that a combination of temperature and compositional change is the most likely mechanism.

Chapter 5, the last work in this dissertation, explores possible sources of the spiral-shaped Pn anisotropy beneath the NMSZ found by Basu & Powell (2019) using a numerical modeling approach. This is an interesting problem because the SKS anisotropy observed by Nyamwandha & Powell (2016) of the same region is along the absolute plate motion direction, implying a depth-dependent anisotropy beneath the NMSZ. First, a careful literature review of two prominent features beneath this region was done: one is the lower crustal mafic intrusion ("rift pillow" (e.g., Pollitz et al. 2001)), and other is the low-velocity zone investigated in chapter 2. This process delineates the two structures, which are then used in the numerical models consisting of three viscosity layers representative of the upper crust, the lower crust and the mantle. Both maximum strain (implying the flow direction of the lower crust) and maximum horizontal compressive stress (implying the direction of cracks in the upper crust) are used as the likely indicators of anisotropy from the models for comparison with the observed anisotropic signature. A range of probable density contrasts of the "rift pillow" and viscosities of the lower crust is assumed to best-match the spiral-shaped Pn anisotropy with the model results. The analysis from the finite strain outputs shows that the sinking mafic intrusion with density contrast +200 kg/m^3 in a weak lower crust with viscosity 10^{19}Pa·s, and the low-velocity zone, could match about 25% of the unusual anisotropic feature of the NMSZ.

Chapter 2

Possible orthopyroxene enrichment in the upper mantle below the Mississippi Embayment

A version of this chapter will be submitted for publication as Saxena, A., Choi, E., Powell C., and Langston, C. Possible orthopyroxene enrichment in the upper mantle below the Mississippi Embayment

Abstract

A recent high-resolution tomography study for the upper mantle beneath the New Madrid Seismic Zone (NMSZ), the most seismically active intraplate zone in the Central and Eastern US, reveals −3 to −6 % Vp and Vs anomalies in the depth range 100 to 250 km. We explore possible explanations for these anomalies by attributing them to elevated temperatures, water, and orthopyroxene (Opx) contents. Considering these sources of velocity anomalies, we determine viscosities and create forward numerical models with a Maxwell viscoelastic crust and mantle. We calculate differential stress at the NMSZ from these models. All of our models consistently show stress concentration in the upper crust (< 20 km) of the NMSZ from the upper mantle heterogeneity. However, our calculations indicate that restricting the observed velocity anomalies to temperature variations results in temperatures much higher than the olivine solidus, for which consistent observational support is lacking. Besides, high temperatures cannot be a sole explanation for the velocity anomalies since the magnitudes of the observed Vp and Vs anomalies are similar; Vs is more sensitive to temperature than Vp. We also find that elevated water content combined with temperature anomalies cannot explain the similar-magnitude Vp and Vs anomalies, although the presence of water allows for sub-solidus variations in temperature. Models with Opx enrichment give reasonable Opx content and temperature variations, which can yield Vp and Vs anomalies of a similar magnitude. The upper mantle viscosity is not reduced as much in the presence of Opx as when only elevated temperature is present, and the stress concentration effect in the upper

crust is correspondingly weaker. We speculate that the Opx enrichment could have been produced by fluids released from a stagnant piece of the Farallon slab imaged at around 670 km beneath the NMSZ.

Introduction

The New Madrid Seismic Zone (NMSZ), located in the Northern Mississippi Embayment, is a seismically active region as indicated by paleoseismic evidence (e.g., Tuttle 2002) and three historic large (Mw $>$ 7) earthquakes in 1811- 1812 (Johnston 1996, Bakun & Hopper 2004). The majority of the seismic activity occurs within the Reelfoot rift, an extensional feature formed during the breakup of supercontinent Rodinia about 570 Ma ago. Hundreds of small-magnitude earthquakes (Mw $<$ 5) are recorded annually (Fig. 2.1) posing a potential risk of seismic hazard in and around this zone.

Geodetic strain rates observed in this region are less than 3×10^{-9}/yr (Boyd et al. 2015). This value is much lower than the strain rate loading of active plate boundaries suggesting that the earthquake generation is not entirely associated with plate tectonics. This has puzzled researchers, invoking them to come up with alternative mechanisms to explain the NMSZ that are compatible with the field observations.

Several models in the NMSZ have been suggested to explain increased stress, and therefore, seismicity. Liu & Zoback (1997) proposed higher temperatures in the lower crust and upper mantle beneath the NMSZ compared to the surrounding regions, such that the tectonic stresses are mainly transmitted in the upper crust. Kenner & Segall (2000) developed a mechanical model to explain the recurrence of earthquakes in the NMSZ. In the Kenner & Segall (2000) model, a localized weak zone in the lower crust is embedded in an elastic lithospher and acts as a concentrator of the far-field tectonic stresses. As a result, stress is transmitted to the upper crust, generating earthquakes. Grollimund & Zoback (2001) suggested a model that incorporates a weak lithospheric mantle and deglaciation of the Laurentia ice sheet (20 Ka ago). The model showed increased seismic strains at the NMSZ, providing a viable mechanism for the 1811-1812 and Holocene

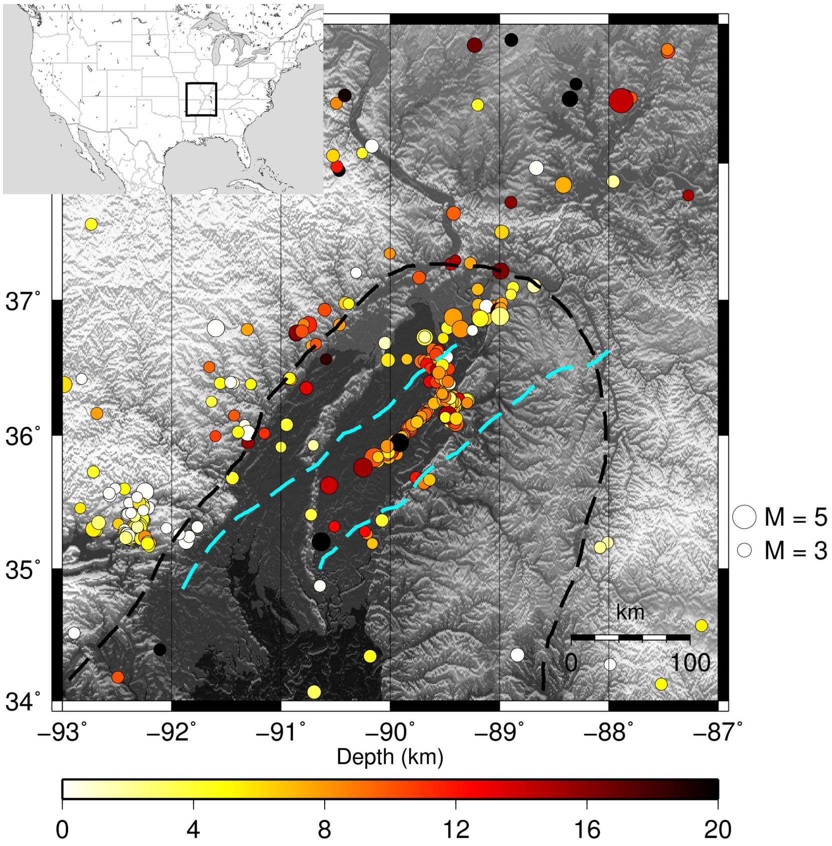

Fig. 2.1: A shaded relief map of earthquake epicenters (>Mw2.0) in the New Madrid Seismic Zone (NMSZ) from May, 2002 to May, 2017.The color and size of symbols represent the depth and magnitude, respectively. The black dashed line marks the boundary of the Mississippi Embayment and the Reelfoot Rift is contained within the blue dashed line. The inset shows a part of the North American and the U.S. state borders providing a geographic reference for the location of the NMSZ (black square). The earthquake catalogue is obtained from the United States Geological Survey at `https://earthquake.usgs.gov/earthquakes/search/`

.

earthquakes in the NMSZ. The sinking of a mafic intrusion beneath the NMSZ, observed by Mooney et al. (1983), was invoked by Pollitz et al. (2001) and later by Levandowski et al. (2016) in a three-dimensional model, to explain the stress concentration in the NMSZ. A recent study by Zhan et al. (2016) utilized a shear wave model developed by Pollitz & Mooney (2014) for the Mississippi Embayment, in which a low-velocity zone beneath the NMSZ was observed, to set up their numerical models. Zhan et al. (2016) translated the observed tomography into equivalent temperatures and found that the weak low-velocity zone below the NMSZ increases stress in the brittle upper crust, prompting seismicity. The previous models have established that a weak zone in the lower crust or lithosphere is unable to retain stress and transfers it to the stronger upper crust, where the seismogenic zone of the NMSZ lies (e.g., Mazzotti & Townend 2010).

However, these models do not investigate the physical origin of such weakness and do not reconcile with recent observations in the NMSZ. The work by Zhan et al. (2016) assumed high-temperatures as the factor for weakness in the upper mantle of the NMSZ, which seems inconsistent with more recent high resolution tomographic observations (Chen et al. 2016, 2014, Nyamwandha et al. 2016). Chen et al. (2014) and Chen et al. (2016) found a 5 % Vp decrease and 7 % Vs variation compared to the surroundings, respectively, at depths of 80-150 km beneath the NMSZ. Nyamwandha et al. (2016) observed Vs and Vp anomalies of a similar magnitude (-4% to -6%) beneath the NMSZ. When converted to temperature variations only, such low seismic velocity anomalies would require considerable partial melting in the upper mantle. This is not supported by geological observations as the last episode of magmatism, revealed in the Magnet Cove carbonatite around the Mississippi Valley graben, occurred about 100 Ma ago (Hildenbrand et al. 2001). Moreover, since Vs is more sensitive to temperature than Vp (e.g., Goes et al. 2000, Cammarano et al. 2003) and the presence of melt alters Vs more than Vp (Karato 2003), similar magnitudes of Vs and Vp anomalies observed by Nyamwandha et al. (2016) can not be explained by temperature variations alone.

The origin of the low-velocity and similar magnitude Vp and Vs anomaly imaged by Nyamwandha et al. (2016) and how this anomaly affects the seismicity of the NMSZ motivates this study. The interpretation of the observed low-velocity anomalies in the tomography studies by Nyamwandha et al. (2016) and Chen et al. (2016) involves not only elevated temperature but also other factors such as the presence of water and compositional variations. However, a formal inversion for the possible factors, temperature, composition, or water content, and its stress implication is lacking.

We, therefore, investigate in this study the possible factors that might explain the low Vp and Vs anomalies of a similar magnitude. The presence of orthopyroxene (Opx) lowers Vp more than Vs (Schutt & Lesher 2010) and provides a possible explanation for the similar magnitudes of the Vp and Vs anomalies in the presence of elevated temperature, which is more sensitive to Vs than Vp (e.g., Goes et al. 2000, Cammarano et al. 2003). Previous studies have reported Opx enrichment over flat subducted slabs (e.g., Wagner et al. 2008, Tang et al. 2012). In the NMSZ, Opx enrichment might have occurred from a flat stagnant piece of the Farallon slab (Sigloch et al. 2008) at mantle transition depths altering the composition of the lithosphere. A similar tectonic situation has been invoked in the North China Craton (NCC) to explain the tomography results by Huang & Zhao (2006), Santosh et al. (2010) in which low P-wave anomalies at upper mantle depths of 100 - 300 km are interpreted as resulting from upwellings from the asthenosphere above the flat Pacific slab in the mantle transition zone. Geochemical evidence by Zhang, Zheng & Zhao (2009), Xiao et al. (2010) in the NCC also supports the interpretation that peridotites have significant fractions of pyroxenes as a result of alteration from the asthenospheric melt (or fluid) interactions.

To test this idea, we first constrain the upper mantle viscosity beneath the NMSZ, assuming that the low-velocity anomalies found in the Nyamwandha et al. (2016) tomography results come from temperature, water, and Opx. We then quantify the effects of these three factors by using the constrained viscosity distributions as input for geodynamic numerical models. We compute differential stresses at seismogenic depths out of the model results and compare the stress effects of all models on the seismicity of the NMSZ.

Seismic Tomography

The tomography results by Nyamwandha et al. (2016) are based on P and S wave arrival times from 519 local earthquakes with $M \geq 2.0$ and travel time residuals from 282 teleseismic earthquakes with $M > 5.5$ occurring between 2011 and 2015. Their reference velocity model, Vp_0 and Vs_0, is shown in Fig. 2.2. The model grid for inversion has the lateral extent shown in Fig. 2.1 with a spacing of 0.4° and a vertical spacing of 10 km in the crust (depth $<$ 40 km) and 40 km in the upper mantle. Only regions with adequate ray-path coverage were interpreted in their results. Several checkerboard and synthetic recovery tests were done by Nyamwandha et al. (2016) to test the reliability of their results. Most of the checkerboard was resolved in the upper mantle with lower resolution in the upper crust. The most striking result from their tomographic inversion is the similar magnitude low Vp and Vs NE-SW trending anomaly in the depth range 100 to 200 km, shown in Fig. 2.3. The synthetic resolution tests substantiated the claim that this feature is well resolved in both Vs and Vp solutions and that the magnitudes of the Vp and Vs anomalies are similar. Based on these tests, we consider the input tomography model to be a reliable foundation for our interpretations and numerical models.

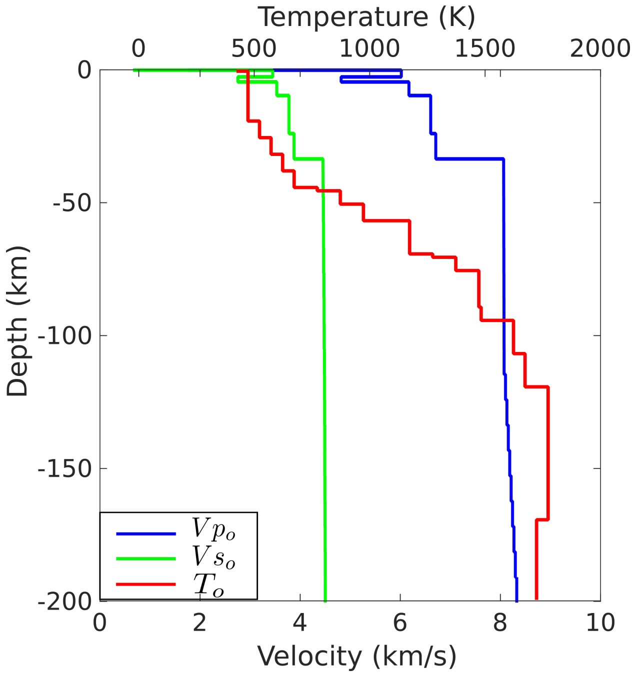

Fig. 2.2: Reference P and S wave velocities (V_{P0} and V_{S0}) used by Nyamwandha et al. (2016) for their tomography results, and reference temperature (T_0) from Zhan et al. (2016), based on which the temperature anomalies are calculated. T_0 is discretized with depth from average geotherm for CEUS (Goes & van der Lee 2002) and is constant within each depth interval.

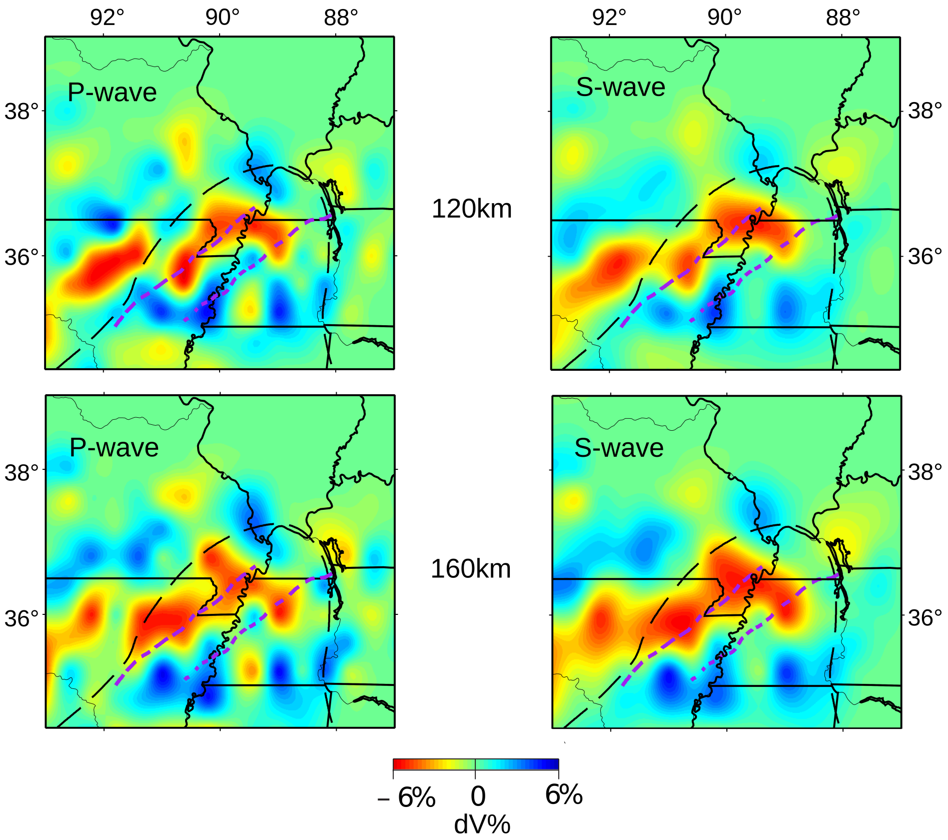

Fig. 2.3: P and S wave tomography results, modified after Nyamwandha et al. (2016), at depth of 120 km and 160 km. Vp and Vs anomalies have similar magnitudes and spatial distributions. Purple and black dashed line marks the reelfoot rift and the Mississippi Embayment, respectively.

Methodology

We calculate the temperature variations, water content, and Opx content that could explain the observed Vp and Vs anomalies, and use them to calculate viscosities. The viscosities are then used in our models to compute differential stress.

Viscosity Calculations

Case I: Temperature only

Effective viscosity for power law creep is given as (Kirby & Kronenberg 1987):

$$\eta_{eff} = \dot{\varepsilon}^{\frac{1-n}{n}} A^{-1/n} \exp\left(-\frac{H}{nRT}\right), \tag{2.1}$$

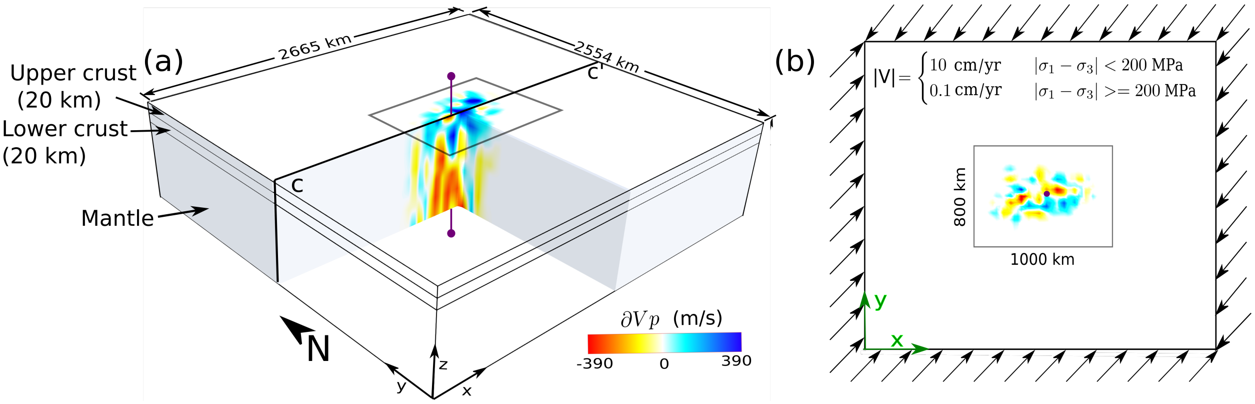

Fig. 2.4: (a) Model domain and the P wave velocity anomalies from Nyamwandha et al. (2016). The domain has 3 layers: 20 km-thick upper crust, 20 km-thick lower crust, and mantle. The purple line through the NMSZ marks the location of vertical profiles of model results shown in the subsequent figures. The rectangle on the surface represents the spatial extent of the tomography model. (b) Model domain representing the S wave velocity anomalies from Nyamwandha et al. (2016) at 100 km depth. Arrows denote the velocity boundary conditions applied on the side walls.

where $\dot{\varepsilon}$ is the effective strain rate taken as $3.25 \times 10^{-17} s^{-1}$ for our calculations (Calais et al. 2006), R is the gas constant, A is the pre-exponential factor, n is the power law exponent, H is the activation energy and T is the temperature. We represent our model domain using three layers and the values of A, n and H as well as density for each layer are listed in Table 2.1. The model is illustrated in Fig. 2.4.

Table 2.1: Rheological constants used in our model simulations

Layer	Composition	Density (kg/m^3)	A (MPa^{-n}s^{-1})	n	H (kJ mol^{-1})
Upper crust^a	Quartzite	2750	$1.1\ e^{-4}$	4.0	223
Lower crust^a	Granulite	2900	$1.4\ e^{4}$	4.2	445
Mantle^b	Olivine	3200	$1.1\ e^{5}$	3.5	530

a : Burov (2010), b : Dixon et al. (2004)

We calculate temperature anomalies using the Vp and Vs anomalies, denoted as ∂Vp and ∂Vs hereafter, determined by Nyamwandha et al. (2016). The sensitivities of Vp and Vs to temperature are based on the anelastic and anharmonic effects in olivine (Ol) given in Goes et al. (2000) and described in the Appendix A.

Case II: Temperature and water content

We assume that mantle temperatures are likely to be lower than the peridotite solidus (T_m) everywhere in the study area, otherwise extensive partial melting would occur for which there are no surface expressions in this region. Moreover, the presence of melt would alter Vs more than Vp (Hammond & Humphreys 2000), but the tomography results for the region show similar magnitudes of ∂Vp and ∂Vs. For only the locations in Fig. 2.5 where temperatures exceed T_m, we assume the presence of water and mantle temperature capped by the olivine solidus. The calculated ∂Vp based temperatures would be higher than the ∂Vs based temperatures for the same anomaly magnitude (Appendix A). Therefore, we use ∂Vp for a liberal estimate of the possible water content. Under these assumptions, a P wave velocity anomaly can be decomposed as follows: $\partial Vp = \partial Vp^{T_m} + \partial Vp^{OH}$, where ∂Vp^{T_m} is the Vp anomaly due to $T_m - T_0$, where T_0 is the reference temperature and ∂Vp^{OH} is the contribution to the Vp anomaly from the water. We use the following relationship between the fluid content and velocity anomaly (Karato & Jung 1998):

$$\delta C_{OH} = -\frac{\partial V^{OH}}{V_o(T,P)} \left(2 \tan \frac{\pi\alpha}{2}\right) \frac{\omega}{\alpha B} \left(\frac{A}{\omega}\right)^{1-\alpha} \exp\left(\alpha\beta \frac{T_m}{T_0}\right), \tag{2.2}$$

where ∂V^{OH} is $\partial Vp - \partial Vp^{T_m} = \partial Vp - \partial Vp/\partial T(T_m - T_0)$, $V_0(T,P)$ is the reference velocity, $\omega = 2\pi$ rad/s, β is related to enthalpy H (in Table 2.1) as $H = \beta R T_m$ (Karato & Jung 1998), $A = B = 8.8 \times 10^6$ and $\alpha = 0.3$, which are all taken from Karato & Jung (1998) for a half space cooling model. δC_{OH} is calculated in ppm H/Si assuming that the reference state has no water content i.e. $C_{OH} = 0$.

The effective viscosity is calculated from the power law creep under the constant strain rate assumption as (Dixon et al. 2004):

$$\eta_{eff} = \dot{\varepsilon}^{\frac{1-n}{n}} \delta C_{OH}^{-\frac{r}{n}} A^{-\frac{1}{n}} \exp\left(-\frac{H}{nRT}\right), \tag{2.3}$$

where δC_{OH} is calculated in Eq. 2.2 and r is the fugacity exponent, assumed to be 1.2 (Hirth & Kohlstedt 2003). All other parameters have usual meaning as in Eq. 2.1, and are listed in Table 2.1. Temperatures, T, are computed as in case I and are taken to be T_m at locations where they exceed T_m.

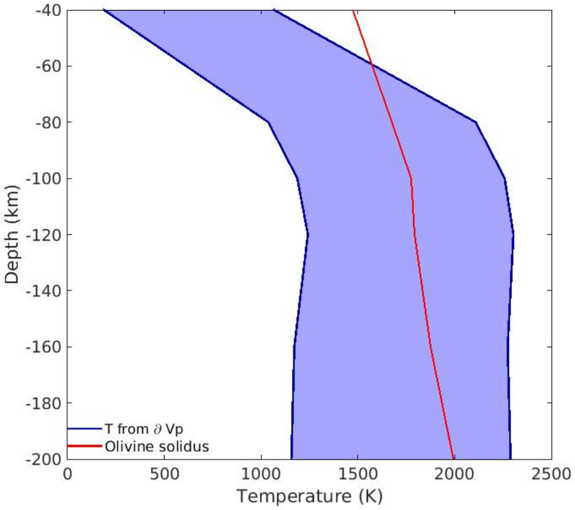

Fig. 2.5: Minimum and maximum temperatures (blue lines) calculated from P wave velocity anomalies as in Case I; and the solidus (red line) from Katz et al. (2003)

.

Case III: Temperature and Opx content

Opx enrichment, together with temperature variations, may explain the similar magnitudes of ∂Vp and ∂Vs because Vp is known to be more sensitive to Opx concentration than Vs (Schutt & Lesher 2010) while Vs is more sensitive to temperature than Vp. We therefore consider the combined effects of Opx and temperature on Vp and Vs anomalies as follows:

$$\partial V_k = \frac{\partial V_k}{\partial T}\,\delta T(X_{Opx}) + \frac{\partial V_k}{\partial X_{Opx}}\,\delta X_{Opx}, \tag{2.4}$$

where V_k denotes Vs or Vp, X_{Opx} is the Opx volume fraction in vol % and T is temperature (K). The coefficients are defined by the Voigt scheme: i.e. in

$$\frac{\partial V_s}{\partial T} = \frac{\partial V_s}{\partial \mu}\frac{\partial \mu}{\partial T} = \frac{1}{2V_s\,\rho}\frac{\partial}{\partial T}\left[(1 - X_{Opx})\,\mu_{Ol} + X_{Opx}\,\mu_{Opx}\right],$$

where ρ is the reference density, μ, μ_{Ol} and μ_{Opx} are shear moduli for the bulk composition, pure Ol and pure Opx, respectively. The sensitivities of elastic moduli to temperature for Ol and Opx are taken from Goes et al. (2000) and the sensitivities of Vp and Vs to Opx content from Schutt & Lesher (2010). We invert the above equations for X_{Opx} and δT simultaneously using the Newton-Raphson scheme assuming that Opx concentration is zero in the reference state.

There is no wide consensus on whether the presence of Opx would generally strengthen or weaken the mantle (e.g., McDonnell et al. 2000, Ji et al. 2001, Sundberg & Cooper 2008, Tikoff et al. 2010, Tasaka et al. 2013, Hansen & Warren 2015). We calculate bulk viscosity in the presence of Opx using a constant strain scheme as $\eta = (1 - X_{Opx})\eta_{ol} + X_{Opx}\eta_{opx}$ (e.g., Ji et al. 2001). In one model, we assume that Opx viscosity is 3.3 times that of Ol (Hansen & Warren 2015) for strengthening effects and in another we construct a model in which Opx viscosity is one eighth of Ol viscosity (Ji et al. 2001) to account for weakening effects of Opx.

Differential Stress Calculations

We construct three-dimensional (3D) models with Maxwell linear viscoelastic rheology to compute differential stresses. Each model has three layers: upper crust (0 - 20 km), lower crust (20 - 40 km,) and mantle (40 - 200 km) (Fig. 2.4a). The depth is restricted to 200 km to model the well sampled regions in Nyamwandha et al. (2016)'s tomography. The lateral extent of our model is 2665 × 2554 km. The central region (gray box in Fig. 2.4a) overlaps with Nyamwandha et al. (2016)'s tomography, but the overall domain is set to be much greater than that of the tomography in order to reduce boundary effects.

To simulate northeast-trending regional compressional principal stress (σ_H) (Zoback & Zoback 1989), horizontal velocities with a magnitude of 10 cm/yr are applied on the X- and Y-axis-perpendicular faces (Fig. 2.4b) until a differential stress ($|\sigma_1 - \sigma_3|$) of 200 MPa is achieved at the depth of 10 km (Zoback et al. 1993, Baird et al. 2010). After that, the boundary velocity magnitude is reduced to 0.1 cm/yr to maintain this stress state without complete viscous relaxation. The top surface is free (i.e., zero-traction), and the bottom has a no-slip condition.

We discretize the domain into a mesh with 227448 hexahedral tri-linear elements using Trelis 15.0. The mesh has lateral and vertical spacing of 25 and 5 km, respectively. We use Pylith (Aagaard et al. 2013), an open-source finite element code for crustal dynamics developed and distributed by Computational Infrastructure for Geodynamics, to calculate stresses and displacements under the loading conditions described above. Differential stress profiles are computed based on stress solutions along a vertical line going through the NMSZ (purple line in Fig. 2.4a).

Model Results

Case I: Temperature only

ΔT_p, temperature anomalies converted from ∂V_p, are plotted in Fig. 2.6 on the cross-section C-C$'$ though the NMSZ as marked on Fig. 2.4. The Vp anomalies from Nyamwandha et al. (2016) along this cross-section are shown in Fig. 2.6a. ΔT_p on this cross-section shows a range of ±600 K (Fig. 2.6b). Viscosity is computed based on the total temperature, which is the sum of the reference temperature profile (Fig. 2.2) and ΔT_p. The viscosity distribution (Fig. 2.6c) follows the pattern of velocity and temperature variations and the minimum is about 10^{20} Pa·s where Vp has the smallest value.

ΔT_s, temperature anomalies converted from ∂V_s, show a magnitude range smaller than that of ΔT_p. ΔT_s is plotted against ΔT_p in Fig. 2.7 for slected depths of 40, 80, 160 and 200 km. If both ∂Vp and ∂Vs are simultaneously explained by temperature anomalies alone, ΔT_p and ΔT_s should be identical, falling on a straight line with a slope equal to 1.

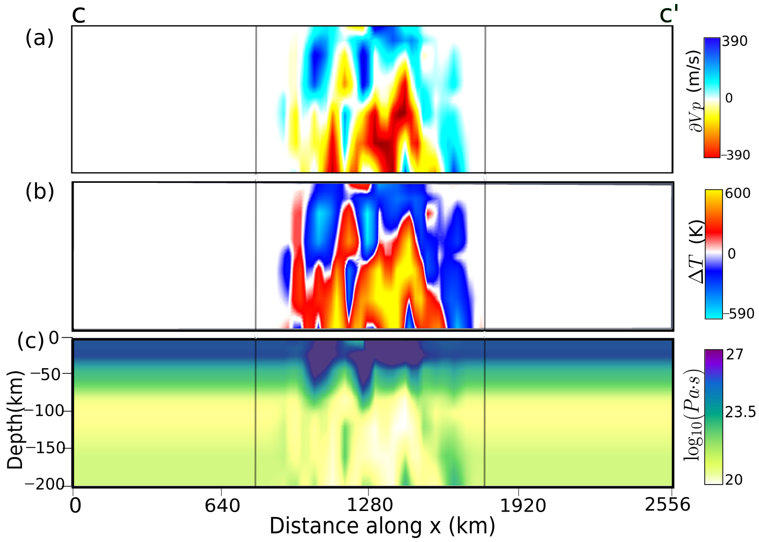

Fig. 2.6: Conversion of the velocity anomalies into model viscosities at cross-section CC' in Fig. 2.4a. Thin vertical gray lines mark the boundaries of the tomography domain of Nyamwandha et al. (2016) (see Fig. 2.4a). Vertical axis is exaggerated by a factor of 3. (a) P-wave velocity anomalies (∂V_p) from Nyamwandha et al. (2016). (b) Temperature anomalies calculated based on ∂V_p. (c) Viscosities computed based on the temperatures anomalies in (b) and the reference temperature shown in Fig. 2.2

.

However, slopes of the best-fitting lines are in the range of 0.5 to 0.7 at all depths, which rejects temperature anomalies as a sole reason for the observed velocity anomalies.

Case II: Temperature and water content

Water contents in the super-solidus regions identified in Case I (Fig. 2.5) are plotted in Fig. 2.8 along cross-section CC′ (marked in Fig. 2.4) and in the 100 km depth layer. The plots show that C_{OH} can be as large as 150 ppm in the regions of maximum temperature (about 2300 K from Fig. 2.5), which also correspond to low V_p regions. The mismatch between the maximum C_{OH}, calculated at depth ∼ 60-90 km, and minimum δVp^{OH} observed between ∼ 100-150 km depth, in the cross section of Fig. 2.8 is because C_{OH} varies inversely with the reference velocity which increases with depth (Eq. 2.2).

Based on the water content present only in the super-solidus regions, we calculate the viscosity distribution using Eq.2.3 and the parameters in Table 2.1 within the NMSZ (Fig. 2.4a). A minor decrease in viscosity is seen only in the depth range from 120 to 160

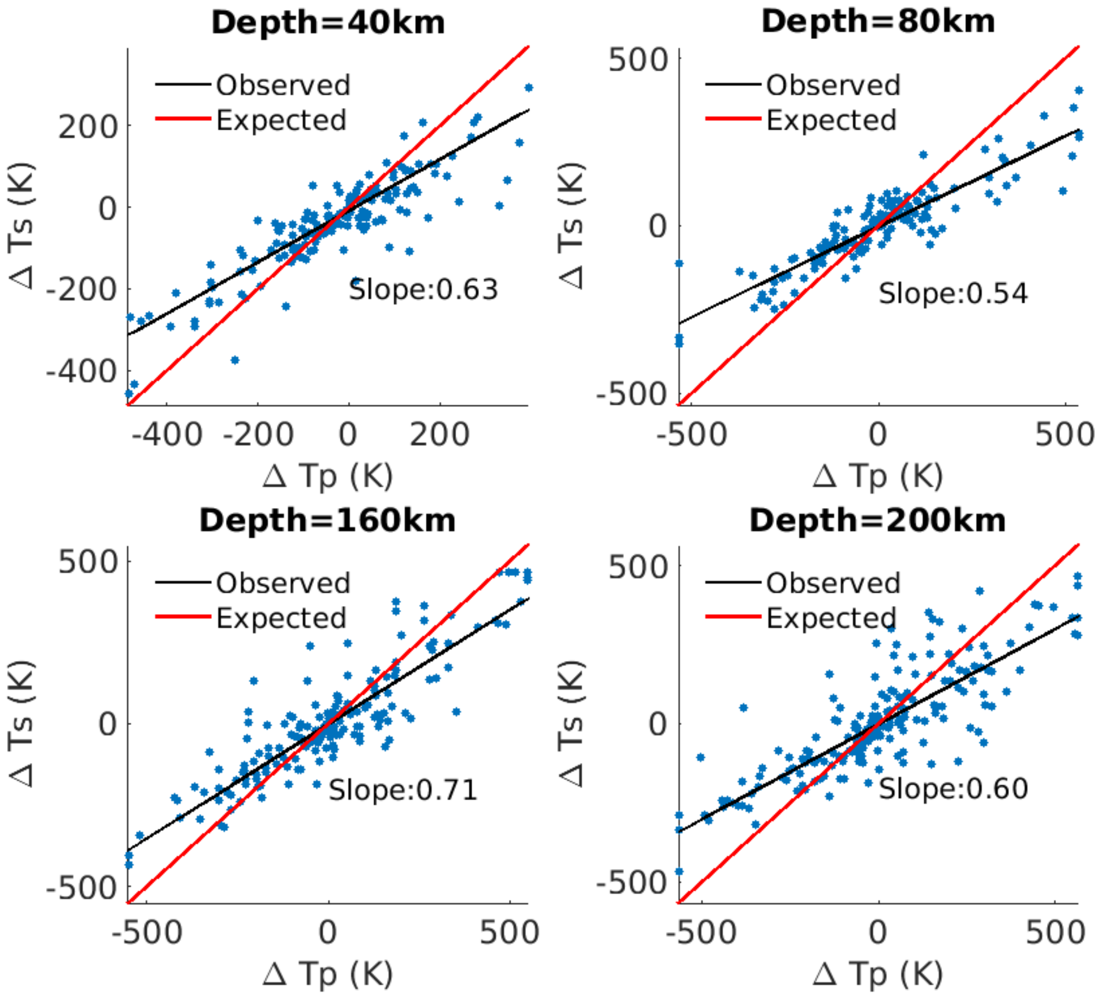

Fig. 2.7: Scatter plots of temperature anomalies calculated from P wave (ΔT_p) and S wave (ΔT_s) anomalies with the best-fitting lines (black). The red line has a slope equal to 1, representing the case where both Vp and Vs anomalies are due to temperature only.

km, where δVp^{OH} is minimum (Fig. 2.8). The associated differential stresses are compared with the dry case (Case I) in Fig. 2.9b. Differential stresses also show only minor differences between Case I and Case II. Although the presence of C_{OH} lowers the required temperatures to explain the high magnitude low velocity anomalies, it cannot explain the similar magnitude of the Vp and Vs anomalies. An increase in water content decreases Vs more than Vp (Table 2 in Karato (2003)). This can also be verified by comparing the C_{OH} contents calculated using P and S wave velocity anomalies and their reference values in Eq. 2.2.

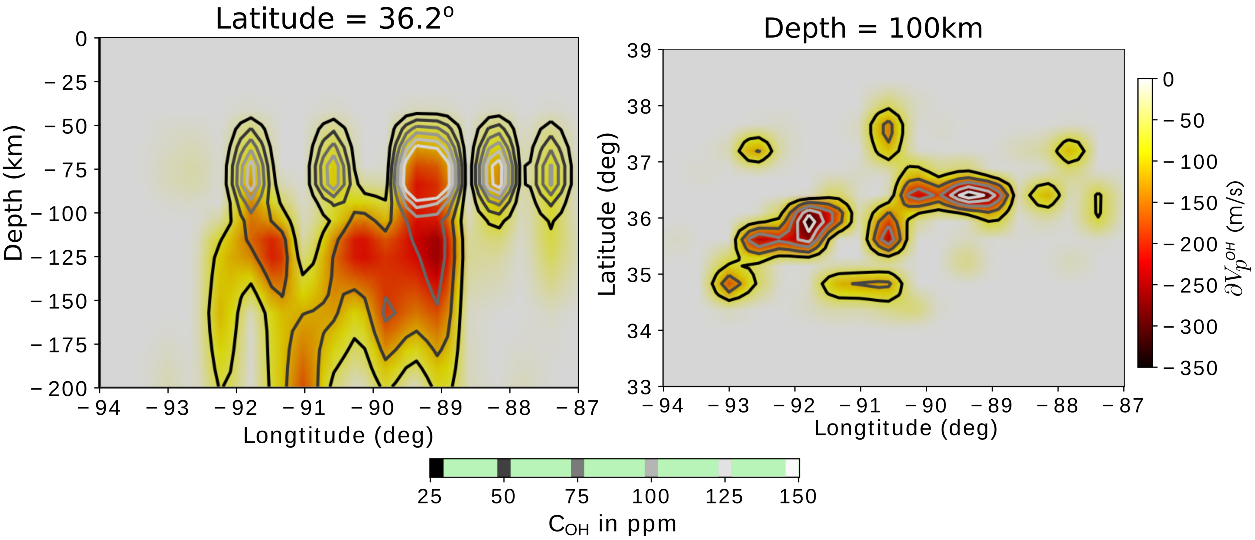

Fig. 2.8: Selectively-added water contents calculated in case II are plotted as contours over the velocity anomalies converted from the temperatures in the super-solidus region on a cross-section along the latitude of 36.2° (left), which approximately coincides with CC' in Fig. 2.4 and on a layer at 100 km depth (right). The higher magnitude negative velocity anomalies correspond to higher calculated water contents.

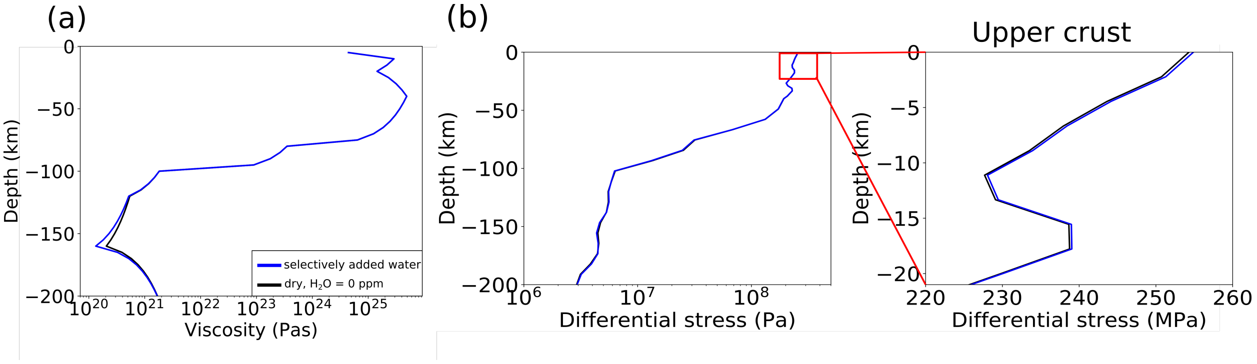

Fig. 2.9: Depth profiles of (a) viscosity (b) differential stresses within the NMSZ (profile location shown by the purple line in Fig. 2.4) for the model with selectively-added water in blue and the model computed from Vp-based temperatures calculated in Case I in black. Differential stresses (b) are zoomed out to observe the concentration in upper crust on the right

.

Case III: Temperature and Opx content

X_{Opx} and ΔT determined from the simultaneous inversion are plotted on two depth slices at 80 and 160 km in Fig. 2.10. Since X_{Opx} is more sensitive to Vp and ΔT is more sensitive to Vs, we plot X_{Opx} and Vp together in the left panels and ΔT and Vs together in the right panels in Fig. 2.10. X_{Opx} values show correlation with negative Vp anomalies, reaching a maximum of 0.4 at 80 km depth and 0.3 at 160 km. Temperature anomalies vary between ± 400 K. This magnitude of temperature anomalies is 20-30 % smaller than that of Case I, dry and Opx-free, where ΔT_p was ± 550K and ± 500K (Fig. 2.7) at the corresponding depths (Fig. 2.6).

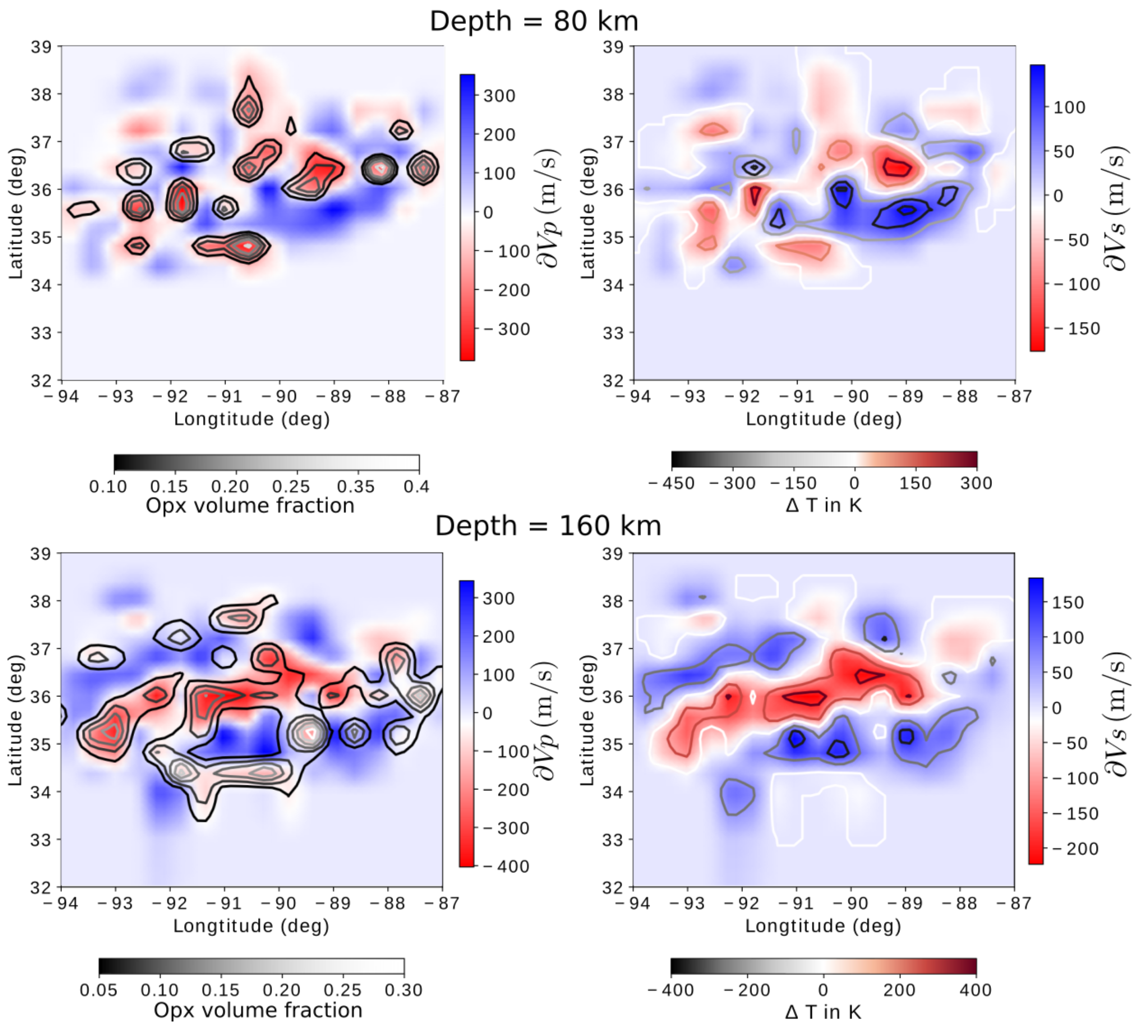

Fig. 2.10: Inverted Opx contents and temperature anomalies at depths of 80 and 160 km. (left) Vp anomalies overlain by the contours of the Opx volume fraction. (right) Vs anomalies overlain by the contours of the temperature variations.

Computed differential stresses show insignificant increasing or decreasing effects due to Opx enrichment (Fig. 2.11a). The sensitivity of viscosity to Opx contents is only loosely constrained (e.g., McDonnell et al. 2000, Ji et al. 2001, Tikoff et al. 2010, Tasaka et al.

2013, Hansen & Warren 2015). Hansen & Warren (2015) suggest a factor of 1.2 to 3.3 increase in viscosity for a pyroxene fraction upto 30 %. Conversely, Ji et al. (2001) indicate a factor of 3 to 8 decrease in the strength of enstatite (the Mg end member of Opx) relative to fosterite (the Mg end member of Ol), for samples containing 0.4-0.6 volume fraction ratio between fosterite and enstatite. Based on these studies, we carry out three different calculations: Opx enrichment increases viscosity by a factor of 3.3 (Hansen & Warren 2015), decreases it by a factor of 8 (Ji et al. 2001), or has no effect. These factors are assumed to be constant for the range of Opx contents determined in this study. Differential stresses computed using these vicosities show only about 1 % variation at all depths including the upper crust, 0-20 km (Fig. 2.11b). However, the presence of Opx has another effect that lowers the magnitudes of temperature anomalies required to explain ∂Vs and ∂Vp. Compared to the water-free Case I model, all the models with non-zero Opx fractions show greater differential stresses in the mantle by about an order of magnitude while smaller differential stresses in the crust by 20-30 MPa (Fig. 2.11).

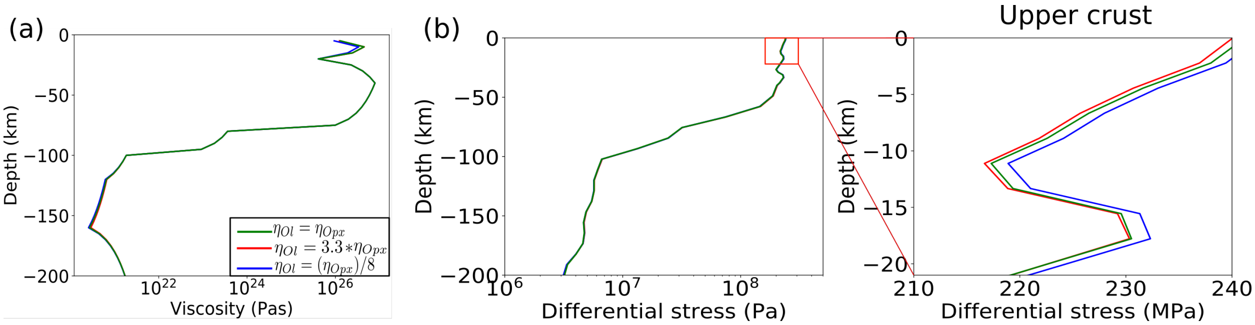

Fig. 2.11: Same as Fig. 2.9 but for the models corresponding to the three possible effects of Opx enrichment on viscosity relative to Ol: Viscosity strengthening (red), viscosity weakening (blue) and the same viscosity as olivine (green).

Discussion

We obtain our results from case III assuming pure Ol as the baseline composition. However, a better approximation to composition of cratonic mantle is harzburgite (85% Ol + 13% Opx + 2% garnet) (McDonough & Rudnick 1998).Consequently, we also calculate Opx content and temperature anomalies from the inversion, assuming harzburgite as the reference upper mantle composition. With the assumed initial Opx concentration in harzburgite, the total Opx content is in the range 40% to 50% localized at depths 80 to 200 km where greatest negative Vp and Vs anomalies are observed. These values in pure Ol case are 40% and 45% at depths 80 and 200 km, respectively. Additionally, the maximum inverted temperatures are reduced by 10 K. Since the inclusion of an initial Opx concentration does not change the results by an appreciable value, we do not show the inversion results with harzburgite as the reference composition. Moreover, the viscosity calculations for Ol are well documented in the literature (e.g., Karato & Wu 1993, Burov 2010) as opposed to other mantle minerals. Therefore, we use pure Ol (or dunite) as the reference upper mantle composition for all of our cases.

We assess the effects of the Reelfoot Rift (Fig. 2.1) on the differential stress by imposing -6 % Vp and Vs anomalies as a conservative measure to represent the weakness in the rift. The rift is modeled as ∼70 km wide on the surface, narrowing to ∼35 km at 10 km depth (Marshak & Paulsen 1996). With the imposed low velocity anomalies, viscosities within the rift are lower than the surrounding areas and therefore, the resultant differential stresses from the model with the rift are lower than the models without rifts. This observation is consistent with the effects of rift zones found by Zhan et al. (2016). We do not show the model results with the rift as we are interested in explaining the cause of the low-velocity anomaly (>50 km depths) and its impact on the NMSZ seismicity. The presence of a rift lowers the absolute differential stress in the upper crust from 230 MPa to 220 MPa at 10 km depth, but does not change the relative impact on differential stress among the cases investigated in this study.

In this study, we do not consider fertility or depletion of the upper mantle as the sole contributor to the velocity anomalies and therefore, to our differential stress calculations. Lee (2003) estimates the effects of fertile mantle (magneisum number, $Mg\# = 100 \times Mg/(Mg + Fe) \sim 86\text{-}88$) and depleted mantle ($Mg\# \sim 93 - 94$) composition on the seismic velocity anomalies. According to this study, a decrease in Mg# significantly decreases the S wave velocity while having no effect on the P wave. The empirical relationship given by Lee (2003): $dVs/d\mathrm{Mg}\# = 0.0143$ km/s, would lead to unrealistically low Mg# (74) for the observed -6% Vs anomalies (discussed in detail by Nyamwandha et al. (2016)). Therefore, fertility of the upper mantle cannot satisfy the observed low and similar magnitudes of Vp and Vs anomalies beneath the NMSZ.

The olivine solidus decreases with water content, up to 5 % for the maximum water content of ~200 ppm H/Si (Karato 2003) computed in case II. This variation is too small and is therefore, ignored in our calculations.

The temperature anomaly calculations described in 2.5 and 2.6 do not include the changes in elastic moduli with pressure. The effects of pressure included in the sensitivity of elastic moduli following Cammarano et al. (2003) leads to 6 and 11 % increase in the calculated temperature anomalies from Vp and Vs respectively, compared to the simplified computations done in this study. This increase translates to about 6% and 10% decrease in Vp and Vs, respectively. We ignore the pressure dependence in temperature calculations for simplicity of implementation in the inversion for Opx content. Instead, we consider constant error bounds in both Vp and Vs anomalies to test the robustness of our interpretation of the tomography results. We introduce an error of ±20% in both P and S wave velocity anomalies to better understand the extent of Opx needed to simultaneously satisfy the Vp and Vs anomalies with these error bounds. In other words, our question is whether Opx enrichment would still be needed if the Vp anomaly is 20 % greater than the value from the tomogrphy and the Vs anomaly is 20 % smaller; or vice versa. The 20% value is chosen as a lenient value for error in the tomography study of Nyamwandha et al. (2016) based on their synthetic and checker-board tests at upper mantle depths (80 - 200 km). A 20 % change in the Vs anomalies largely affects the inverted temperatures by ±80 K while the Opx content varies by just ~ 3%. On the other hand, an increase or decrease in Vp anomalies by 20% results in about a ± 20 K change in temperature and ~ 11% change in Opx volume fraction. This is expected because of the higher sensitivity of Vs to temperature (e.g. Cammarano et al. 2003) and Vp to Opx content (Schutt & Lesher 2006, 2010). When Vs anomalies are altered by a 20 % increase (or 20 % more negative) from the observed tomography, the maximum inverted temperature is 550 K at depths of 160 to 200 km which would cause substantial partial melting at these depths. In addition, Vs would be lowered much more than Vp, increasing the difference between the anomaly magnitudes (Hammond & Humphreys 2000). Therefore, other contributing factors besides Opx and temperature would be needed to explain the altered low Vs anomalies. Conversely, when the altered Vp anomalies are 20% less in magnitude than the observed values from the tomography, the maximum Opx volume fraction computed is 0.3. This is less than the maximum Opx content of 0.41 obtained after inversion using the tomography results, but is still greater than the Opx content (22%) expected in more fertile rocks such as Lherzolite (McDonough & Rudnick 1998). Lherzolite would also contain some clinopyroxene (Cpx) (around 12%) (McDonough & Rudnick 1998) but the presence of cpx has lower partial derivatives of elastic moduli with temperature and pressure than olivine (Cammarano et al. 2003). Therefore, additional Cpx content is unlikely to reconcile the explanation for high magnitude low Vp and Vs velocity anomalies without invoking very high temperatures. After these considerations, we suggest that unless the magnitude of the low Vs anomaly is significantly more (> 20 %) than the Vp anomaly, temperature and Opx enrichment can be simultaneously inverted for the Vp and Vs anomalies giving a reasonable temperature range.

The results shown in this study correspond to the modeling time when the differential stress below the NMSZ is approximately 200 MPa at 10 km depth (e.g. Baird et al. 2010). At this time step, the mean second invariant of strain rate observed at the model surface is 5×10^{-10}/ yr. This value is similar to the strain rate observations from GPS studies, i.e., 3×10^{-9}/yr, by (Boyd et al. 2015). Therefore, our stress calculations produce realistic deformation rates comparable to the observations.

Differential stress calculated in all cases considered in the study is most sensitive to temperature and less so to Opx and water contents. Low differential stresses in the mantle in all the models (cases I-III) are consistent with the high-temperature anomalies and low mantle viscosity values. Relatively strong crust (depths > 40 km) concentrates the differential stress from the deeper mantle. Differential stress in the upper crust calculated from the Opx-enriched cases (case III) appears to be smaller than values computed using forward calculated temperatures (case I and II). This trend is the result of lower temperatures (Fig. 2.10) observed after inversion in case III than the calculated temperatures in case I (Fig. 2.7), implying that the mantle in case I is weaker and concentrates higher differential stress in the upper crust (Fig. 2.12). It can also be observed from Fig. 2.12 that the effects of Opx on differential stress are minor. Capping the maximum temperatures computed from P wave anomalies (ΔT_p) with the olivine solidus and attributing the excess anomalies to water content (case II) has minor effect on the differential stress compared to case I. Therefore it can be inferred from Fig. 2.12 that the differential stress is most sensitive to temperature.

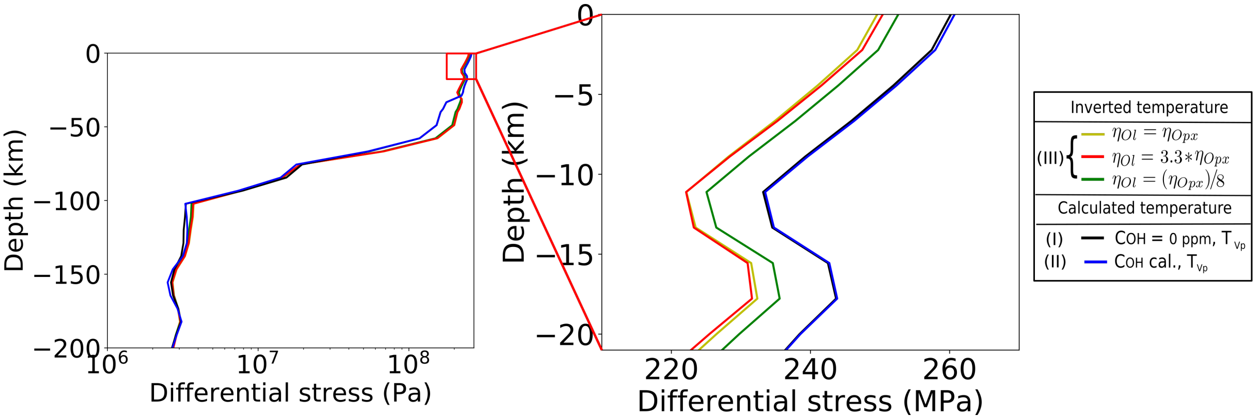

Fig. 2.12: Depth profiles of differential stress from all the cases (Case I to III) presented in this study. Case I: temperatures converted from the ∂V_p (black); Case II: selective addition of water in super-solidus regions and temperature calculated from Case I using ∂V_p (blue); Case III: temperatures inverted using ∂V_p and ∂V_s and Opx for its strengthening (red), weakening (green) and no (yellow) viscosity effects on Opx. The blue and black curves are indistinguishable.

We favor the differential stress calculations with the inverted temperatures and the presence of Opx (Case III) because they can provide the only explanation for the similar magnitudes of the upper mantle Vp and Vs anomalies determined by Nyamwandha et al. (2016). The velocity anomalies cannot be attributed to elevated temperature alone, a more fertile mantle, or to the presence of fluids combined with elevated temperatures; the presence of elevated amounts of Opx is a necessary condition. The inverted values of Opx in the range of 5-40 % (Fig. 2.10) are similar to those found previously for the Kaapvaal Craton (Wagner et al. 2008) and the Colorado Plateau (Li et al. 2008). Metasomatism by Si-rich fluids derived from a subducting slab is the preferred mechanism for Opx enrichment in these regions as documented by the texture and composition of mantle xenoliths (Smith et al. 1999, Bell et al. 2005, Li et al. 2008).

The need for Opx enrichment to provide a reasonable explanation of the similar low Vp and Vs anomalies argues for the presence of a slab below the Mississippi Embayment at some point in time. Flat subduction of the Farallon slab is usually invoked to explain deformation and magmatism during the Laramide orogeny (ca. 80 to 35 Ma) in the western U.S. (e.g., Humphreys 2009) and several studies suggest that flat slab segments are present at depths above 1000 km in the central U.S. (Sigloch et al. 2008, Liu et al. 2008, Sigloch 2011, Schmandt & Lin 2014, Gao & Liu 2014, Porritt et al. 2014). Flattening of the Farallon slab can be attributed to the subduction of oceanic plateaus (the Shatsky and Hess plateaus) located on an old (>50 My) slab (e.g., English & Johnston 2004, Liu et al. 2010). This situation would result in cold slab subduction, facilitating the transport of hydrous minerals to transition zone depths (Maruyama & Okamoto 2007, Kusky et al. 2014, Wang et al. 2018). Geodynamic modeling by Liu et al. (2010) indicates that the top of the Hess plateau is located at a depth of about 660 km below the Mississippi Embayment (Figure 4 in Liu et al. (2010)).

Biryol et al. (2016) attribute a high-velocity upper mantle region located to the east of the NMSZ to the presence of a dense, partially removed, lithospheric drip. The down-going drip may result in upward, return flow of the asthenosphere below the Reelfoot rift (Figure 9 in Biryol et al. (2016)). Our analysis indicates that the Vp and Vs anomalies determined by Nyamwandha et al. (2016) cannot be attributed to the presence of the asthenosphere devoid of Opx enrichment. One possibility that may be compatible with the concept put forth by Biryol et al. (2016) is that the upwelling asthenosphere was enriched in Opx by the presence of a slab fragment that has subsequently dropped to depths just below the transition zone. A deeper slab fragment is suggested by the tomography results of Schmandt & Lin (2014) and by the present location of the Hess oceanic plateau determined by Liu et al. (2010).

Conclusions

In this study, we explore possible explanations for the upper mantle negative Vp and Vs anomalies (∂V_p and ∂V_s) found below the Mississippi Embayment in the tomographic study by Nyamwandha et al. (2016) and suggest Opx enrichment as the most plausible cause for the observed similar magnitudes of the Vp and Vs anomalies. When inverted for Opx volume fraction and temperature anomalies, these low velocity anomalies correspond to positive temperature anomalies up to 450 K and Opx contents up to 40 %. The presence of Opx reduces the range of temperature variations, which is ± 600 K when converted from ∂V_p only. The estimated Opx fraction is in the range of estimates made for central Chile (Wagner et al. 2008) and the Colorado Plateau (Li et al. 2008), which are associated with the water-rock interactions from the Chile-Argentina and Farallon flat slab, respectively. In the upper Mississippi Embayment, olivine alteration to Opx might have been induced by fluids released from the flat-subducted Laramide slab.

We set up numerical viscoelastic models based on the tomography by Nyamwandha et al. (2016) to assess how variations in temperature, water and Opx contents affect the regional stress field in three dimensions. Our results from the numerical models corroborate previous studies indicating that a low viscosity layer will concentrate the stress above it into high viscosity layers (e.g., Kenner & Segall 2000, Zhan et al. 2016). Additionally, the magnitude of differential stress under various combinations of contributing factors to viscosity, (i.e. water content, temperature and Opx content), clearly shows their relative effect on the stress concentration below the NMSZ.

Appendix A

We incorporate the effects of anaelasticity and anharmonicity to calcualte the senitivity of the P and S wave velocity with temperature, $\partial Vp/\partial T$ and $\partial Vs/\partial T$ respectively, following Goes et al. (2000) as:

$$\begin{aligned} \frac{\partial Vp}{\partial T} &= \frac{1}{2Vp_0\,\rho}\frac{\partial K}{\partial T} + \frac{2}{3Vp_0\,\rho}\frac{\partial \mu}{\partial T} + Q_p^{-1}\frac{aH}{2RT_0^2\tan(\pi a/2)}, \\ Q_p &= A\omega^a \exp\left[\frac{a(H+PV)}{RT_0}\right]\frac{3Vp_0^2}{4Vs_0^2} \end{aligned} \tag{2.5}$$

$$\begin{aligned} \frac{\partial Vs}{\partial T} &= \frac{1}{2Vs_0\,\rho}\frac{\partial \mu}{\partial T} + Q_s^{-1}\frac{aH}{2\,R\,T_0^2\tan(\pi a/2)}, \\ Q_s &= A\omega^a \exp\left[\frac{a(H+PV)}{RT_0}\right]. \end{aligned} \tag{2.6}$$

Density is assumed to be constant as its sensitivity to temperature is about 4 orders of magnitude smaller than those of the elastic moduli when the standard value of volume expansion coefficient (10^{-5}/K) is assumed. Table 2.2 lists the values of parameters and relevant quantities. The reference velocities ($\mathrm{Vp_0}$, $\mathrm{Vs_0}$) and the reference temperature ($\mathrm{T_0}$) are depth-dependent (Fig. 2.2). We use the velocity model from Pujol et al. (1997) for the crustal depths (< 40 km) and IASP91 (Kennett & Engdahl 1991) for the mantle (> 40 km). The reference temperatures are taken from Table 2 in Zhan et al. (2016), which are originally from Liu & Zoback (1997) for depths shallower than 100 km and from Goes & van der Lee (2002) for greater depths.

Table 2.2: Elastic moduli, their temperature derivatives and anelasticity parameters

Variable	Symbol	Unit	Value
Bulk modulus[a]	K	GPa	129
Shear modulus[a]	μ	GPa	82
Derivative with temperature[a]	$\partial K/\partial T$	MPa/K	-16
	$\partial\mu/\partial T$	MPa/K	-14
Angular frequency[b]	ω	rad/s	2π
Frequency exponent[a,c]	a	N/A	0.15
Gas constant	R	J/mol·K	8.314
Activation energy[a,c]	H	kJ/mol	500
Volume[a,c]	V	cm^3/mol	20

a: Goes et al. (2000), *b*: based on the frequency range of the tomography by Nyamwandha et al. (2016), *c*: Sobolev et al. (1996).

Chapter 3

Stress concentration in the Central and Southeastern US seismic zones due to upper mantle heterogeneities

This chapter is submitted for publication as Saxena, A., Choi, E., Powell C., and Aslam, K. Stress concentration in the Central and Southeastern US seismic zones due to upper mantle heterogeneities, Geophysical Journal International

Abstract

Sources of stress responsible for earthquakes occurring in the Central and Eastern US (CEUS) must include not only far-field plate boundary forces but also various local contributions. In this study, we model stress distributions due to heterogeneities in the upper mantle beneath the CEUS, including a high-velocity feature identified as a lithospheric drip in a recent regional P wave tomography study. We acquire velocity and stress distributions from numerical models for instantaneous three-dimensional mantle flow. Mantle flow in our models is driven by heterogeneous buoyancy arising from a temperature field converted from the P-wave velocities. The temperature field is also used by a power-law creep rheology assumed in the models. When only the upper mantle heterogeneities are included in a model, differential and Coulomb stress for the dominant fault geometries oriented for failure showed greater magnitudes at some of the seismic zones in the CEUS than in other regions. The model with the lithospheric drip and homogeneous mantle revealed that stress concentrates only in the vicinity of the drip, which includes the Eastern Tennessee Seismic Zone and the northeast arm of the New Madrid Seismic Zone. Our modeling results suggest that the upper mantle heterogeneities below the CEUS have stress concentration effects and are likely to promote earthquake generation at preexisting faults in the region's seismic zones. However, assuming a range of theoretical fault orientations and dips, the most favorable fault geometry for failure from our models are not identical to the fault geometries inferred from the observational studies, suggesting additional factors for earthquake generation in this region.

Introduction

The tectonic setting of the Central and Eastern US (CEUS) includes complex fault systems formed by two continent-scale episodes of rifting and collision (e.g., Keller et al. 1983, Hoffman et al. 1989, Thomas et al. 2006). Within these systems, optimally oriented faults with respect to the present-day regional or local stresses can get reactivated, generating earthquakes (e.g., Zoback 1992, Hurd & Zoback 2012). Indeed, the CEUS is characterized by several intraplate seismic zones including the New Madrid Seismic Zone (NMSZ), the Eastern Tennessee Seismic Zone (ETSZ), the South Carolina Seismic Zone (SCSZ), the Giles County Seismic Zone (GCSZ) and the Central Virginia Seismic Zone (CVSZ) (Fig. 3.1).

Far from the tectonic plate boundaries and known to have low tectonic strain rates (Boyd et al. 2015), the CEUS appears to require local stress contributions to earthquake generation in the active seismic zones. Diverse origins of these local stress contributions have been proposed, many of which involve both crustal and upper mantle heterogeneity. Kenner & Segall (2000) proposed the presence of a weaker lower crustal zone within an elastic lithosphere that acts as a local source of stress concentration. Pollitz et al. (2001) suggested a geodynamic model for the NMSZ consisting of a sinking mafic body in the weakened lower crust that can transfer stress into the overlying elastic crust. Levandowski et al. (2016) showed that stress produced by a high density lower crust below the NMSZ interferes constructively with the far-field tectonic stress, causing optimal stress orientations for earthquake generation. Although the seismogenic depths in the CEUS occur in the upper to middle crust (5 to 30 km) (Vlahovic et al. 1998, Johnston 1996, Mazzotti & Townend 2010), deeper mantle structures can also make a significant contribution to the generation of earthquakes (e.g., Forte et al. 2007, Li et al. 2007, Chen et al. 2014, Nyamwandha et al. 2016, Zhan et al. 2016). Forte et al. (2007) showed that stress concentration below the lithosphere of the NMSZ could be produced by the descent of the Farallon slab using a global geodynamic and seismic tomography based numerical

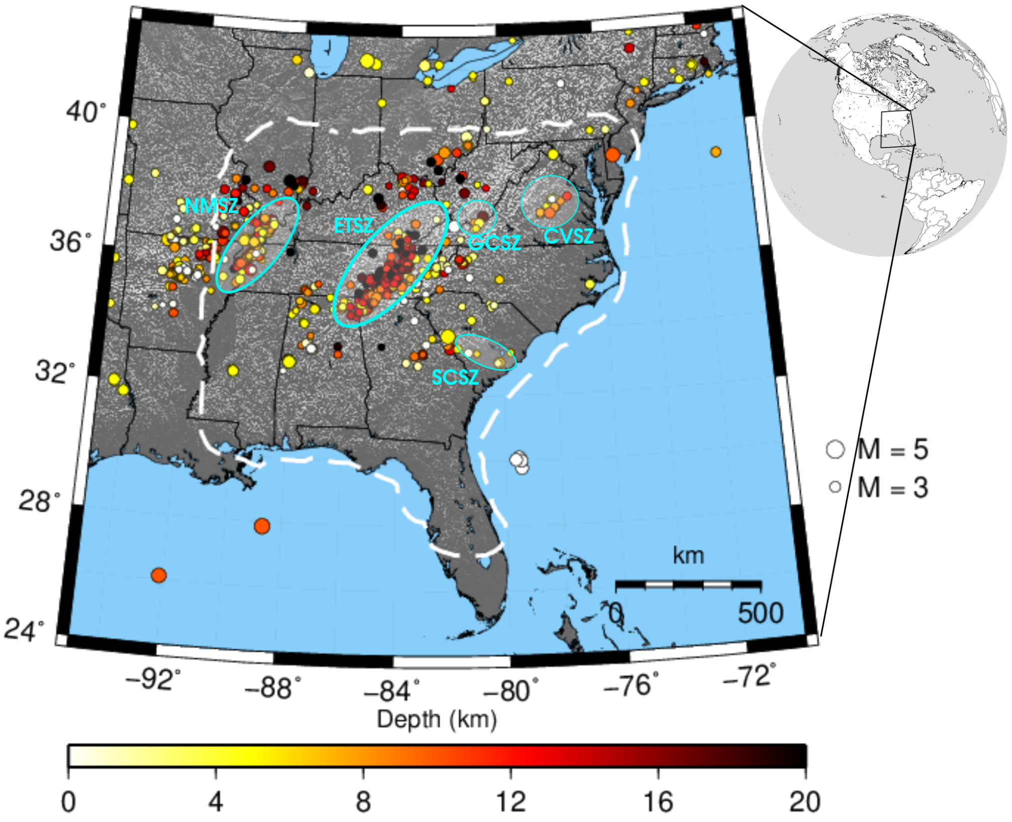

Fig. 3.1: A shaded relief map of the study area including the central and southeastern US seismic zones: New Madrid Seismic Zone (NMSZ), eastern Tennessee Seismic Zone (ETSZ) South Carolina Seismic Zone (SCSZ), Giles County Seismic Zone (GCSZ) and Central Virginia Seismic Zone (CVSZ). White dashed line represents the well-sampled region in the tomography results by Biryol et al. (2016) at a depth 130 km. The earthquakes that occurred over the period December 2011 - December 2018 and had $M_w > 2.5$ are plotted as colored circles. The size and color of a circle represent the event's magnitude and depth. The earthquake catalog is obtained from the United States Geological Survey at `https://earthquake.usgs.gov/earthquakes/search/`.

model. Li et al. (2007) showed that lateral heterogeneity in the lithosphere below the CEUS could concentrate stress in the NMSZ. Chen et al. (2014) and Nyamwandha et al. (2016) independently observed a low P-wave velocity zone at 50-200 km depths below the NMSZ. This was interpreted as a weak zone that acts as a conduit for stress transfer into the crust. Similarly, based on a regional tomography model by Pollitz & Mooney (2014), Zhan et al. (2016) found that weak upper mantle can focus stress in the NMSZ crust.

Similar considerations of crustal and mantle stress sources are yet to be made for other CEUS seismic zones such as the ETSZ, SCSZ, GCSZ, and CVSZ. In a recent high-resolution P-wave tomography study, Biryol et al. (2016) found positive velocity anomalies in the upper mantle beneath the area in-between the ETSZ and the NMSZ at depths of 200 to 660 km, and interpreted them as foundering lithosphere. They further speculated that, since the NMSZ and ETSZ coincide with the boundary of the lithosphere thinned by the drip, they are weakened by the underlying hot asthenosphere and thus prone to seismicity.

In this study, we investigate the effects of the upper mantle heterogeneities found in the P-wave tomography study by Biryol et al. (2016) on the seismicity in the CEUS. We compute stress fields arising from density and strength variations converted from the tomography using instantaneous three-dimensional (3D) mantle flow models. Following previous studies that have demonstrated a correlation between differential stress (e.g., Baird et al. 2010, Zhan et al. 2016) or deviatoric stresses (e.g., Levandowski et al. 2016) with the observed intraplate seismicity, we will consider contributions of the upper mantle heterogeneity to these stress fields and discuss the slip tendency of faults in the seismic zones based on the Coulomb failure criterion (e.g., King et al. 1994, Freed 2005, Li et al. 2007). Ghosh et al. (2019) took a similar approach to explain the intraplate seismicity in the CEUS, but our study differs in the scale of heterogeneity investigated. Ghosh et al. (2019) invoked long-wavelength lateral variations in viscosity structure, which are dependent on the age of the lithosphere, and the location of plate boundaries. In contrast, we consider short-wavelength viscosity contrasts originating from the high-resolution heterogeneities in the upper mantle imaged in Biryol et al. (2016)'s tomography model.

Seismic tomography and upper mantle heterogeneities

We briefly summarize the seismic tomography results by Biryol et al. (2016), including the associated resolution and uncertainties before explaining our numerical models and results. The tomography study by Biryol et al. (2016) is based on direct P and PKPdf residual travel times for the IASP91 earth model (Kennett & Engdahl 1991). The data are collected from 514 stations in the study region (Fig. 3.1) for 753 teleseismic earthquakes occurring between 2011 to 2015 with moment magnitude, $Mw > 5.5$. The discretized model grid has a lateral extent of 30 km in the center and 45 km along the boundary of the domain. The depth extent of the grid is from 36 km to 915 km and consists of 21 layers, but we are only interested in the features extending down to 660 km for this study. The tomographic inversion algorithm by Schmandt & Humphreys (2010) is used along with optimal smoothing and damping constraints to minimize the model norm and data misfit (described in detail in the supplementary information by Biryol et al. (2016)). Only model nodes with high quality (hit points) are used, and therefore, only model results deeper than 60 km depth are interpreted by Biryol et al. (2016).

Biryol et al. (2016) verify their inversion results after robust resolution tests. The checkerboard and synthetic anomaly recovery tests indicate vertical smearing at shallow depths due to the near vertical incidence of the teleseismic raypaths and amplitude loss by about 40 % in the center of the model. Their calculated lateral resolution in the center is about 40 km going to 60 km towards the bottom of the domain, while the vertical resolution is around 50 km at the top and reduces to 65 km at the bottom. They observe some artifacts due to smearing but have overall confidence on the large magnitude (>1 %) and dimensional features. The locations of the smaller dimensional features (∼100 km) are recovered in the synthetic resolution tests, but their outline is smeared laterally and vertically.

The well-sampled region in the tomographic inversion shows high-velocity anomalies with a mean amplitude of 1.9 %, which are interpreted as lithospheric foundering (Fig. 3.2). The two perpendicular cross-sections in Fig. 3.2 show that these anomalies start at about 200 km depth with lateral dimensions of 2° and extend to 660 km where they widen to about 3° (marked in Fig. 3.2A). According to the synthetic anomaly tests, the supposed foundering lithospheric drip with these amplitudes and dimensions should be reliably resolved, and therefore, reliable for our numerical model inputs.

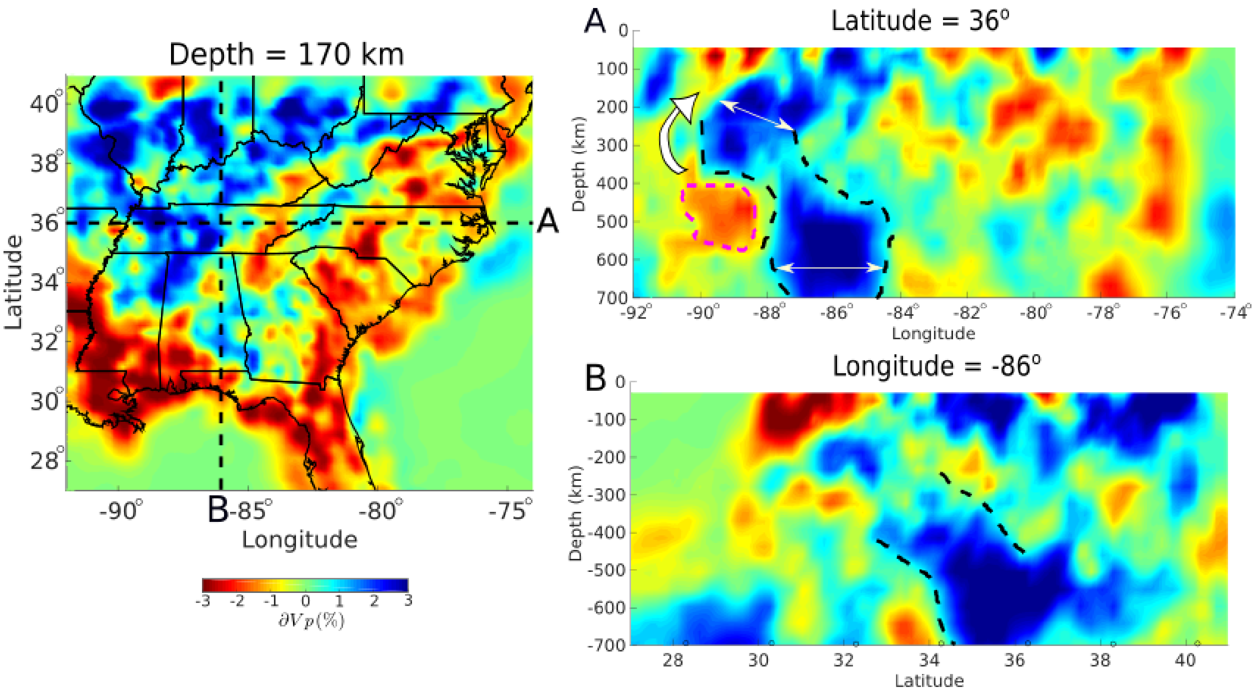

Fig. 3.2: P wave tomography results of (Biryol et al. 2016) at a depth of 170 km. Panels A and B are cross-sections at 36° latitude and −86° longitude, respectively. Dashed black lines on the cross-sections mark the approximate boundaries of the high-density anomalies interpreted as a foundering lithospheric root. Dashed magenta lines on A indicates the low-velocity region interpreted by Biryol et al. (2016) as asthenospheric return flow due to the foundering lithosphere. The white arrow on A shows the direction of the return flow as speculated by Biryol et al. (2016).

Modeling instantaneous mantle flow

Temperature Calculations

Inferring temperature from the seismic velocity anomalies has primary importance for our modeling approach because it will determine both the driving buoyancy force and the viscous resistance. We follow Cammarano et al. (2003)'s approach to calculate temperatures from the seismic velocity anomalies. This approach takes into account the effects of anharmonicity (i.e. elasticity), anelasticity and the phase transition at 410 km depth. Inversion of seismic tomography results to a temperature field is commonly regarded as a non-linear problem due to the shear anelasticity of seismic waves (Minster & Anderson 1981, Karato 1993, Sobolev et al. 1996, Goes et al. 2000, Artemieva et al. 2004) and non-linear sensitivity of elastic moduli and their pressure derivatives to temperature

(Duffy & Anderson 1989, Anderson et al. 1992, Cammarano et al. 2003, Stixrude & Lithgow-Bertelloni 2005). The presence of melt or water may also introduce non-linearity in temperature effects on seismic velocities (Karato & Jung 1998) but the effects of melt and fluids are not considered in this study because of the lack of high heat flow or other substantial evidence for melting in this region of the mantle (Blackwell et al. 2006). Our inversion procedure is fully detailed in Appendix B.

Velocity anomalies and the inverted temperatures for depths of 200 km and 605 km are shown in Fig. 3.3. P-wave velocity (Vp) sensitivity to temperature is found to be −0.85 % per 100°K and −0.55 % per 100°K at depths 200 km and 605 km, respectively. These values are consistent with those in (Cammarano et al. 2003): −0.75±0.15 % per 100°K and −0.65 % per 100°K at the same depths, along the mantle adiabats 1300°C and 1600°C, respectively, used in this study.

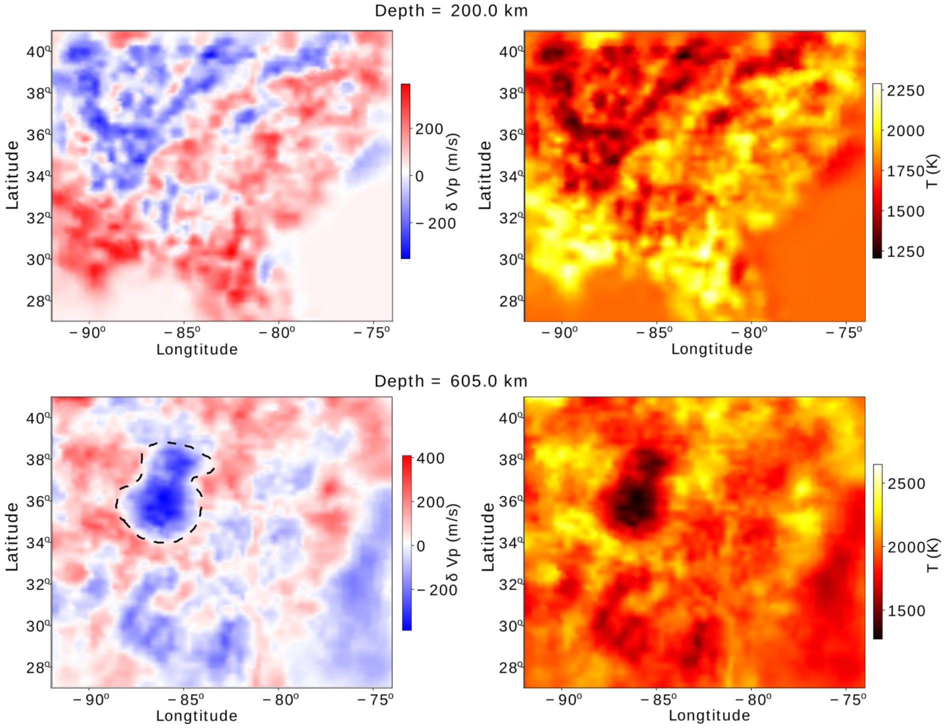

Fig. 3.3: P wave anomalies (left) from Biryol et al. (2016) and the inverted temperatures (right) at depths of 200 (top) and 605 km (bottom). Black dashed line in the depth layer 605 km marks the boundary of the high-velocity structure interpreted as a foundering drip by Biryol et al. (2016).

Model Setup

We compute velocity and stress fields that are in equilibrium with heterogeneous buoyancy forces arising from the heterogeneous distribution of temperature-dependent density. For this calculation, we use an open-source finite element code, ASPECT version 2.0.0 (Heister et al. 2017, Kronbichler et al. 2012, Bangerth et al. 2018). ASPECT can solve the equations for the conservation of mass, momentum, and energy using an adaptive finite element method for a variety of rock rheologies.

Our model domain is laterally bounded by longitudes, 71°W and 95.5°W and by latitudes, 23°N and 43°N. The depth range is from 0 to 660 km (Fig. 3.4). Since the tomography model considers only the mantle starting from a depth of 36 km, we assume a temperature distribution appropriate for the crust. We divide the crust into four depth layers such that the temperature is constant in each layer (Fig. 3.4). The domain is discretized into 0.512 million hexahedral elements with a 0.15° resolution in longitude, 0.125° in latitude and 35 km in depth. This spatial resolution is similar to that of the tomography and thus sufficient for resolving the mantle velocity structure shown by the tomography model.

We assessed mesh resolution effects by running a model with a twice finer mesh having 2.048 million elements and found that differences in the results were small, amounting to a relative error of 2% in the velocity field. All the model results presented in this study are thus based on the coarse mesh for computational efficiency. We also tested a model with an additional lateral area of 5° by 5° surrounding our domain to asses boundary effects. The overall resultant velocity and stress field are similar to those for the smaller model domain, but the magnitude of the calculated stress and velocity field at our depth of interest (15 km) near the boundaries is smaller by 10-15 % because the viscous effect of the same heterogeneity is now spread over a larger area. However, since the seismic zones are sufficiently far from the model domain boundaries, we show only the results for the smaller domain.

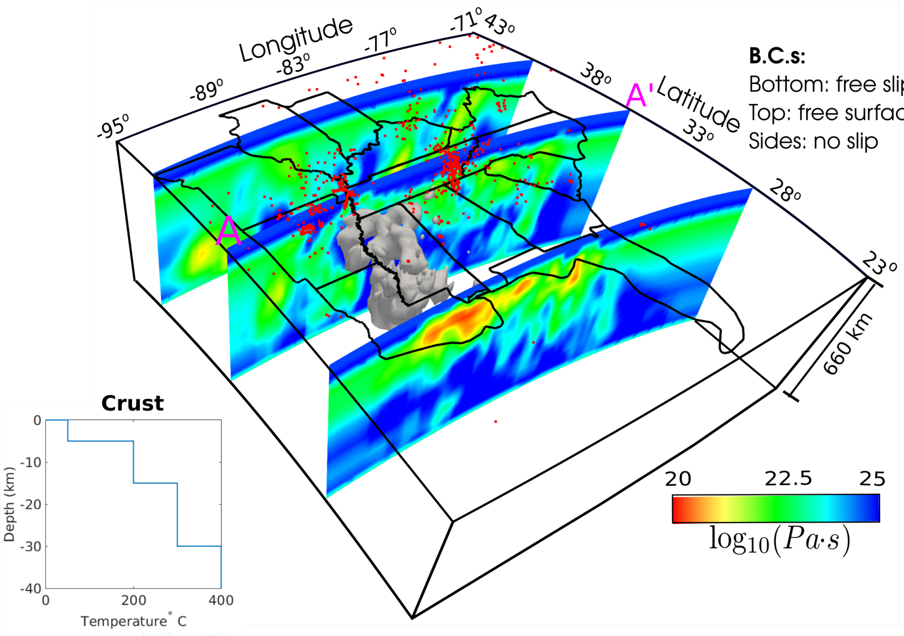

Fig. 3.4: Model setup with the computed rheology based on the regional tomography by Biryol et al. (2016) and the boundary conditions applied. Gray isosurface represents P-wave anomalies > 2 % in the region interpreted as lithospheric foundering. Instantaneous flow along slice AA' passing through the ETSZ and NMSZ is discussed in Fig. 3.12. Black lines indicate the state boundaries and red dots are epicenters for the earthquake catalog used in Fig. 3.1. Temperature depth profile of the crust is shown on the left.

Upper mantle flow is assumed to occur by a dislocation creep at low temperatures relative to the melting temperatures of mantle rocks and by a diffusion creep at higher temperatures (e.g., Gordon 1967) with respect to the melting temperatures. Our model employs both dislocation and diffusion creep with each type having different contributions depending on the temperature and pressure. In this rheology model, the effective viscosity (η_{eff}) is computed as (Billen & Hirth 2007):

$$\eta_{\text{i}} = \frac{1}{2} A^{-1} n_i d^{\frac{m_i}{n_i}} \dot{\varepsilon}_i^{\frac{1-n_i}{n_i}} \exp\left(\frac{E_i + PV_i}{n_i RT}\right), \; i = \text{diff or dis}, \tag{3.1}$$

$$\eta_{\text{eff}} = \left(\frac{1}{\eta^{\text{diff}}} + \frac{1}{\eta^{\text{dis}}}\right)^{-1}, \tag{3.2}$$

where diff and dis denote diffusion and dislocation creep, A_i is the pre-exponential factor, n_i is the power law exponent, d is the grain size, m_i is the grain size exponent, $\dot{\varepsilon}$ is the second invariant of the strain rate tensor, R is the gas constant, T is temperature obtained from the inversion of the Vp anomalies, P is pressure, and E_i and V_i are the activation energy and volume, respectively. All the parameter values used in this study are given in Table 3.1.

Table 3.1: Values for dislocation and diffusion creep

Parameter	Symbol	Unit	Diffusion Creep	Dislocation Creep
Pre-exponential factor[a]	A	s^{-1}	1.5×10^{-16}	0.3×10^{-22}
Power law exponent[a]	n		1	3.5
Grain size exponent[a]	m		2	0
Activation energy[a]	E	kJ/mol	300	530
Activation volume[a]	V	cm^3/mol	6	20
grain size[b]	d	mm	5	5

[a] Karato & Wu (1993). [b] Approximate value for olivine (Karato 1984).

The bottom boundary at 660 km has the free-slip condition (e.g., Arcay et al. 2007, Billen & Hirth 2007, Quinquis et al. 2011). For side boundaries, we tested our model with both free-slip and no-slip conditions and verified that the velocity fields at the seismic zones have the same pattern with up to 5% magnitude difference. In this study, we only show the results for the no-slip conditions. We let the top boundary be a free surface that can develop topography in response to the instantaneous flow in the mantle.

Differential and Coulomb stress changes

We define static changes in Coulomb stress (ΔC) of a model with respect to another model as the difference in Coulomb Failure Function (CFF) (King et al. 1994):

$$\Delta C = \Delta\tau - \mu'\Delta\sigma_n, \tag{3.3}$$

where $\Delta\tau$ and $\Delta\sigma_n$ are the difference between the models in shear (positive in the direction of slip) and normal (positive when compressive) stress, respectively, for a particular fault orientation, and μ' is the effective coefficient of friction after accounting for pore pressure. Since we do not have sufficient constraints on the effective friction coefficients for the faults in the study area, we use a value of 0.6 based on the study by Hurd & Zoback (2012).

Differential stress, $\sigma_{\text{diff}} \equiv \sigma_1 - \sigma_3$, is compared between different models with a similarly defined quantity, $\Delta\sigma_{\text{diff}}$.

Stress tensors in the model outputs are given as Cartesian stress components with respect to x and y axes at 0° and 90° longitudes and on the equator. Stress tensors are transformed according to a rotation of the model domain by which the z axis goes through the center of the domain. After this rotation, x and y axes approximately coincide with East and North as understood in the model. Stress tensors are further transformed such that x, y and z axes in the rotated Cartesian system coincide with a fault's strike, up-dip and normal directions (Fig. 3.5). We follow the convention that strike is defined as the direction that puts a dipping fault plane on the right and dip angle changes between 0° and 90°. In the final coordinate system, negative values of τ_{zx} and τ_{zy} correspond to right-lateral and down-dip sense of motion, respectively.

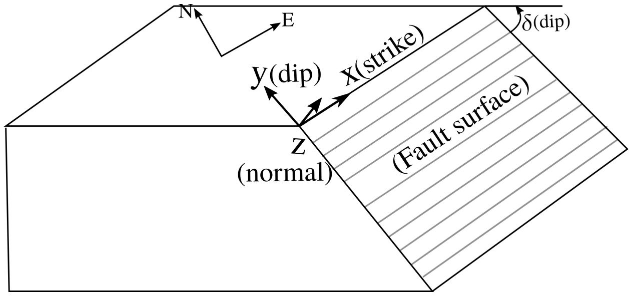

Fig. 3.5: Cartoon sketch showing the sign convention for the strike, dip, and normal to the fault surface.

To facilitate comparison of models with and without the local upper-mantle heterogeneity, delineated by the velocity anomaly isosurface in Fig. 3.4, we denote the model with tomography-based temperatures plus the reference geotherm as HT (HeTerogeneous), a model with the reference geotherm in the upper mantle as HM (HoMogeneous), and a model identical with HT except that the temperature within the foundering lithosphere is replaced with the reference geotherm values as HR (Heterogeneous but having no Root). HT−HM represents the contributions from the upper mantle heterogeneity, while HT−HR shows only the contribution of the high-velocity structure interpreted as the foundering drip. Fig. 3.6 shows a cross-section of the tomography illustrative of these model setups. Coulomb stress changes, ΔC_{HT-HM} and ΔC_{HT-HR}, indicate whether and how much the stress field in the model HT would promote the slip tendency of a fault relative to stress fields in HM and HR. For instance, a positive ΔC_{HT-HM} for a fault geometry and a sense of motion means that the mantle heterogeneities considered in HT promote the failure of the fault relative to the laterally homogeneous mantle (HM).

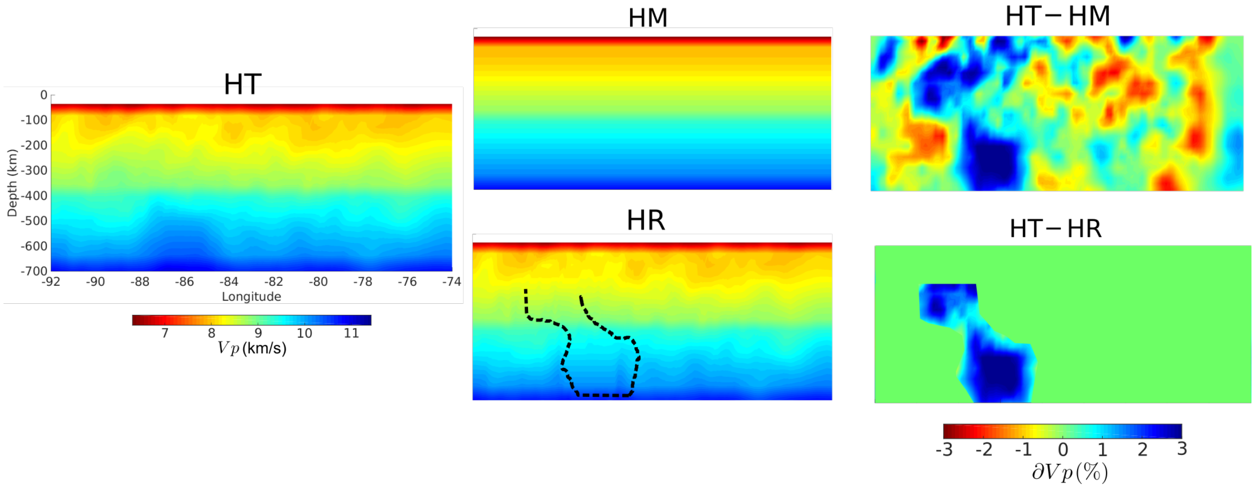

Fig. 3.6: Cross-section along latitude=36° across model setups for which stress calculations are done in this study. HT, HM, and HR represent the HeTerogeneous, Homogeneous Mantle and Homogeneous Root models, respectively. The models, HT−HM and HT−HR isolates the effects of upper mantle heterogeneity and lithospheric drip, respectively.

We calculate ΔC and $\Delta\sigma_{\text{diff}}$ for HT−HM and HT−HR, and analyze the results at the approximate locations of the seismic zones: ETSZ, SCSZ, CVSZ, GCSZ, and the northeastern arm of the NMSZ (NMSZ_NE) (shown in Fig. 3.7) which are contained in the well-resolved region in the Biryol et al. (2016) tomography. CFF values are computed for the optimal fault geometries based on the focal mechanisms and earthquake relocations at 15 km depth in all the seismic zones (Table 3.2).

Table 3.2: Seismic Zones* and their associated dominant fault geometries

Seismic Zone	Strike, Dip	Sense of motion	Reference
NMSZ_NE	N10°E, 90°	right-lateral	Chiu et al. (1992), Shumway (2008)
ETSZ	1- N10°E, 90°; 2- E-W, 90°	right-lateral; left-lateral	Chapman et al. (1997), Cooley (2015), Powell & Thomas (2016)
GCSZ	E-W, 90°	left-lateral	Munsey & Bollinger (1985)
CVSZ	N30°E, 50°SE	thrust	Wu et al. (2015)
SCSZ	N180°E, 40°W	thrust	Chapman et al. (2016)

* NMSZ_NE: North eastern arm of New Madrid Seismic Zone; ETSZ: Eastern Tennessee Seismic Zone; GCSZ: Giles County Seismic Zone; CVSZ: Central Virginia Seismic Zone; SCSZ: South Carolina Seismic Zone.

Model results

The upper mantle heterogeneity results in increased differential stresses at crustal depths and at the CEUS seismic zones. $\Delta\sigma_{\mathrm{diff}}^{\mathrm{HT-HM}}$ is plotted in Fig. 3.7a for the depth of 15 km, at which seismicity in the study area is most frequent (e.g., Mazzotti & Townend 2010). The seismic zones, ETSZ, SCSZ, GCSZ, CVSZ, and NMSZ are correlated with positive $\Delta\sigma_{\mathrm{diff}}^{\mathrm{HT-HM}}$ in the range of 30 to 40 MPa (Fig.3.7b). The areas F_1 and F_2 marked on Fig.3.7a do not show active seismicity but $\Delta\sigma_{\mathrm{diff}}^{\mathrm{HT-HM}}$ is greater than 70 MPa. In contrast, $\Delta\sigma_{\mathrm{diff}}^{\mathrm{HT-HR}}$ shows only small positive values, 2 to 4 MPa in the horseshoe-shaped region surrounding the drip, which partially overlaps with the ETSZ and NMSZ (Fig.3.7b). The presence of upper mantle heterogeneity increases the Coulomb stress in all of the seismic zones for their respective optimal fault orientations listed in Table 3.2. $\Delta\sigma_{\mathrm{diff}}^{\mathrm{HT-HM}}$, Coulomb stress changes for HT−HM are about 5 MPa in the GCSZ and in the ETSZ for their optimal fault orientations (Fig. 3.8a). On the other hand, $\Delta\mathrm{C}_{\mathrm{HT-HM}}$ for a vertical right-lateral fault striking N10°E indicates that the mantle heterogeneities reduce the slip tendency in the ETSZ but slightly increase it in the NMSZ_NE (Fig. 3.8b). $\Delta\sigma_{\mathrm{diff}}^{\mathrm{HT-HM}}$ is about 20 MPa for the thrust motion on the dominant fault orientations in the CVSZ and the SCSZ (Fig. 3.8c,d).

Coulomb stress changes due to the lithospheric drip ($\Delta\mathrm{C}_{\mathrm{HT-HR}}$) are mostly negative or weakly positive at all the seismic zones for their respective dominant fault orientations

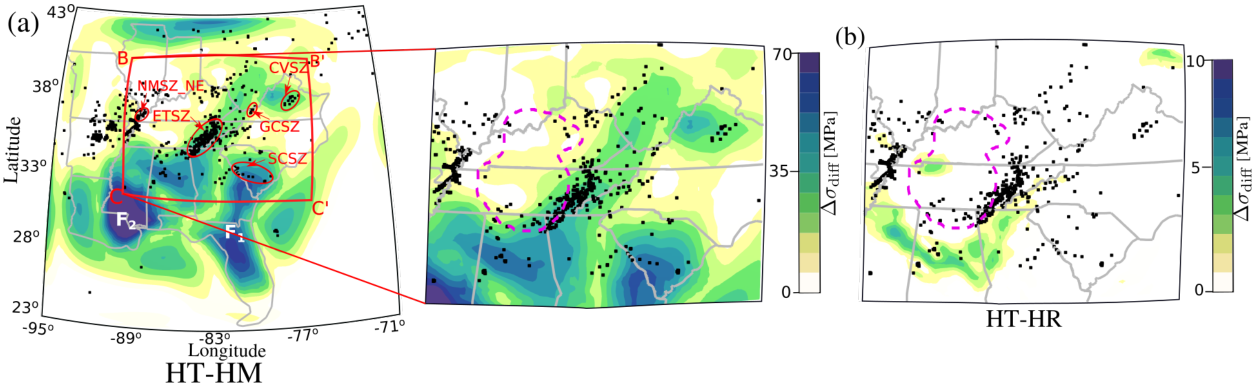

Fig. 3.7: (a) Differential stress changes in the HT−HM case ($\Delta\sigma_{\text{diff}}^{\text{HT}-\text{HM}}$) at a depth of 15 km. Black dots are earthquake epicenters from USGS data between 2011-2018. Gray lines denote the US state boundaries. Seismic zones investigated in this study are the northeastern arm of the New Madrid Seismic Zone (NMSZ_NE), Eastern Tennessee Seismic Zone (ETSZ), South Carolina Seismic Zone (SCSZ), Giles County Seismic Zone (GCSZ) and Central Virginia Seismic Zone (CVSZ). F_1 and F_2 indicates the areas of anomalously high values of $\Delta\sigma_{\text{diff}}^{\text{HT}-\text{HM}}$. Dashed magenta line marks the boundary of the foundering at 605 km depth. The box BB'CC' indicates the region enlarged in subsequent figures. (b) Differential stress change for HT−HR ($\Delta\sigma_{\text{diff}}^{\text{HT}-\text{HR}}$) in a region centered on the ETSZ.

(Fig. 3.9). $\Delta C_{\text{HT}-\text{HR}}$ tends to be confined to an area surrounding the drip making relatively greater impact on the ETSZ and NMSZ than on the other seismic zones further east. $\Delta C_{\text{HT}-\text{HR}}$ is about 1-2 MPa in the NMSZ_NE for its dominant fault orientations (Fig. 3.9b) but decreases at the ETSZ for both of the dominant orientations (Fig. 3.9a, b). The GCSZ, CVSZ and SCSZ are located too far from the drip to have significant $\Delta C_{\text{HT}-\text{HR}}$ (Fig. 3.9a, c and d).

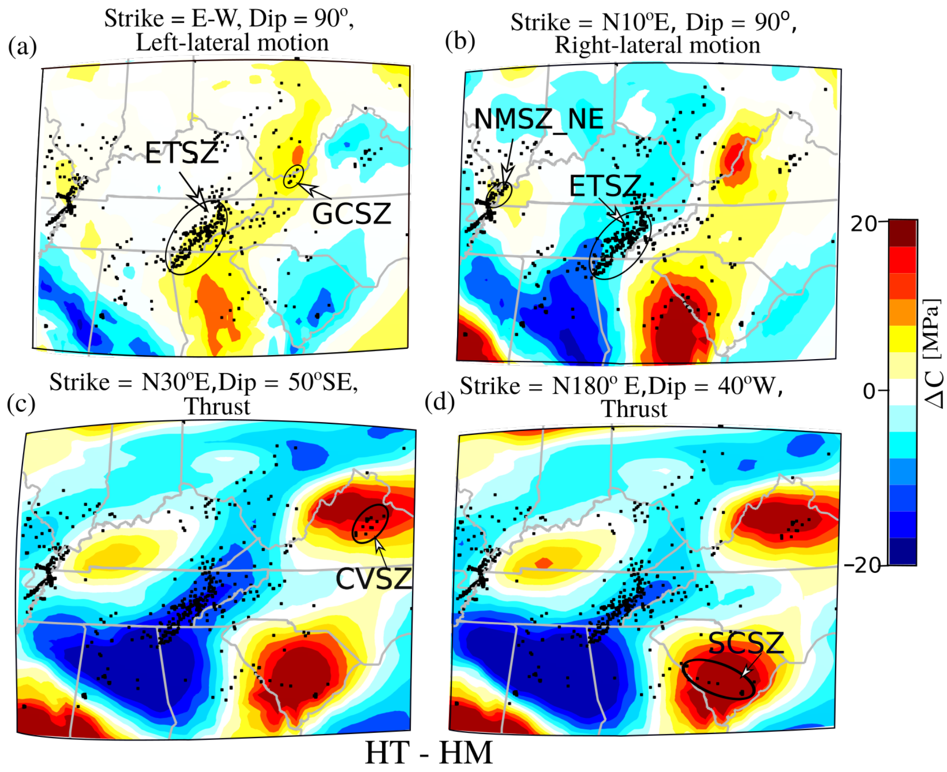

Fig. 3.8: Coulomb stress change (ΔC) for HT−HM calculated for different fault orientations in Table **??**) at 15 km depth. Seismic zone(s) and their corresponding optimal fault geometries are mentioned for each subplot: (a) Eastern Tennessee Seismic Zone (ETSZ) and Giles County Seismic Zone (GCSZ), left lateral vertical fault striking EW, (b) ETSZ and North-eastern arm of the New Madrid Seismic Zone (NMSZ_NE) and right lateral vertical fault strikingt N10°E, (c) Central Virginia Seismic Zone (CVSZ) and thrust fault dipping 50° SE striking N30°E, (d) South Carolina Seismic Zone (SCSZ) and thrust fault dipping 40° W striking N-S.

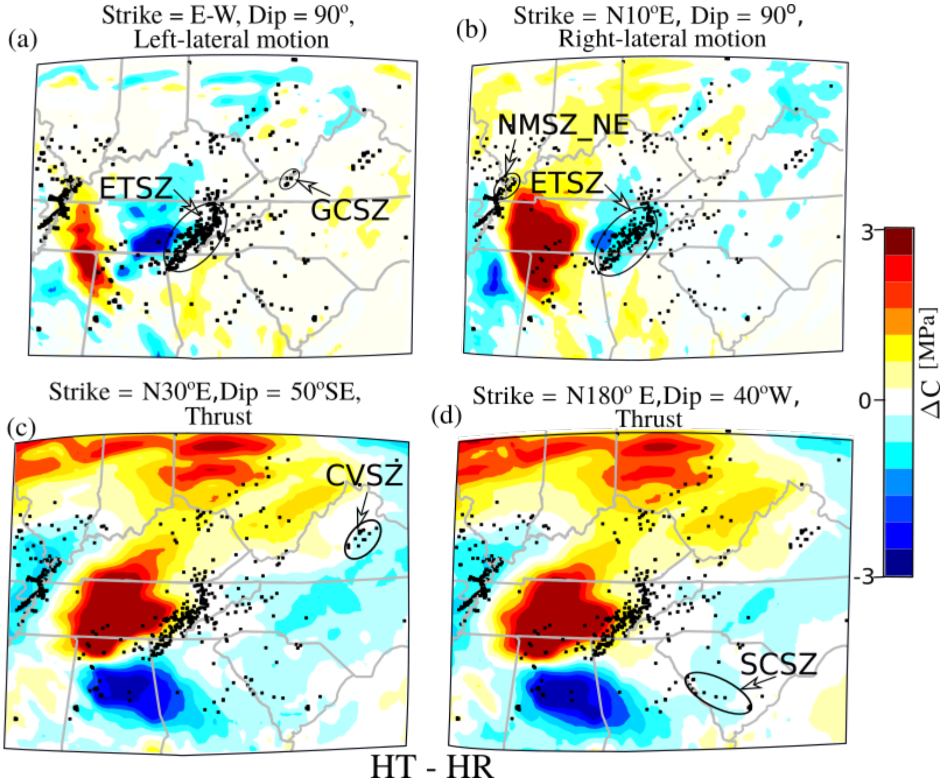

Fig. 3.9: Same as Fig. 3.8 but for HT−HR.

Discussion and Summary

Changes in differential stress ($\Delta\sigma_{\mathrm{diff}}$) and the Coulomb stress (ΔC) for the cases HT−HM and HT−HR quantify how the upper-mantle heterogeneity and the lithospheric drip, respectively, can contribute to the seismicity in the ETSZ, GCSZ, CVSZ, SCSZ and NMSZ (see Fig. 3.1 for their locations). $\Delta\sigma_{diff}^{\mathrm{HT-HM}}$ involves the combined effects of all the mantle heterogeneities relative to the laterally homogeneous reference mantle and shows positive values up to 30 MPa in all of the seismic zones considered (Fig. 3.7a). On the other hand, the lithospheric drip alone has an area of influence that includes only the ETSZ and NMSZ as $\Delta\sigma_{diff}^{\mathrm{HT-HR}}$ shows positive values of about 3 MPa in these locations. Although the positive values of differential stress changes suggest an increased potential for seismicity, even the greatest value of $\Delta\sigma_{diff}^{\mathrm{HT-HM}}$, $\sim$ 30 MPa in the ETSZ, is an order of magnitude less for that required for the nucleation of earthquakes at crustal depths of 10-20 km (e.g. Sibson 1990). This deficiency in magnitude requires other contributions for explaining the seismicity in the CEUS like weak existing faults created during the past several Wilson cycles (Thomas et al. 2006)). From our Coulomb stress change calculations for the optimal fault geometries of the seismic zones (Table 3.2), we find that these faults are more loaded towards failure in the hetetogeneous upper mantle revealed by the tomography than in the laterally uniform one.

Stress concentration occurs along the edges of rheology changes as previously proposed by Zhang, Sandvol & Liu (2009). To test this, we considered a model with the drip shifted to the east such that it begins below the ETSZ and not between the NMSZ and the ETSZ. The stress increase for the shifted root model surrounds the ETSZ and does not correlate with any observed seismic zones. This result is a special case of the general behavior that stress concentrates at a boundary of large lateral viscosity changes (2 to 3 orders magnitude in Fig. 3.4). Since the viscosities are computed based on the temperatures inverted from the Vp anomalies, the location of the foundering lithospheric drip has an impact on concentrating the differential stress at the surrounding seismic zones, the ETSZ and the NMSZ.

The optimally oriented fault planes based on our model results do not perfectly coincide with the focal mechanism solutions in the seismic zones (Fig. 3.10). Defining the optimal fault orientation as the one maximizing the Coulomb stress changes of HT relative to HM ($\Delta C_{\mathrm{HT-HM}}$), we employ a simple grid search over strikes from N90°E to S90°E and dips from 10° to 90° at an interval of 10° for the possible senses of motion, right- and left-lateral strike-slip, normal and thrust faulting (Fig. S1). There are several reasons for the mismatch between the focal mechanism solutions and the optimal fault orientations for our models in the seismic zones (Fig. 3.10) . Firstly, the focal mechanisms investigated in this study for each of the seismic zones are not unique; there are other proposed focal mechanisms documented in the literature, but we only select focal planes for each seismic zone that are most prevalent. Moreover, at some seismic zones such as the SCSZ and the CVSZ, the seismicity is spatially diffused so that a single mechanism cannot describe the entire zone (Johnson et al. 2014, Munsey & Bollinger 1985, Madabhushi & Talwani 1993). Secondly, the presence of upper mantle heterogeneity is not the only contributing factor for stress concentration in the CEUS. Other factors such as a dense sinking body in a weak lower crust as proposed by Pollitz et al. (2001) or weak lower crust or upper mantle embedded in an elastic lithosphere by Kenner & Segall (2000) or isostatic response from deglaciation of Laurentia by Grollimund & Zoback (2001), may also play a role in affecting stresses at 10-20 km depths. Thirdly, most of the earthquakes in the CEUS occur at depths < 20 km (e.g., Bollinger & Sibol 1985, Chiu et al. 1992, Powell & Thomas 2016) on reactivated faults formed from past Wilson cycles (Thomas et al. 2006, Wolin et al. 2012). However, the mantle tomography model used in our study does not provide constraints on the geometry and strength of the shallow seismogenic faults created in the past. Lastly, our model does not account for any tectonic stresses since our focus is on the local stress perturbations from the upper mantle. In reality, the effects of plate motion, as included by Zhan et al. (2016) and Levandowski et al. (2016), will influence the near-surface stress field.

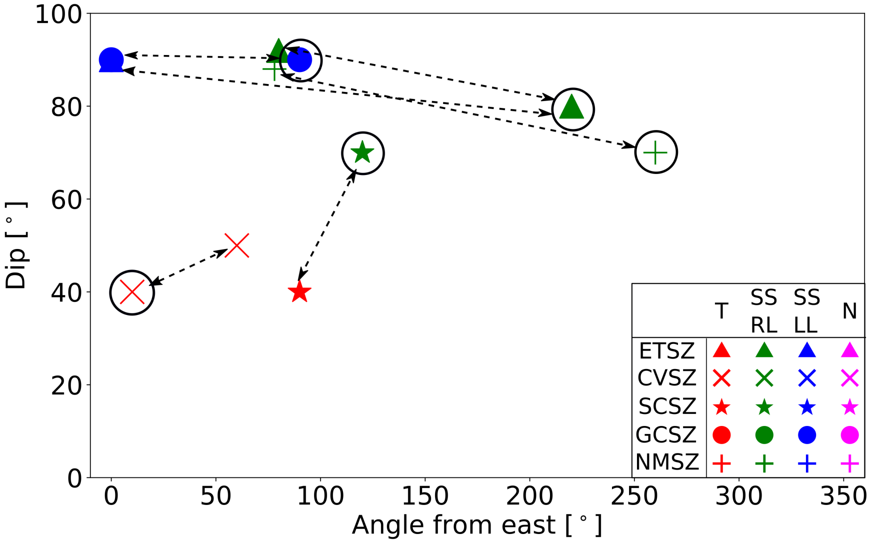

Fig. 3.10: Proposed fault planes from observational studies based on focal mechanism and earthquake hypocenters (Table 3.2) versus fault planes at which ΔC_{HT-HM} is maximum. The markers represent each of the seimic zones: New Madrid Seismic Zone (NMSZ), Eastern Tennessse Seismic Zone (ETSZ) South Carolina Seismic Zone (SCSZ), Giles County Seismic Zone (GCSZ) and Central Virginia Seismic Zone (CVSZ). The sense of fault slip is indicated with the color of the marker as thrust(T), right-lateral strike-slip (SS, RL), left-lateral strike slip (SS, LL) and normal (N). Encircled markers represent the orientations maximizing ΔC_{HT-HM}. A double-ended arrow pairs the observed and modeled fault orientations for each seismic zone.

The directions of maximum horizontal stress (S_H) computed from the model HT roughly match those obtained by Levandowski et al. (2018) in all the seismic zones but the ETSZ (Fig. 3.11). S_H based on HT is NNW-SSE in the ETSZ differing from the NE-SW direction determined using focal mechanism solutions by Levandowski et al. (2018) and by Mazzotti & Townend (2010). This is not surprising as faulting in the ETSZ may be strongly influenced by density anomalies in the lower crust inherited from past tectonic events (Levandowski et al. 2018), which are not accounted in this study.

The distribution of stress regime parameter, R, (Delvaux et al. 1997, Simpson 1997), computed based on the model HT, shows that the dominant faulting styles are thrust for the NMSZ_NE, and oblique-thrust for the GCSZ (Fig. 3.11). These stress regimes are consistent with the proposed faulting styles in Levandowski et al. (2018) for these zones, but differ from the selected studies in Table 3.2 which suggest strike-slip for the GCSZ and the NMSZ_NE. The HT model predicts normal faulting at the SCSZ and the CVSZ. These zones are associated with thrust faulting in Levandowski et al. (2018), and the studies mentioned in Table 3.2. This discrepancy between the modeled and predicted faulting style at the CVSZ and the SCSZ occurs because our model does not account for compressive tectonic stresses due to ridge push, which are highest at these zones. Within the ETSZ, a strike-slip mechanism has been suggested by other studies (Table 2 Mazzotti & Townend 2010, Powell & Thomas 2016) which agrees with our model result, but differs with Levandowski et al. (2018) who find normal faulting in the ETSZ. This discrepancy may be because Levandowski et al. (2018) consider new focal mechanism data in their stress inversions indicating a propensity for normal faulting in the ETSZ (also found in Cooley 2015).

The stresses in our model arise from instantaneous flow due to the upper mantle heterogeneity. Fig. 3.12 shows the velocity field at slice AA′ (marked in Fig 3.4) in the model HT due to heterogeneous density computed from temperatures based on the tomography study by Biryol et al. (2016). A broad downward flow is found below both the NMSZ and ETSZ in the velocity field (Fig. 3.12) on the cross-section AA′ of the model HT (marked in Fig 3.4). The descending flow induces upwellings along the edges of the model domain. The upwellings are observed at the surface as features F_1 and F_2 marked in Fig. 3.7. The broadly downward flow due to the lithospheric drip is not consistent with the asthenospheric upwelling that Biryol et al. (2016) proposed would occur as a counter-flow to the drip. However, the asthenopsheric upwelling cannot be reliably rejected because the velocity field in our model depends on various parameters including the viscosity of the asthenosphere and the boundary conditions. Lower viscosity of the asthenosphere, for instance, would reduce the lateral extent of the downward drag by the lithospheric drip

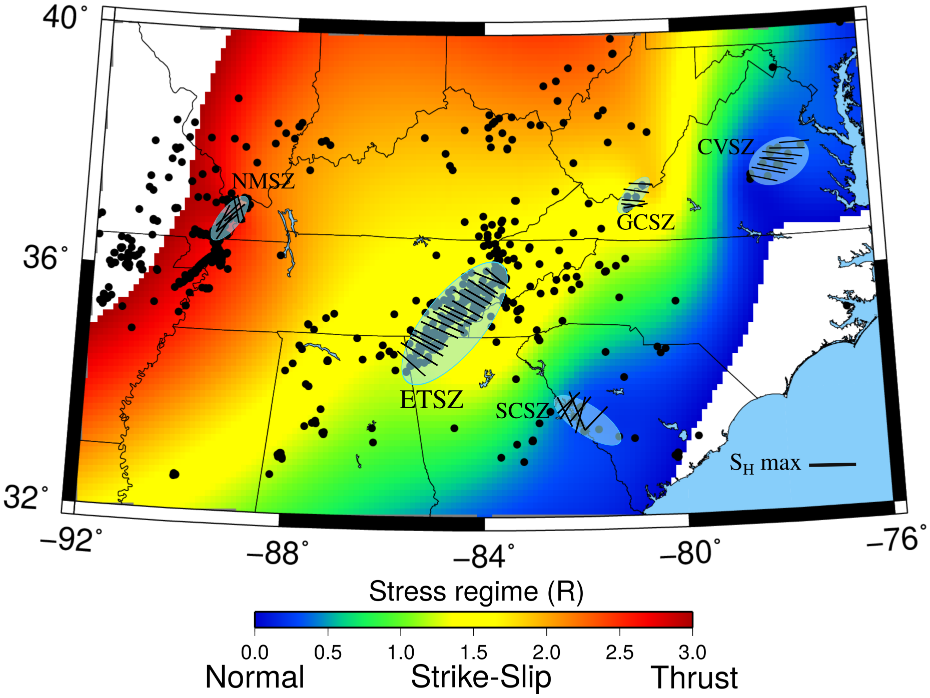

Fig. 3.11: Maximum horizontal stress directions (S_H) at all the seismic zones for the heterogeneous (HT) model (black lines) overlain over the stress regime (R) computed using the principal stresses at these seismic zones.

such that the region beneath the NMSZ might not be affected as strongly as in the current model.

We calculated residual topography in our study region following the approach by Becker et al. (2014) for the isostatic and dynamic topography for the western US. We first calculate the isostatic topography. We use CRUST1.0 (Laske et al. 2013) for crustal thickness and density (Fig. 3.13a) and LITHO1.0 (Pasyanos et al. 2014) for lithospheric thickness variations (Fig. 3.13b). We assume a constant lithospheric density of 3300 kg/m^3 and a constant asthenosphere density of 3250 kg/m^3. These values are reasonable for a density contrast between the lithosphere and asthenosphere (e.g., Bonnardot et al. 2008, Ito & Simons 2011). Although the crustal contribution to the topography is about 10 times more dominant than the lithosphere for these density values, the residual topography highs are preferentially associated with the very thinned lithospheric locations (Fig. 3.13c), which have greater influence than the crustal thickness variations. We also plot the

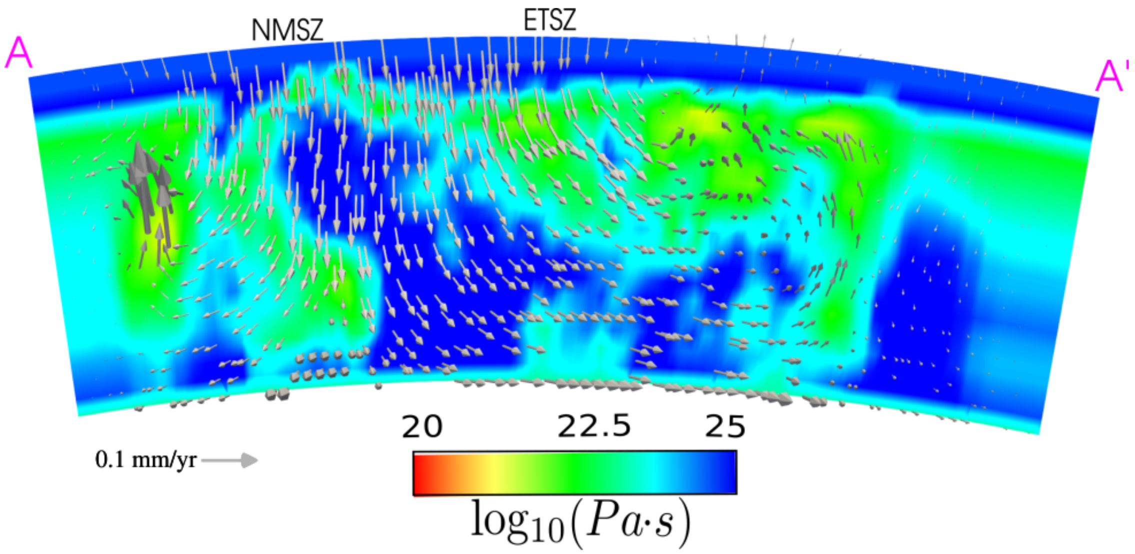

Fig. 3.12: Velocity (arrows) and viscosity fields from the model HT on the slice AA′ (marked in Fig 3.4). The extreme high-velocity vectors observed west of the NMSZ and out of the plane are from the upward return flow due to the downward pull of the lithospheric drip and are likely an artifact due to fixed boundary conditions at the sides.

residual topography due to the density distribution based on the Biryol et al. (2016) tomography in Fig. 3.13d.

Some similarities are found between the residual topography based on the globally compiled data set (Fig. 3.13c) and the one based on the densities calculated from Biryol et al. (2016)'s tomography (Fig. 3.13d) but these two topography models exhibit inconsistencies as well. The high-density lithospheric drip clearly generates a topographic low (outlined by dashed line in Fig. 3.13d). The topographic low is the effect of the density and thickness along depth at each lateral point in the model and, therefore differs from the boundary marked in the Fig. 3.3. Regions marked by encircled letters, A, B, and C on Fig. 3.13d show positive dynamic topography coinciding spatially with the positive residual topography in Fig. 3.13c although less in extent and magnitudes. The mismatch between the residual and the dynamic topography can be attributed to several factors. Firstly, the seismic tomography puts no constraints on the crustal structure, and the crust is assumed to have a uniform thickness of 40 km to calculate the isostatic response, contrary to the crustal thickness and density variations obtained from the CRUST1.0 model. Secondly, the

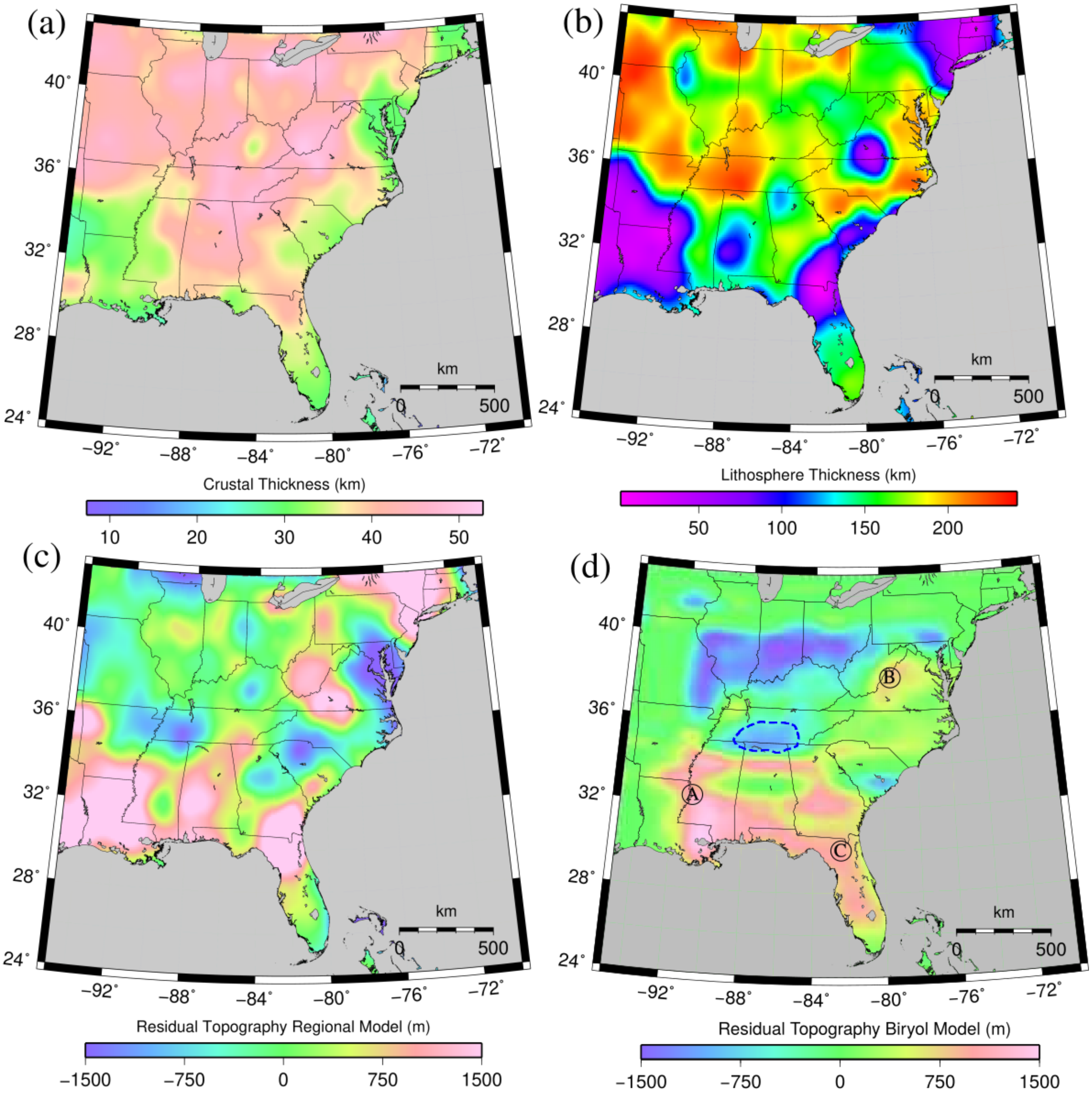

Fig. 3.13: Residual topography calculated from densities based on the regional tomography by Biryol et al. (2016) used in this study and from global models. (a) Crustal thickness from CRUST1.0 (Laske et al. 2013). (b) Lithospheric thickness from LITHO1.0 (Pasyanos et al. 2014) (c) Residual topography calculated using (a) and (b). (d) Residual topography based on the densities calculated using the regional tomography. Encircled letters, A, B, and C, mark the regions where residual topography are strongly positive in both models. The dashed blue line delineates the topographic low due to the lithospheric drip.

LITHO1.0 model is about eight times coarser in resolution than the tomography study, and we assumed a constant density of 3300 kg/m^3 in the lithosphere instead of the density based on the heterogeneous temperature. We suggest that continued investigation into accurate crustal and lithospheric thickness, and density variations is required to observe any dynamic topography response from the upper mantle flow beneath this region. Time dependent modeling will be needed to address the mechanism for the origin of a foundering drip in the CEUS. Such an investigation in this region would call for more sophisticated techniques such as backward advection modeling (e.g., Conrad & Gurnis 2003), quasi-reversibility (Glišović & Forte 2016), or adjoint methods (e.g., Bunge et al. 2003, Liu et al. 2008) for the calculation of initial conditions on temperature, viscosity and density, which has not been done in this study. It has been proposed by Biryol et al. (2016) that the lithospheric foundering could have started due to Rayleigh-Taylor instability beginning from the presence of an ecologized root as proposed by Le Pourhiet et al. (2006) in the western US. It is also possible that the dense high velocity mantle feature is part of the subducted Farallon slab below this region (Schmandt & Lin 2014). We do not comment on the origin of this high-velocity feature but follow the naming convention by Biryol et al. (2016) as a drip in this study. Additional observations such as low dynamic topography at the surface would be required to confirm if the high velocity is indeed attached to the lithosphere or is a remnant Farallon slab.

In summary, the numerical model with heterogeneous temperature, density, and viscosity based on the tomography study by Biryol et al. (2016), indicates differential stress concentration due to the upper mantle heterogeneity at the major seismic zones in the CEUS: ETSZ, NMSZ, GCSZ, CVSZ, and parts of the SCSZ. We also examine the isolated effect of a positive P-wave velocity anomaly interpreted by Biryol et al. (2016) as a lithospheric drip and observe increased differential stress in the seismic zones surrounding the root (ETSZ and NMSZ). Coulomb stress was also increased in all the seismic zones at their optimal fault orientations obtained from other studies when all the upper mantle heterogeneity is considered. Therefore, our results provide a possible mechanism for reactivation of the faults in the intraplate seismicity of the CEUS. This, in turn, helps to better associate seismic hazard with the seismic zones in the CEUS. Therefore it can be inferred that the presence of mantle heterogeneity is a factor in generation of the earthquakes but not the sole factor, and the mantle heterogeneity should be accounted for in any comprehensive model of earthquake generation.

Appendix B

The effects of composition at high temperature and pressure are incorporated in seismic velocity following Cammarano et al. (2003) in which the elastic moduli (K, G) and densities (ρ) at reference temperature T_0 and pressure P_0 are first extrapolated at high temperatures (T) and then adiabatically at high pressures (P) following finite-strain extrapolation (Duffy & Anderson 1989). The calculations are divided at pressures 12.5 GPa to account for phase transformation of olivine to β spinel at 410 km.

To calculate density at high pressures, a mantle adiabat with potential temperature (T_{pot}) $1300^o C$ was chosen for depths $\leq$ 410 km and $1600^o C$ for deeper depths up to 660 km. Strain (ϵ) is first calculated at known pressures (based on PREM model by Dziewonski & Anderson (1981)) using K_0, G_0 and their pressure derivatives, K_S', G' (Table 3.3). Reference density calculated at the potential temperature and zero pressure ($\rho(T_{pot}, P_0)$) is then used to get the density $\rho(P, T)$.

$$P = -(1-2\epsilon)^{5/2}\left[3K_0\,\epsilon + \frac{1}{2}\left(9K_0(4-K_S')\right)\epsilon^2\right],$$

$$\epsilon = \frac{1}{2}\left[1-\left(\frac{\rho(T,P)}{\rho(T_{pot},P_0)}\right)^{2/3}\right]$$

$$\rho(T_{pot},P_0) = \rho(T_0,P_0)\ \exp\left(-\int_{T_0}^{T_{pot}}\alpha(T)dT\right)$$

where thermal expansivity, $\alpha(T) = \alpha_0 + \alpha_1 T$ is truncated after the second term. Density changes due to temperature, T from the reference geotherm, T_o and pressure are calculated from above as:

$$\delta\rho = \rho(T_0,P_0)\exp\left(-\int_{T_0}^{T}\alpha(T')dT'\right)\alpha(T))(T-T_o) \tag{3.4}$$

Table 3.3: Mineral physics data used in this study

Mineral	Density (kg/m^3)	K_S (GPa)	μ (GPa)	K'	μ'	$\partial K/\partial T$ (GPa/K)	$\partial \mu/\partial T$ (GPa/K)	$a_0(10^{-4})$	$a_1(10^{-7})$
olivine	3222	129	81	4.2	1.4	-0.017	-0.014	0.20	0.139
orthopyroxene	3215	109	75	7	1.6	-0.027	-0.012	0.387	0.044
garnet	3565	171	92	4.4	1.4	-0.019	-0.01	0.099	0.116
wadsleyite	3472	172	121	4.5	1.5	-0.014	-0.014	0.232	0.0904
majorite	3565	171	92	4.4	1.4	-0.019	-0.01	0.0991	0.1165

K_S: adiabatic bulk modulus, μ: shear modulus, K': pressure derivative of bulk modulus, μ': pressure derivative of shear modulus, $\partial K/\partial T$: bulk modulus derivative with temperature, $\partial \mu/\partial T$: shear modulus derivative with temperature, a_0, a_1 are constants in thermal expansivity, $\alpha = a_0 + a_1 T$. Values of elastic moduli and their derivatives are from Cammarano et al. (2003) and thermal expansivity are from Saxena & Shen (1992).

Temperature dependence on K G, is assumed linear while changes in K_S', G' is calculated from the procedure in (Duffy & Anderson 1989) as:

$$\begin{aligned}\delta M|_{T,P0} &= \frac{\partial M}{\partial T}(T - T_o)\\ \delta M'|_{T,P_0} &= \left(M'(T_0)\text{exp}\left[\int_{T_0}^{T} \alpha(T)dT\right]\alpha(T)\right)(T - T_o),\end{aligned}$$

where M is either K or G, δM, $\delta M'$ are changes in elastic modulus and its pressure derviate due to temperature T.

Elastic moduli changes are then evaluated at high pressures using second-order extrapolation order expansion (Duffy & Anderson 1989):

$$\delta K + \frac{4}{3}\delta G = (1-2\epsilon)^{5/2}\left[M_1 + \epsilon\left(5L_1 - 3\frac{\partial K}{\partial T}(T - T_o)\left[K' + \frac{4}{3}G'\right] - 3K_0 M_2\right)\right], \quad (3.5)$$

$$\text{where,} \quad M_1 = \delta K|_{T,P0} + \frac{4}{3}\delta G|_{T,P0}; \quad M_2 = \delta K'|_{T,P_0} + \frac{4}{3}\delta G'|_{T,P_0}$$

The anharmonic velocity variations due to temperature and pressure are then calculated using 3.4, 3.5 for each mineral and then averaged using Voigt (constant strain) averaging scheme for the reference composition, discontinuous across 410 km, described in section .

$$\delta V|_{anh} = \frac{1}{2\sqrt{K_0 + 4/3G_0}\sqrt{\rho_0}}\left[\delta K + \frac{4}{3}\delta G\right] - \frac{K_0 + 4/3G_0}{1\rho_0^{3/2}}(\delta\rho) \tag{3.6}$$

Frequency dependence (anelasticity) of velocity with temperature is incorporated following Goes et al. (2000):

$$\begin{aligned} \delta V|_{anel} &= Q_p^{-1}\frac{aH}{2RT^2\tan(\pi a/2)}, \\ Q_p^{-1} &= A\omega^a \exp\left[\frac{a(H+PV)}{RT}\right]\frac{3Vp_0^2}{4Vs_0^2} \end{aligned} \tag{3.7}$$

Here, $\omega = 2\pi$, values of laboratory constants, $a = 0.15, A = 0.148$, activation energy $H = 500$ kJ/mol, volume $V = 20$ cm^3/mol are taken from Sobolev et al. (1996). Vs_0 and Vp_0 are S and P wave velocities from IASP91 (Kennett & Engdahl 1991).

The reference geotherm (T_0) for lithospheric (i.e., < 200 km) depths is the one used in (Goes & van der Lee 2002) for eastern US and for greater depths, we follow Fig. 4.56 from Turcotte & Schubert (2014) due to lack of evidence for regional geotherms at deeper depths. Thermal expansivity (α) from Saxena & Shen (1992) (see Table 3.3). We assume a reference composition of harzburgite, i.e., 83 % olivine (ol), 15 % orthopyroxene (opx), 2 % garnet (gt) (McDonough & Rudnick 1998) for depths 40 km to 410 km or pressure (P) < 12.5 GPa. For depths from 410 km to 660 km, we use a reference composition of 60 % Mg-wadsleyite and 40 % Majorite (Haggerty 1995). We use Burnman, a mineral physics toolbox (Cottaar et al. 2014), to calculate the mantle adiabat with a potential temperature of 1300°C for P < 12.5 GPa, which is appropriate for continental lithosphere (Rudnick et al. 1998) and 1600° for P > 12.5 GPa (Katsura et al. 2010). Values for bulk modulus (K_S), shear modulus (G) and density (ρ) for each mineral in the composite are taken from Cammarano et al. (2003) and are listed in Table 3.3.

We account for the anelastic effects on the seismic velocity by correcting for the power law dependence of frequency on seismic attenuation, Q_p. We use linear pressure dependence on activation enthalpy ($H(P) = H_0 + VP$, V is the activation volume) in calculating Q_p, (model 2 described inSobolev et al. (1996)). Another way to correct for pressure dependence on enthalpy is using melting temperature dependence, (model 1 in Sobolev et al. (1996), i.e., $H(P) = gRT_m$ where g is constant and T_m is melting temperature). We use model 2 because we do not include the effects of melting in the seismic anomalies for the reasons discussed earlier. We use a value of 1 Hz for the frequency in the attenuation calculation.

The inversion procedure starts with an initial guess for temperature and updates the temperature values at all the observational points in the tomography until the difference of the calculated anomalies with the observed seismic anomalies is minimized. We also calculate temperatures accounting for uncertainties in the elastic moduli and their temperature derivatives as in (Cammarano et al. 2003)) and compare them with the results obtained here using the mean values given in Table 3.3. Taking the maximum values of the elastic parameters reduces the temperature sensitivity such that the negative (positive) velocity anomaly decreases (increases) temperature by a small ($\pm$ 90 K) magnitude. On the other hand, minimum parameter values increase the temperature sensitivity, and therefore the range of temperatures obtained, by $\sim$ 180 K.

Our approach has several differences from that of Cammarano et al. (2003). Firstly, we invert velocity anomalies, not absolute velocities, for temperature anomalies, which are added to an assumed reference geotherm T_o. Secondly, we use the Voigt averaging scheme to calculate elastic moduli and density of the composite rock instead of the Hashin Shtrikman scheme used by Cammarano et al. (2003). Although the Voigt scheme is known to overestimate the converted values (Watt et al. 1976), seismic velocities based on compositions averaged by the Voigt scheme, which is representative of the upper bound value for the composite (Watt et al. 1976), and the Reuss scheme, which is representative of the lower bound value for the composite (Watt et al. 1976), shows less than 0.2 %

difference in magnitudes. Since this error is within the range of the tomography error (Biryol et al. 2016), we use the computationally simpler Voigt scheme. Finally, elastic moduli at high pressures are extrapolated using second-order accuracy instead of third-order for simplicity in implementation of the inversion.

Supplementary figure

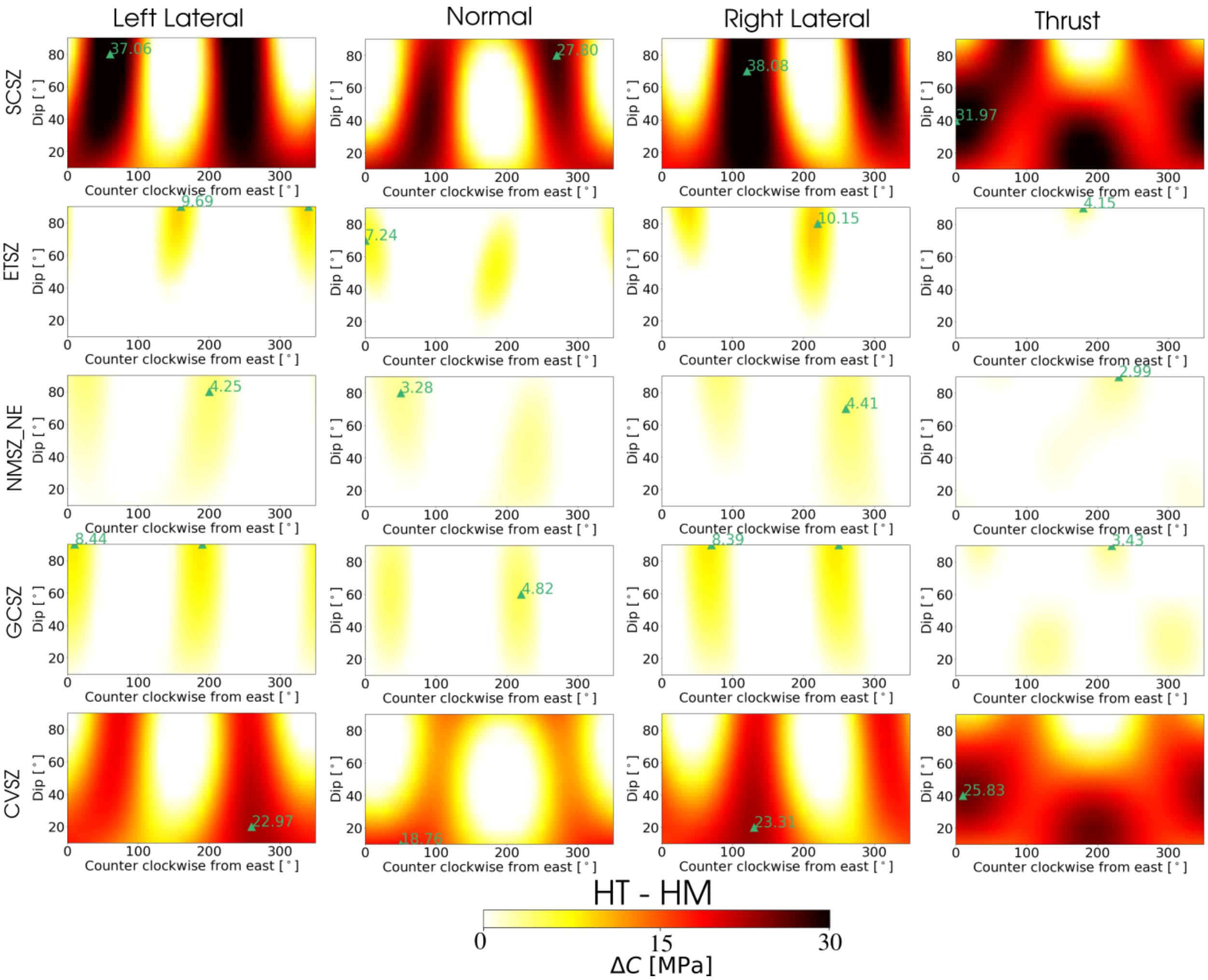

Fig. S1: Coulomb stress change, ΔC, for HT−HM in the seismic zones for possible strikes, dips, and slip directions: right-lateral, left-lateral strike-slip, normal, and thrust faulting. Subplots are also labeled with maximum ΔC, and a triangular marker denoting the orientation and dip where the maximum occurs.

Chapter 4

Detecting lithospheric discontinuities beneath the Mississippi Embayment using S wave receiver functions

This chapter is ready for submission to Journal of Geophysical Research, Solid Earth for publication as Saxena, A., and Langston, C. Detecting lithospheric discontinuities beneath the Mississippi Embayment using S wave receiver functions

Abstract

Identifying upper-mantle discontinuities in the Central and Eastern US is crucial for verifying models of lithospheric thinning, and a low-velocity anomaly structure beneath the Mississippi Embayment. In this study, S-wave receiver functions (SRFs) were used to detect lithospheric boundaries in the embayment region. The viability of SRFs in detecting seismic boundaries was tested before computing them using the earthquake data. A careful analysis using a stochastic noise and coda model on the synthetics revealed that a negative velocity gradient could be detected with certainty at low to moderate noise levels after using two different stacking techniques. A total of 31518 SRFs from 688 earthquakes recorded at 174 seismic stations including the Northern Embayment Lithospheric Experiment, EarthScope Transportable Array and other permanent networks were used in this study. Common depth point stacks of the SRFs in $1^\circ \times 1^\circ$ bins indicated a continuous and broad Sp phase corresponding to a negative velocity gradient at depths between 60 and 100 km. The maximum amplitudes of the phase trend East of the Reelfoot Rift, suggesting a concurrent origin of the discontinuity with the formation of the rift. The observed negative Sp phase is interpreted as a mid-lithospheric discontinuity, and several possible mechanisms for this discontinuity are explored. After quantitative analysis, a combination of temperature, composition, and water content variations are attributed to explain the observed negative Sp in this study. The observations and interpretations in this study support the previous claims of a mid-lithospheric discontinuity in the Central and Eastern US and provides a possible mechanism for its origin.

Introduction

The objective of this study is to constrain lithospheric structure using S-to-P conversions beneath a large portion of the Central and Eastern US (CEUS) that includes the northern Mississippi Embayment, a prominent sedimentary basin (marked in Fig. 4.1).The lithosphere provides us indirect information on the underlying asthenospheric flow. Imaging lithospheric thickness and its structure is, therefore, vital to understanding the coupling mechanism between asthenospheric flow and surface plate motions (Stoddard & Abbott 1996). A technique that offers insight into the lithosphere and its thickness is receiver function analysis, i.e., isolating conversions from the near-receiver earth structure response using teleseismic P and S waves radiated from large earthquakes and explosions (Langston 1979, Vinnik 1977).While both P-to-S and S-to-P conversions have been extensively used for detecting upper mantle seismic discontinuities (Farra & Vinnik 2000, Gilbert et al. 2003, Xu et al. 2007, Spieker et al. 2018), S-to-P phases have an advantage over P-to-S for lithospheric study since they are free from the P multiples between the surface and the Moho (Yuan et al. 2006).

A number of previous studies have reported on lithosphere beneath the contiguous US using S wave receiver functions (e.g., Abt et al. 2010, Hopper et al. 2014, Lekić & Fischer 2014, Hansen et al. 2015, Hopper & Fischer 2015, Liu & Gao 2018). These studies have successfully shown a sharp negative velocity gradient at depths coinciding with the lithosphere-asthenosphere boundary in the western US ($\sim$ 50 to 120 km), but the detection of lithospheric thickness beneath the CEUS remains problematical. Instead, previous work has pointed to another shallower, and discontinuous velocity contrast interpreted as the mid-lithospheric discontinuity in the CEUS. This difficulty in detecting the lithosphere-asthenosphere boundary below the CEUS probably arises from its gradual velocity decrease due to lesser temperature changes and magmatism in the asthenosphere compared to the western US (e.g., Rychert & Shearer 2009, Eaton et al. 2009). It has been particularly challenging to detect the lithosphere below the unconsolidated sediments of the

Mississippi Embayment since the Sp phase may be masked with near-surface reverberations.

We have several motives for our study, which builds upon previous work. Sp conversions within S wave receiver functions are often difficult to detect for small velocity impedance contrast due to the interference from P wave coda. We investigate this problem by conducting an analysis of the effect of noise using different synthetic realizations of P and S wave coda added to synthetic S-wave receiver functions. To increase the signal-to-noise ratio of the Sp converted wave generated at a gradual velocity contrast, we test two different stacking techniques—one based on receiver functions and another on individual seismogram components—using the noise simulations. After obtaining adequate results from the synthetic tests, we extend our methodology to the real earthquake data. Our study utilizes the dense network coverage available over the CEUS (Fig. 4.1) and teleseismic earthquakes over seven years to investigate the lithospheric structure at an improved resolution. Another motivation for computing S-wave receiver functions in the CEUS is to find evidence for an anomalous low-velocity structure (low Vp, Vs of -3 to -5 % at depths 80 - 200 km), recently imaged in tomography studies by Nyamwandha et al. (2016) and Chen et al. (2016) of the CEUS.

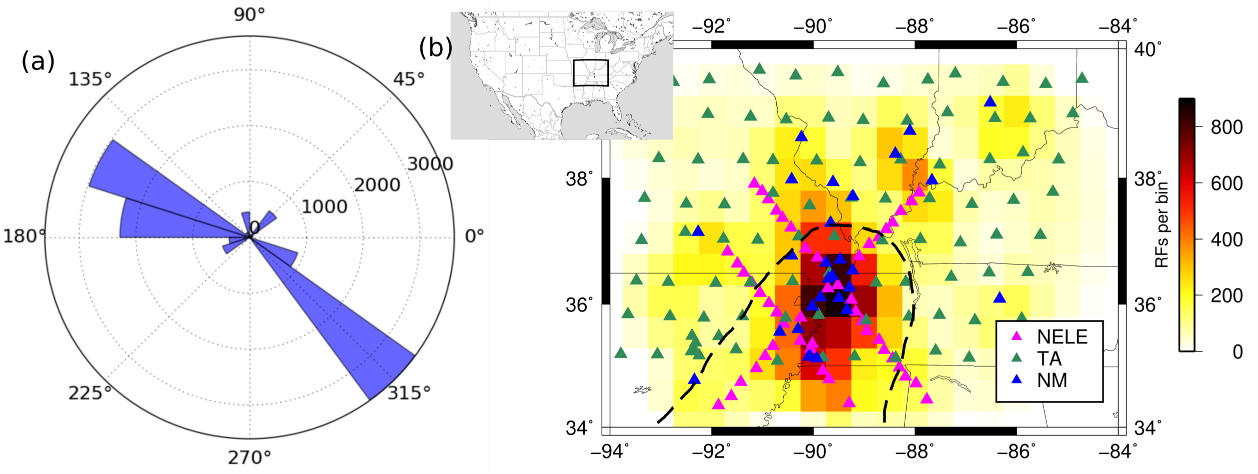

Fig. 4.1: (a) Polar plot showing the number and azimuthal directions of the earthquake hypocenters between Jan, 2010 to Dec, 2017 with respect to the receivers used in this study.(b) The study region showing all the broadband stations from various networks (filled triangles) overlying with the number of RFs in each bin of size 1° x 1° with an overlap of 0.5°. NELE: Northern Embayment Lithospheric Experiment, TA: EarthScope Transportable Array, NM: New Madrid network. Earthquake data is obtained from United States Geological Survey at `https://earthquake.usgs.gov/earthquakes/search/`. Inset shows our study region relative to the map of US.

Data

We utilize wavefom data from 688 earthquakes with Mw > 5.5 occurring between Jan 2010 and Dec 2017. Location parameters are taken from the United States Geological Survey earthquake catalog (`https://earthquake.usgs.gov/earthquakes/search/`) and waveforms recorded at stations from EarthScope Transportable Array network, New Madrid stations handled by Center for Earthquake Research and Information (CERI), and Northern Embayment Lithospheric Experiment (NELE) stations under the EarthScope FlexArray deployment in the area shown in Fig. 4.1. A total of 31518 3-component seismograms were obtained from Incorporated Research Institutions for Seismology (IRIS) Data Management Center for epicentral distance between 55° and 85°. This range of the epicentral distance avoids interference from deeper phases such as SKS and post-critical Sp reflections at lithospheric depths (Wilson et al. 2006).

We preprocess the downloaded raw data following the usual steps of removing the mean, synchronizing the seismograms to an origin time of 0 sec, time windowing one minute before and after the estimated S wave arrival based on the iasp91 model (Kennett & Engdahl 1991),removing instrument response with band-passed frequency limits 0.03 to 5 Hz and rotating the horizontal components to the radial and transverse components. This ensures that the radial, transverse and the vertical seismogram components have the majority of SV, SH, and P energy, respectively, in the teleseisms (Aki & Richards 1980).The resultant seismogram components are band passed using Butterworth filter with four poles at corner frequencies 0.03 and 0.5 (Abt et al. 2010).

Methodology

The main principle behind P (or S) wave receiver functions is to deconvolve the vertical (or radial) component from the radial (or vertical) component. This process removes the shared source and propagation effects, resulting in a time series of converted or reflected P-to-S (or S- to-P) waves at structural boundaries below the receiver (e.g. Langston 1977). For our problem of defining the lithospheric strucuture, we compute S-wave receiver functions (SRFs).

We compute the SRFs from the pre-processed data by deconvolving the radial from the vertical component using spectral division based on the water-level technique (Clayton & Wiggins 1976). The water-level is chosen after some trial and error as 0.005 times the maximum amplitude of the power spectrum of the radial component. We use a Gaussian filter of width 0.25 Hz to remove the high frequencies in the receiver functions (Langston 1979).We select only the SRFs which have a short-term over long-term (sta-lta) average higher than 2.5 and then normalize those with respect to their peak amplitude. The process of sta-lta averaging reduces the number of waveforms by a factor of three such that subsequent calculations are done on only 10502 SRFs. We then calculate the piercing points for all sources and epicentral distances at the receivers using the IASP91 velocity model (Kennett & Engdahl 1991). To migrate the RFs to depth, we first calculate travel times for piercing depths between 10 to 300 km at an interval of 1 km (Liu & Gao 2018) using the velocity model based on CRUST1.0 (Laske et al. 2013) model for depths < 40 km and IASP91 (Kennett & Engdahl 1991) for depths below (plotted in Fig. 4.2). We then interpolate the amplitudes of RFs using this piercing time with depth variation, which removes the effect of the ray parameter. We then stack the SRFs based on the common depth points, as used by other studies (e.g., Dueker & Sheehan 1998, Steckler et al. 2008), within bins of size 1° and 0.5° overlap.

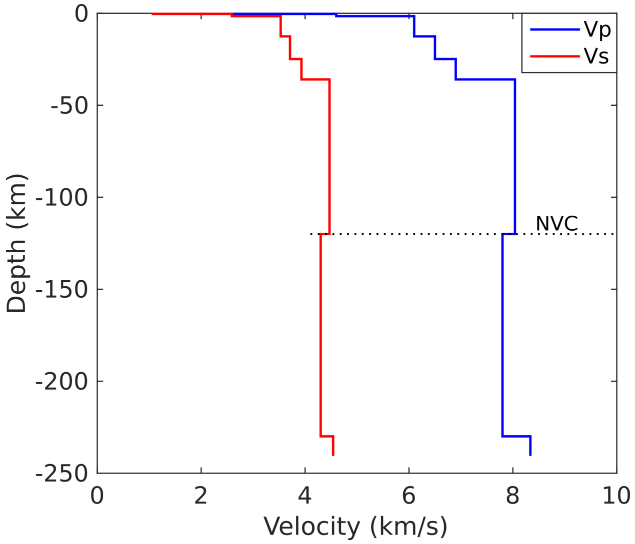

Fig. 4.2: Velocity model used for computing the synthetic seismograms, based on the CRUST1.0 (Laske et al. 2013) and IASP91 (Kennett & Engdahl 1991) Earth models with an added negative velocity contrast (NVC) at depth 120 km.

We also follow the component stacking procedure as used by Abt et al. (2010) and compare the results with stacking the RFs as described above. In this technique, we remove the move-out by applying time shifts to all seismograms so that they align with a reference seismogram (having epicentral distance 70.77° and velocity model shown in Fig. 4.2) for a range of possible discontinuities ranging from 10 to 300 km depth. We then stack the seismograms within each bin for all the possible depths and calculate RFs by deconvolving the stacked radial from the vertical component. We then interpolate the RFs to depth using the time-depth variation for the reference receiver function. We find that receiver function stacking performs better; therefore, we show the results from the component stacking only in the supplementary information (Fig. S1).

Our methodology is first tested using synthetic seismograms before using the earthquake data. We compute the synthetics using a plane-layered velocity model (Fig. 4.2) with a propagator matrix method (Haskell 1962). The velocity model assumed is from CRUST1.0 for depths <40 km and the iasp91 Earth model for depths below (Fig. 4.2). We add a velocity contrast of -3% at the depth of 120 km ($\sim$ -5%) feature below the Mississippi Embayment, as imaged by Nyamwandha et al. (2016), where we expect to detect a reasonable amplitude S-to-P converted phase. We use a simple Gaussian source time function for the incident SV wave. Different ray parameters between 0.07 to 0.1 sec/km were used to account for different receiver locations while stacking.

We add noise in our synthetics following the approach by Langston & Hammer (2001).Langston & Hammer (2001) present the effects of P-wave coda on P-wave teleseismic receiver functions. They approximate the coda as an exponentially decaying waveform with time and add the coda to all seismogram components. We extend their method in this study by employing both P and S wave coda decay in the noise model to mimic the behavior of earthquake data. Fig. 4.3 shows one realization of the noise model along with earthquake data recorded at one of the stations, HICK, in the Mississippi Embayment.

The noise is added in both vertical and radial components as:

$$N_V(t) = C_V e^{-\gamma(t-tp)} n_1^V(t) H(t-tp) + C_R e^{-\gamma(t-ts)} n_2^V(t) H(t-ts) + N_m^V \tag{4.1}$$

$$N_R(t) = C_V e^{-\gamma(t-tp)} n_1^R(t) H(t-tp) + C_R e^{-\gamma(t-ts)} n_2^R(t) H(t-ts) + N_m^R \tag{4.2}$$

where, $N_V(t)$ and $N_R(t)$ are noise added to the vertical and radial components, respectively. The first and second terms in the right-hand side of Eq. 4.1 and Eq. 4.2 represents the P and S wave coda controlled by the decay parameter, $\gamma = 0.02$ s^{-1} (Langston & Hammer 2001). C_V and C_R are constants equal to the fraction of the maximum amplitude of vertical and radial components, respectively, and varied between

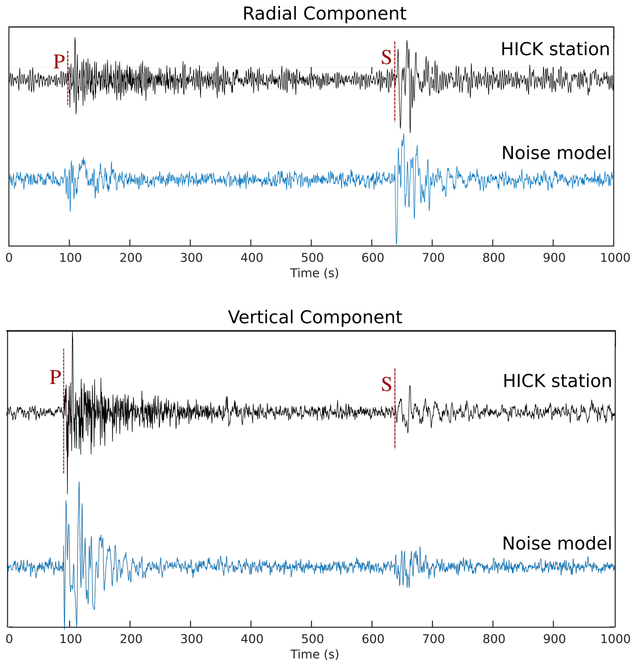

Fig. 4.3: Radial and vertical components from one earthquake recorded at HICK station in the Mississippi Embayment in black and the corresponding waveform data generated using the noise model utilized in our study.

0.5 to 1.5. $H(t)$ is the heavy-side function determined by the arrival times of the P wave, tp and S wave, ts. $n_{1,2}^{V,R}(t)$ are different realizations of the white noise convolved with the source function. $N_m^{V,R}$ is background white noise equal to 0.01 times the maximum amplitude of the respective component.

Fig. 4.4 shows the vertical and radial seismograms along with the added noise model based on Eq. 4.1 and Eq. 4.2. We also calculate the receiver functions computed from these seismograms. It can be seen from Fig. 4.4 that the converted Sp phase at the top of the low velocity zone, S$_N$P, picked in the noise-free S-wave receiver function, is indistinguishable in the presence of various noise models. Therefore, we attempt to retrieve the phase using two different stacking methods.

To achieve a good S/N ratio in the receiver functions with added coda noise, we obtain stacked receiver functions by stacking in both individual seismogram components (Eq. 4.3) and the receiver functions (Eq. 4.4), for different noise levels controlled by the values C_V and C_R (Fig. 4.4). The resultant seismogram components with varying ray

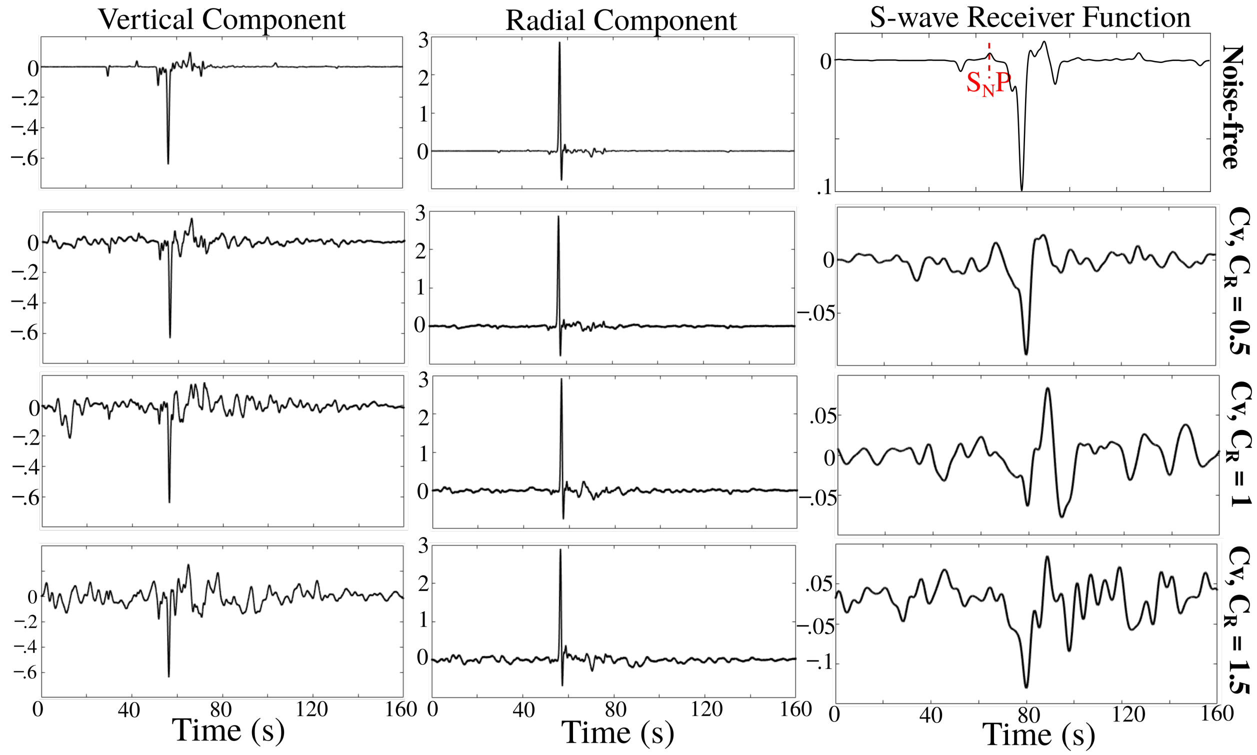

Fig. 4.4: Noise-free and noisy synthetic seismograms computed following the approach by Langston & Hammer (2001). Each row represents the different noise levels, i.e., 0, 0.5, 1, 1.5, in the vertical component, the radial component, and the S-wave receiver function. The converted S_NP phase at the top of low-velocity zone (marked in Fig. 4.2) is shown in the top right receiver function.

parameters, p, are shifted by time lags at which the cross-correlation with a reference radial component is maximum. The value of p changes within 0.01 s/km such that move-out corrections of the Sp converted phase at the negative velocity contrast (NVC) fall within 0.5 °, and can be ignored. We account for the randomness in the noise by using 1000 realizations of added noise in both vertical and radial components for a given value of p. The Bootstrap technique (Efron & Tibshirani 1986) is then employed for stacks containing 20 to 100 waveforms, and the misfit of the noisy Sp phase at the NVG is calculated from the noise-free phase in the stacked receiver functions (Fig. 4.5) following eq. 4.5.

$$RF(t) = F^{-1}\left(\frac{\sum_{n=1}^{s} G(\omega)V_i(\omega)}{\sum_{n=1}^{s} R_i(\omega)}\right) \tag{4.3}$$

$$RF(t) = \sum_{i=1}^{s} \left(F^{-1} \frac{G(\omega) V_i(\omega)}{R_i(\omega)} \right) \tag{4.4}$$

$$\epsilon = \sum_{i=t_0}^{t_1} |Sp_i - Sp_i^n|, \tag{4.5}$$

where, $R_i(\omega)$ and $V_i(\omega)$ are the frequency spectrum of the radial and vertical components, $G(\omega)$ is the Gaussian function of width 0.25 Hz and s is the number of samples used in stacking. Sp_i and Sp_i^n represents the noise-free and noisy Sp phase converted at the NVC beginning at time t_0 and ending at t_1.

Fig. 4.5 shows that, overall, stacking the individual noisy components first before deconvolution recovers the Sp phase converted at the NVC ($S_N p$) better than stacking the noisy receiver functions. It is important to note that the RF waveform stacks shown in Fig. 4.5 (left) are for 100 samples at one iteration of bootstrapping. It is a possibility that the results are different for different bootstrap iterations. Therefore,the mean misfit trend gives a better estimate for recovering the $S_N p$ after stacking. The decreasing trend of a misfit with the number of samples used in stacking is expected as the coda noise is calculated using white noise, which sums to zero when a large number (tending to infinity) of samples is used. RFs from both stacking techniques recovers S$_N$p at low noise levels, i.e., C_V, C_R = 0.5 for higher bootstrap samples (> 40). At high noise levels of C_V, $C_R = 1$, $S_N p$ can possibly be observed with $\sim$ 100 samples in the stack, but further increasing the noise level to 1.5 does not recover the S$_N$p for both stacking methods. We use both stacking methods on the earthquake data in the Mississippi Embayment. We get a good S/N ratio when we stack the receiver functions. We show the results using this stacking technique here. The results from stacking the individual seismogram components first and then calculating the receiver functions, are shown in the supplementary material.

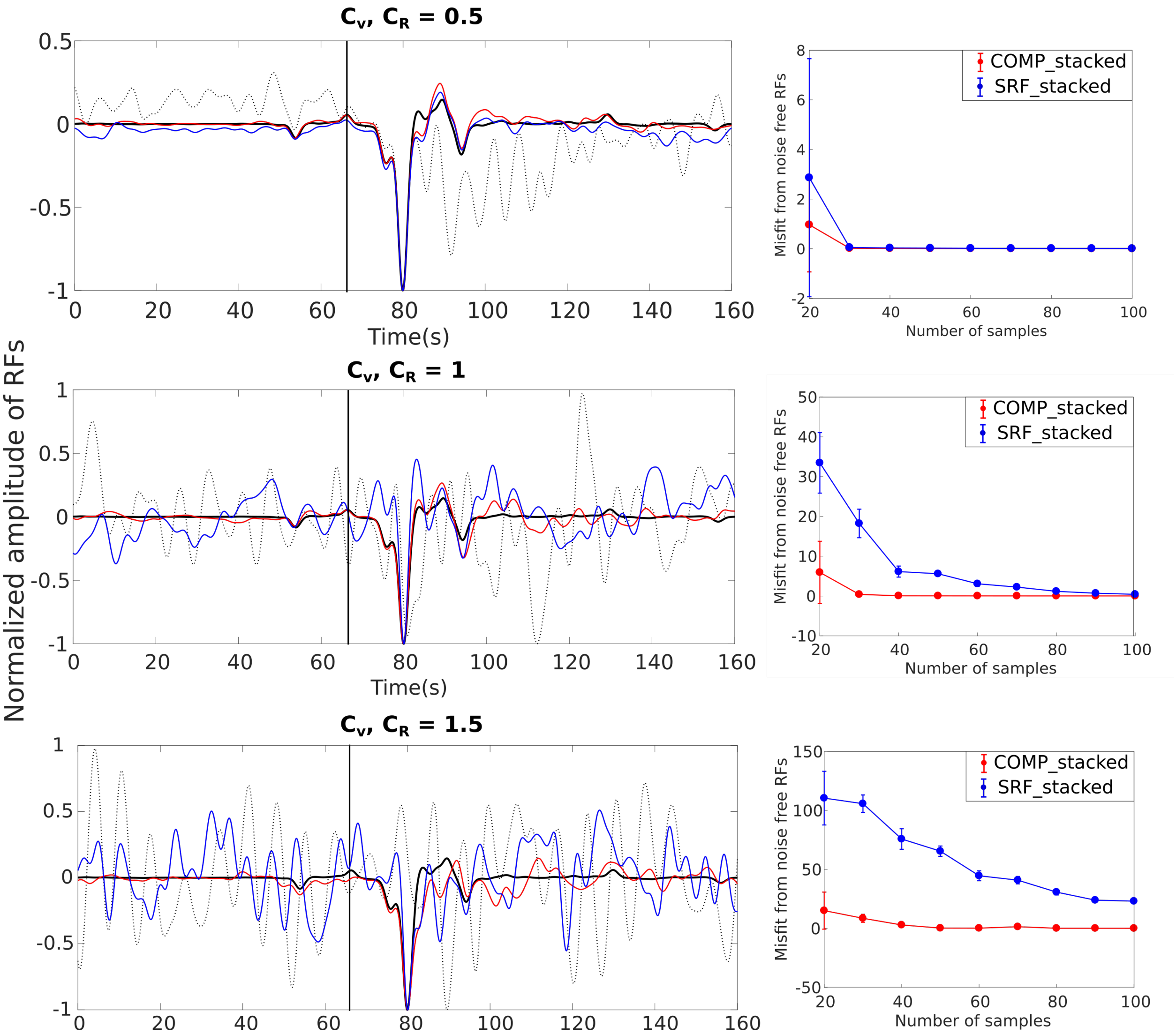

Fig. 4.5: Normalized S-wave receiver function (SRF) with and without added coda noise after stacking and the corresponding misfit of the Sp phase converted at the top of negative velocity zone (S_Np) between noisy and noise-free seismograms. (Left) Black solid and dotted waveforms are the calculated RFs from noise-free and noisy seismogram components, respectively. The SRF functions calculated after stacking 100 bootstrapped noisy seismograms (COMP_stacked) and receiver functions (SRF_stacked) are shown in blue and red, respectively, at different coda noise levels governed by constants, C_V, C_R. The vertical line marks the maximum amplitude of S_Np. (Right) Mean misfit between the noisy and the noise-free S_Np along with one standard deviation after 500 bootstrap iterations plotted with the number of samples used in component and RF stacking.

Receiver Functions and Interpretation

We follow the methodology described above on the earthquake data. Seismograms are used from 688 events corresponding to 31518 S-wave receiver functions (SRFs) calculated, out of which 10502 are used after sta-lta thresholding on the SRFs. A total of 89 common depth point stacks of S-wave receiver functions (SRFs) are calculated after binning, where each bin has 21 to 843 SRFs (Fig. 4.1). Fig. 4.6 shows the amplitude of the Sp phase from RF stacks indicative of the magnitude of velocity contrast. The amplitudes in Fig. 4.6 correspond to the maximum value of the positive lobe (which is equivalent to the negative velocity contrast in the SRFs) observed below the Moho.

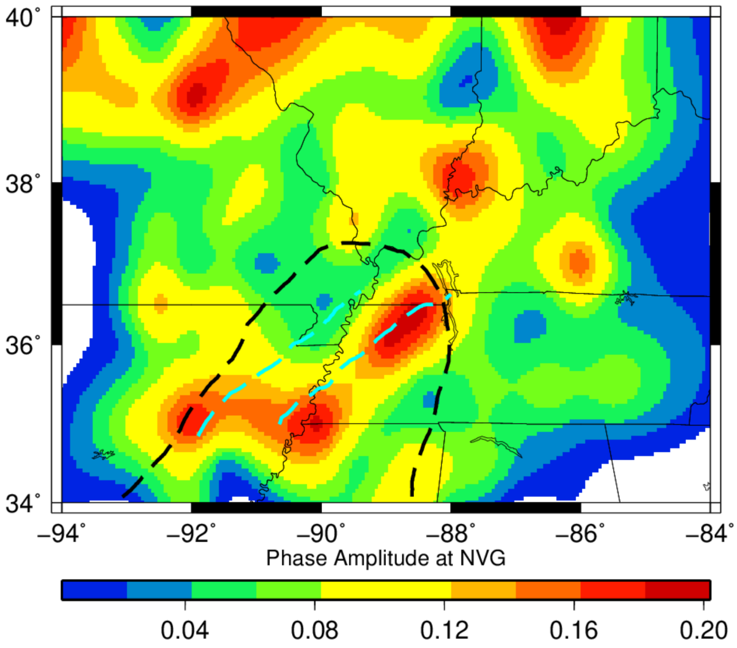

Fig. 4.6: Map showing the amplitude of the S_Np phase in the stacked SRFs. Black and cyan dashed line marks the boundary of the Mississippi Embayment and the Reelfoot rift, respectively.

Fig 4.7 shows a map of depth to the negative velocity contrast (NVC) with stacked RFs over four cross-sections. Moho depths are indicated by cyan markers as the maximum amplitude of the first positive side lobe of the main P phase (depth = 0 km) in the stacked SRFs. The Moho depths range from 30 to 44 km (Fig. 4.7). The approximate depth to the NVC is depicted using magenta markers in Fig. 4.7. We choose the depth to the NVC as the depth to the maximum negative phase below the Moho arrival in SRF stacks (Fig. 4.7(a)). The average depth of the negative velocity layer ranges between 60 and 120 km, where there is good station coverage and a high number of receiver functions per bin (see Fig. 4.1). The depth contours of the NE-SW trending low-velocity feature at 100 km depth found by Nyamwandha et al. (2016) are overlain on the NVC depth map. We also calculate the stacked SRFs following the stacking of individual seismogram components (described in Abt et al. (2010)) in Fig. S1.

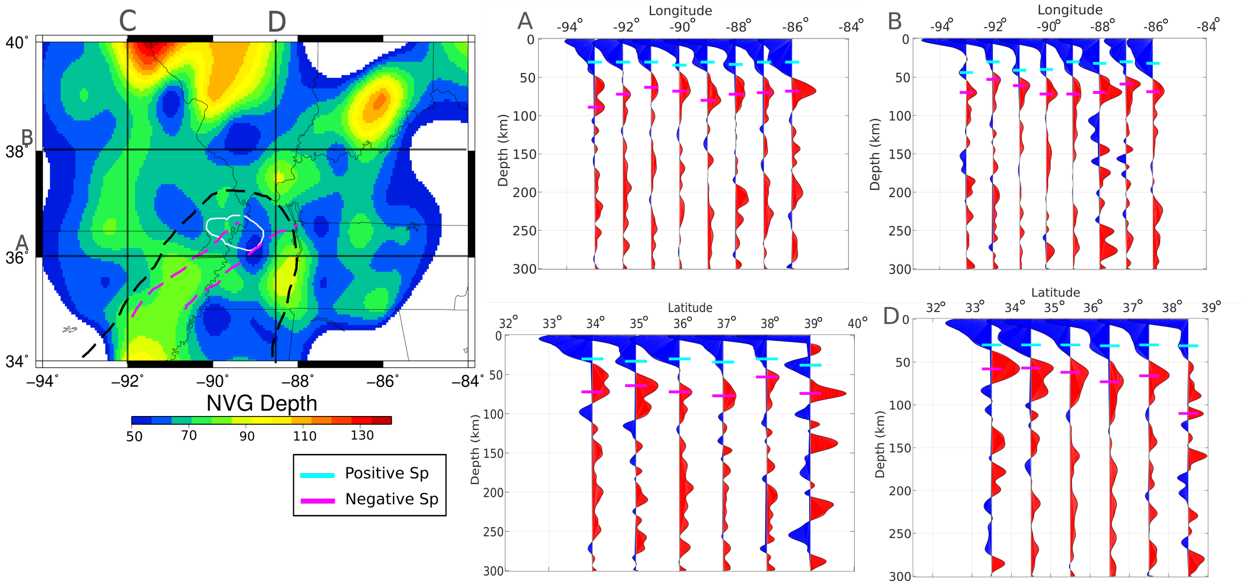

Fig. 4.7: (left) Inferred depths to the negative velocity gradient, which is estimated after depth migration and stacking the S receiver functions across the study region. The contour of the low-velocity anomaly found by Nyamwandha et al. (2016) at 100 km depth is marked by white. Black and magenta dashed line marks the boundary of the Mississippi Embayment and the Reelfoot rift, respectively. (right) Latitudinal and longitudinal profiles, corresponding to the letters and locations marked by magenta lines in the map view on the left, showing the stacked depth migrated RFs. The depth to the Moho and the negative upper mantle discontinuity is picked using cyan and magenta lines, respectively.

Previous studies have determined 1-D velocity models based on observed P-wave receiver functions (e.g., Langston 1994, Herrmann et al. 2000) but this kind of inversion is non-unique and strongly dependent on the staring model (Ammon et al. 1990). To gain a first-order understanding of the velocity model that could generate the observed Sp phase at the NVC (picked in Fig. 4.7),we first compute synthetics for four velocity models obtained by previous studies (Langston 1994, Pollitz & Mooney 2016, Chen et al. 2016, Nyamwandha et al. 2016) in the ME. We then perturb these velocity models to match the significant characteristics of the observed SRF within the Mississippi Embayment with the modeled SRF. The models for Vp and Vs, plotted in Fig. 4.8, are extrapolated from these studies to 200 km depth using iasp91 (Kennett & Engdahl 1991). The Vp model is inferred for Pollitz & Mooney (2016) and Chen et al. (2016) using a Vp/Vs ratio of 1.75. We compute synthetic seismograms for the velocity models in Fig. 4.8 assuming ray parameters ranging from 0.072 to 0.11 sec/km and an added P and S wave coda noise using Eq. and Eq. 2.5. We stack the synthetic noisy receiver functions, after correcting for the normal move-out, and compare them with the observed receiver function within the embayment in Fig. 4.9.

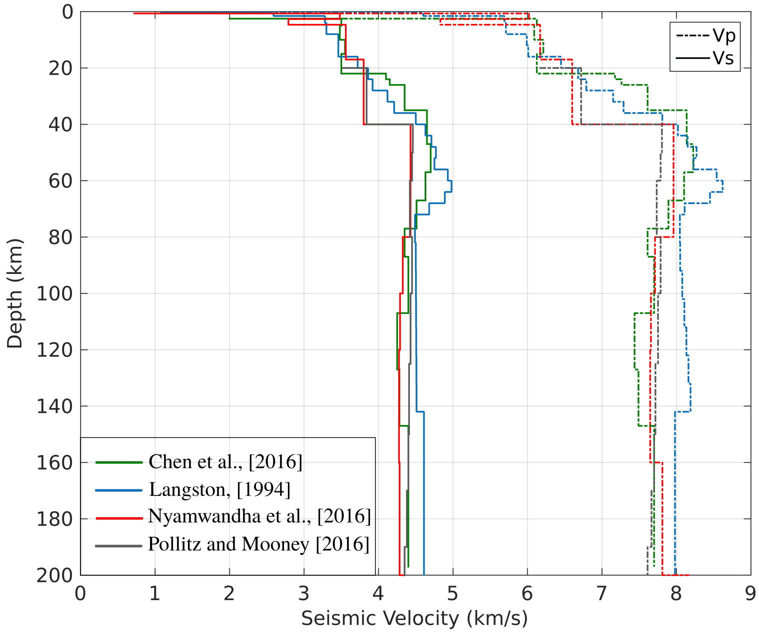

Fig. 4.8: Various velocity models documented for Mississippi Embayment. These models are used to generate synthetic receiver functions for comparison with the observed receiver functions.

There are a couple of key differences between the observed RFs and synthetic RFs from all the velocity models (Fig. 4.9). Firstly, the amplitude of the main phase in all of the observed RFs is reduced compared to the synthetic receiver functions. This difference arises because the receiver functions are stacked at the common depth points within each bin. The bin includes individual RFs having both positive and negative amplitudes due to different frequency content in the main phase. As a result, the stack sums to a reduced

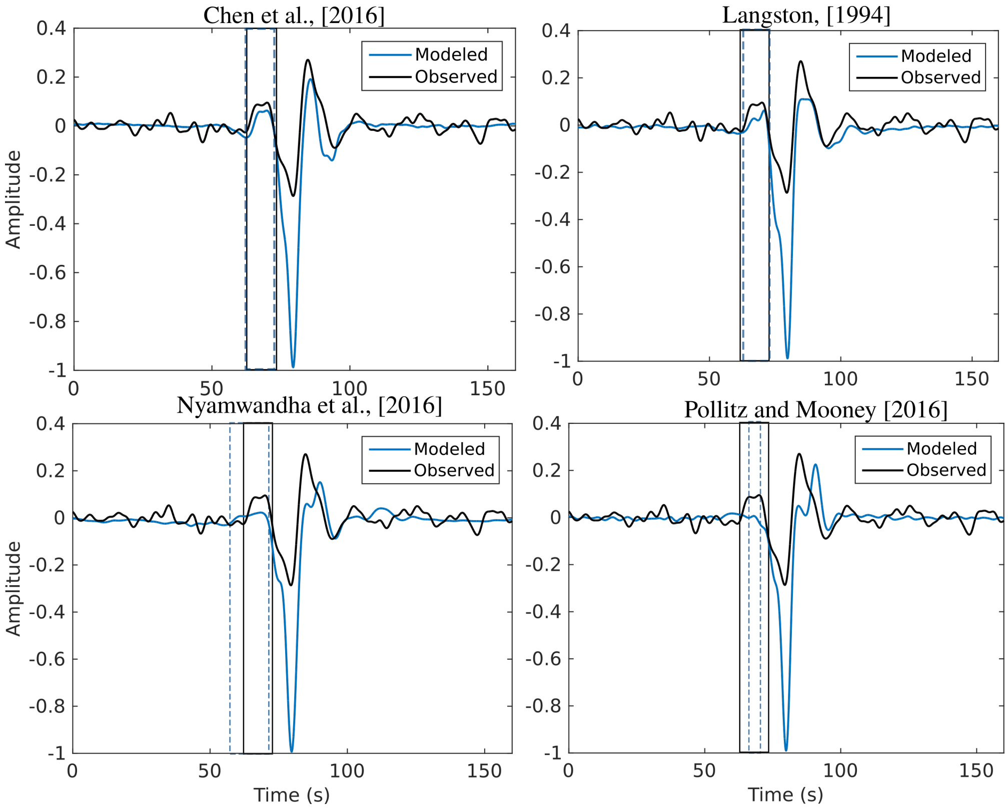

Fig. 4.9: Observed and synthetic seismograms for the Mississippi Embayment using various velocity models plotted in Fig. 4.8. Each subplot marks the Sp phase converted from the negative velocity gradient in the observed and synthetic seismogram using black and dashed blue lines, respectively.

amplitude. Secondly, the width of the Sp phase converted at the NVC is different than what is obtained in the synthetic RFs (black and dashed blue window marked in Fig. 4.9) computed for the velocity model given by Nyamwandha et al. (2016), Pollitz & Mooney (2016). This implies that the width of the low-velocity gradient may be different from what is given in these models. It is worthwhile to note that the modeled Sp phase at the NVC using Chen et al. (2016) and Langston (1994) velocity structure shows two overlapping peaks, which is also observed in the observed RF and several other RFs in our study region (Fig. 4.7). This double-lobed phase has been observed in the S-wave receiver functions by Liu & Gao (2018) and is indicative of two low-velocity layers close to each other. The best-matched width of the observed Sp phase converted at the NVC is obtained for the velocity models by Chen et al. (2016), Langston (1994) (Fig. 4.9).

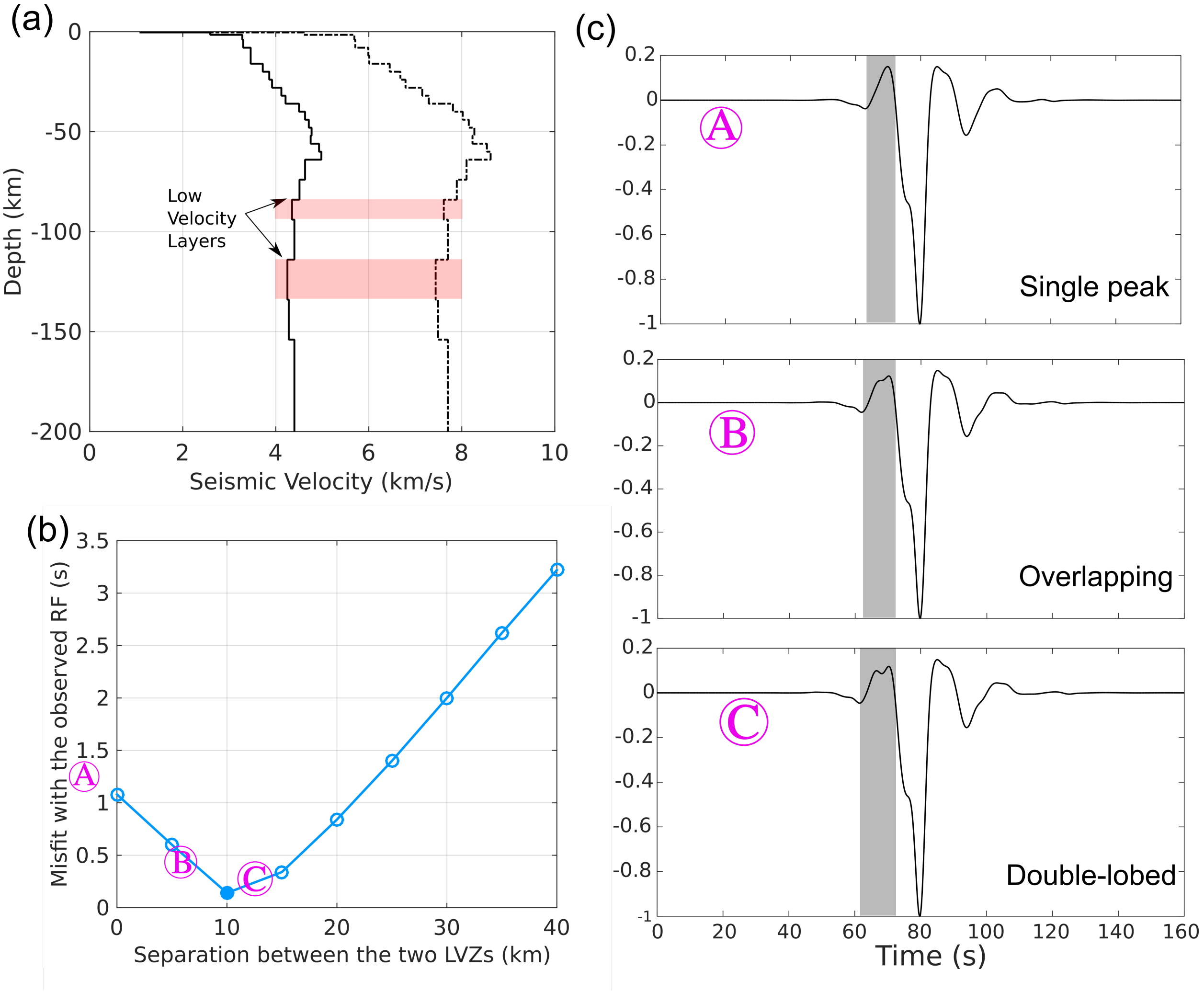

Fig. 4.10: (a)Interpretation of the observed negative Sp phase (S_Np) using a suite of synthetic velocity models modified using a velocity model combined after Langston (1994) and Chen et al. (2016). (b)The difference in the width of the observed and synthetic S_Np for different separations between the two low-velocity layers in (a). The filled circle represents the minimum misfit in the observed and the modeled S_Np phase for separation of 10 km. (c) RFs from three models employing varying separations in (b) to illustrate the single peak, overlapping and double-lobed S_Np in plots A, B, and C, respectively.

To match our observed RFs, we extend the velocity model by Langston (1994) such that after 60 km depth, we use the velocity model by Chen et al. (2016). We do this because Langston (1994) used inversion of receiver functions to get a velocity model with a higher vertical resolution than Chen et al. (2016), who use surface wave data to get their velocity model. However, the Langston (1994) velocity model does not extend to deeper depths (> 64 km). We perturb this model by varying the thickness of the two low velocity layers (marked in Fig. 4.10) from 5 to 40 km, and assuming separations between these layers from 5 and 20 km at an interval of 5 km. We calculate the difference in the width of the observed Sp phase due to the low-velocity zone (S_Np), with the S_Np phase in the computed synthetic RFs (Fig. 4.10). We choose the velocity model from Fig. 4.10 that gives the minimum difference in the width of the S_Np phase between the synthetic and the observed RF. We also mark the velocity models that produce a double lobed and overlapping phase in Fig. 4.10 and discuss those later.

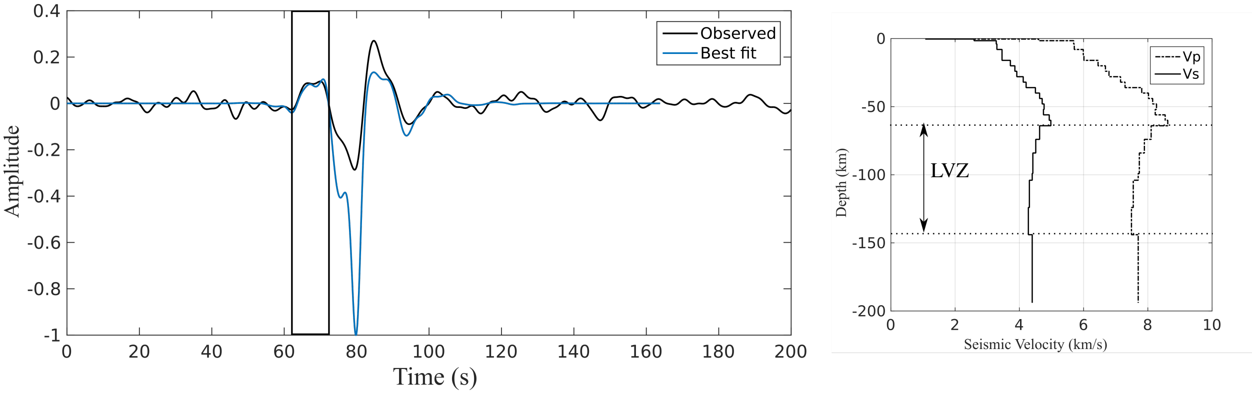

Fig. 4.11: (left) The best-fit modeled (blue) and observed (black) receiver function with the window of the S_Np phase. (right) The velocity model used to generate the synthetic RF, and the low-velocity zone (LVZ) marked for reference.

We use the model which best matches the width of the S_Np phase with observation (marked in Fig. 4.10), and modify the Vp and Vs contrast at the two adjacent low velocity layers to match the amplitude of the observed phase with the synthetic phase. We use Vp and Vs contrasts ranging between -2 to -6% at an interval of 1% while keeping the Vp/Vs ratio as 1.75 across the low velocity layer. The best fit resultant synthetic seismogram from our grid search and the corresponding velocity model are plotted in Fig. 4.11. The best-match velocity model in Fig. 4.11 has a low-velocity zone, starting at around 60 km depth and reducing velocity until $\sim$ 140 km depth.

Discussions

We explored two stacking techniques in this study to improve the signal to noise ratio of the Sp conversions: stacking individual seismogram components before performing the deconvolution (e.g., Abt et al. 2010), and stacking the individual receiver functions (e.g., Liu & Gao 2018). We find that at lower noise levels, both stacking methods show a distinguishable S_Np phase. In general, stacking the individual noisy synthetic components leads to the lower misfit between the S_Np phase than stacking the synthetic receiver functions (Fig. 4.5). This is in contrast to the earthquake data in which we find better SNR while stacking the individual receiver functions (Fig. 4.7, S1). This mismatch is likely from using a single source function in our synthetics so that stacking the individual components improves the quality of the incident S-wave used for deconvolution. Since the real data consists of multiple source functions and associated coda decays, stacking the seismogram components fails to remove the noise common to both components and is then propagated to the receiver function during deconvolution.

The maximum amplitudes of the observed S_Np phase in our study region follow the trendand are offset to the east of the Reelfoot rift (Fig. 4.6). The correspondence between the trend of the high S_Np amplitudes and the Reelfoot Rift observed in our study points to a paleo-seismic origin for the low-velocity layer, associated with rifting during during the breakup of Rodinia (Thomas et al. 2006). Rifting along the eastern margin of the US created several zones of weakness parallel to the present day Reelfoot rift (Thomas et al. 2006), which could act as a conduit for an asthenospheric upwelling. This mechanism has been recently suggested by Chen et al. (2016), Nyamwandha et al. (2016), who independently observed low S-wave velocity anomalies within the northern Reelfoot Rift. Based on this evidence, we suggest that our observed high amplitudes in the receiver functions are conversions from a low-velocity zone formed due to the emplacement of asthenospheric melts during the episodes of past Wilson cycles. We also observe high S_Np amplitude outside of the Reelfoot rift at the northern end of our domain (Fig. 4.6). This is most likely an artifact because we have fewer waveforms in the regions near the boundary of our domain, such that the noise levels are high in the stacked receiver functions.

To interpret the depths of the observed $S_N p$ phase (Fig. 4.7),we first calculate the expected depths of the lithosphere-asthenosphere boundary (LAB) in this region and then compare our observed depths with the LAB depths. There are several representative proxies for defining the LAB depth, such as a change in temperature, anisotropy, electrical resistivity, and strain rate (Eaton et al. 2009). Assuming that these measures give not too different seismic signatures, we choose to use a temperature-based LAB. The thermal LAB can be defined as the depth at which the conductive lithospheric geotherm coincides with the convective mantle adiabat assumed for the asthenosphere (e.g. Sobolev et al. 1997). Using this definition, we plot the S-wave tomography-based geotherms for the Central US from Goes & van der Lee (2002) and mantle adiabat of 1300° (representative for continental interior) in Fig. 4.12. It can be seen from Fig. 4.12 that the thermal LAB would extend to about 200 km depth within the continental interior, which is much deeper than the depth of the observed low-velocity layer in this study (around 80 - 150 km in Fig. 4.7).

We interpret the observed low-velocity layer starting at the depths between 60 km to 100 km across our study region (Fig. 4.7) as a mid-lithospheric discontinuity (MLD). This observation is consistent with the several previous studies on the S-wave receiver functions beneath the central US (Abt et al. 2010, Hopper et al. 2014, Lekić & Fischer 2014, Hansen et al. 2015, Hopper & Fischer 2015, Liu & Gao 2018, Chen et al. 2018) and in other continental interiors worldwide (e.g., Thybo & Perchuć 1997, Lekic & Romanowicz 2011, Tharimena et al. 2016). However, the origin of a continuous MLD remains debatable. Proposed mechanisms for a global MLD over continental cratons include seismic anisotropy (Yuan & Romanowicz 2010, Wirth & Long 2014), partial melting (Wölbern et al. 2012), mineralogical alterations from melt (Hansen et al. 2015), and change in rheology from elevated temperature or water content (Karato et al. 2015). We do not comment on a preferred mechanism for the MLD due to the lack of other observational

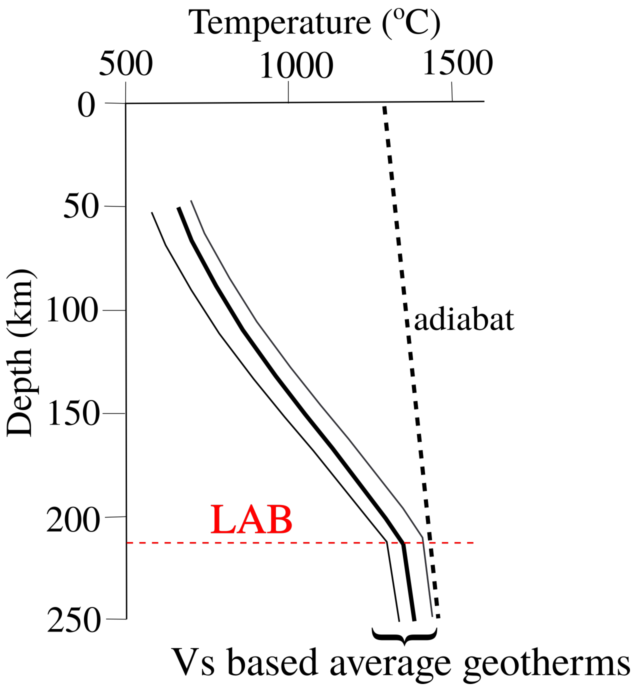

Fig. 4.12: Thermal lithosphere-asthenosphere boundary defined for the continental interior at the intersection of the Vp based geotherm taken from Goes & van der Lee (2002) and mantle adiabat with a potential temperature of 1300°.

constraints. Instead, we compute and explore the feasibility of required temperature change, melt amount, and water content that may explain the velocity contrast for the observed phase-amplitude

Based on our synthetic tests, we find that an MLD amplitude equal to 10% of the main phase corresponds to a 5% decrease in the S wave velocity. Computing the sensitivity of the S-wave velocity to temperature from Goes et al. (2000), we find that elevated temperatures by $\sim$ 430 K are needed to explain the 5/% Vs drop at 80 km depth.Based on the observed variation in MLD phase amplitudes and depths, it is unlikely that a common mechanism could explain the variable amount and depth of increasing temperatures globally within the lithosphere. Assuming that the observed decrease in velocity is from increased water content, a C_{OH} of about 1800 H/Si ppm is required (Karato & Jung 1998). This value is equivalent to $\sim$ 100 H_2O ppm water content for the mantle in the depth range of the observed MLD (Dixon et al. 2004); this is too wet for continental interiors. The presence of 1% of the partial melt can explain the shear wave velocity decrease (Hammond & Humphreys 2000). However, we can not attribute the MLD to melt, due to lack of evidence for high surface heat flow over continental cratons (Davies 2013). Compositional change from metasomatic alterations from subducting or subducted oceanic lithosphere results in lawsonite-eclogites compositions and reduces the velocity by 3-7% (Connolly & Kerrick 2002). However, such conditions are not present in regions far from an active subduction zone or overlain with subducted oceanic lithosphere to explain the globally observed MLD. Therefore, it is likely that the origin of the observed MLD is not from a single factor such as temperature, water content, or melt. Instead, a combination of these factors provides more compelling evidence leading to a velocity drop within the lithosphere.

We only interpret one of the stacked receiver functions for the corresponding velocity model in Fig. 4.11. It is possible to infer the lateral variations in the velocity structure using other stacks, and the corresponding initial velocity model for that stack. Since there is available literature of high-resolution shear velocity estimates from seismic tomography in this region (Nyamwandha et al. 2016, Chen et al. 2016), we do not attempt to recover the 3-D velocity model from our observed receiver functions. Instead, we focus on the relationship between the S_Np amplitude and the velocity contrast and S_Np phase width and layer thickness in Fig. 4.10 and Fig. 4.11, respectively.

The best-fit velocity model for our synthetic receiver function stack is based onLangston (1994) and Chen et al. (2016) in Fig. 4.11. The high-velocity reflector in the upper mantle at 55-60 km depth in the velocity model of Langston (1994) is also observed by Catchings (1999). The presence of this high-velocity layer provides a negative velocity contrast below it. Indeed, this is another plausible explanation for the observed S_Np phase in our receiver functions consistent with observations. The origin of the high-velocity layer is not clearly understood or explored in this study; however, compositional variations for anhydrous eclogites could increase the seismic velocity (Connolly & Kerrick 2002).

We compare the observed MLD in our study region in the light of some previous studies on seismic tomography and geologic models. A thinned lithosphere beneath the Mississippi Embayment has been proposed by Hildenbrand (1985), Cox & Van Arsdale (2002), Biryol et al. (2016), implying a shallower MLD beneath the embayment compared to the surroundings, which is not observed in our study (Fig. 4.7). This inconsistency maybe because of the probable difference in the timings for the two events. The thinning of the lithosphere beneath the embayment occurred in mid-Cretaceous (Cox & Van Arsdale 2002), which may not coincide with the origin of the MLD. Since the MLD has been observed globally over the continents, it is likely formed concurrently with the cratonic lithosphere. Thus, the thinning of the lithosphere could have occurred after the layering within the lithosphere. Another interesting observation by recent teleseismic tomography studies (Nyamwandha et al. 2016, Chen et al. 2016) is the low Vs (-5%) anomaly at about 80 - 160 km depth beneath the northern ME. We do not observe the top of this low anomaly feature in our depth map (Fig. 4.7). A possible explanation would be the limited resolution of our stacked receiver function, i.e., one waveform in 1° bin, compared to the 100 km lateral width of the low Vs anomaly found by the tomography studies.

We observe the double-lobed negative Sp phase corresponding to the MLD at several locations in our study region (Fig. 4.7).Based on our synthetics using 1-D velocity models (Fig. 4.10), we find that the double-lobed phases are formed due to overlap of S to P conversions from two negative velocity contrasts, and the width of each lobe is proportional to the thickness of the low velocity layers. Moreover, we can also roughly infer the separation distance of the two layers. A higher distance between the peaks of the double-lobed MLD implies a greater separation between the two layers. Double MLDs have been previously reported by Chen et al. (2018) and described as possible lithospheric accretion or due to magmatism from a tectonic event. Since we explain the MLD as a result of multiple origins, including temperature, composition, or water content, we think that the presence of double MLDs is indicative of differences in depths of these seismic indicators within the lithosphere.

Conclusions

We use S-wave receiver functions to find the lithospheric discontinuities beneath the Mississippi Embayment. We extend the noise model from a previous study by Hammond & Humphreys (2000) to include the S-wave coda model. We conduct noise analysis on synthetic seismograms using realistic noise components and different stacking methods to detect a negative velocity contrast. Based on this analysis, we find that it is possible to delineate the Sp phase converted at the top of low-velocity layer at low noise-levels and high number of stations. We also find that the stacking the receiver functions after deconvolution gives a better S/N ratio than stacking the seismogram components and then deconvoling them. Our results on the earthquake data indicate a continuous negative Sp phase in our receiver functions across the Mississippi Embayment at depths ranging between 60 to 100 km. We interpret this Sp phase as a mid-lithospheric discontinuity. We also find a strong negative velocity contrast trending along the Reelfoot Rift, suggesting that the velocity drop could have a past tectonic origin. At several locations, we image a double- lobed Sp phase, hinting for multiple lithospheric discontinuities within this region. Our investigation into possible origins of the mid-lithospheric discontinuity suggests multiple factors, including both thermal and compositional changes.

Supplementary figure

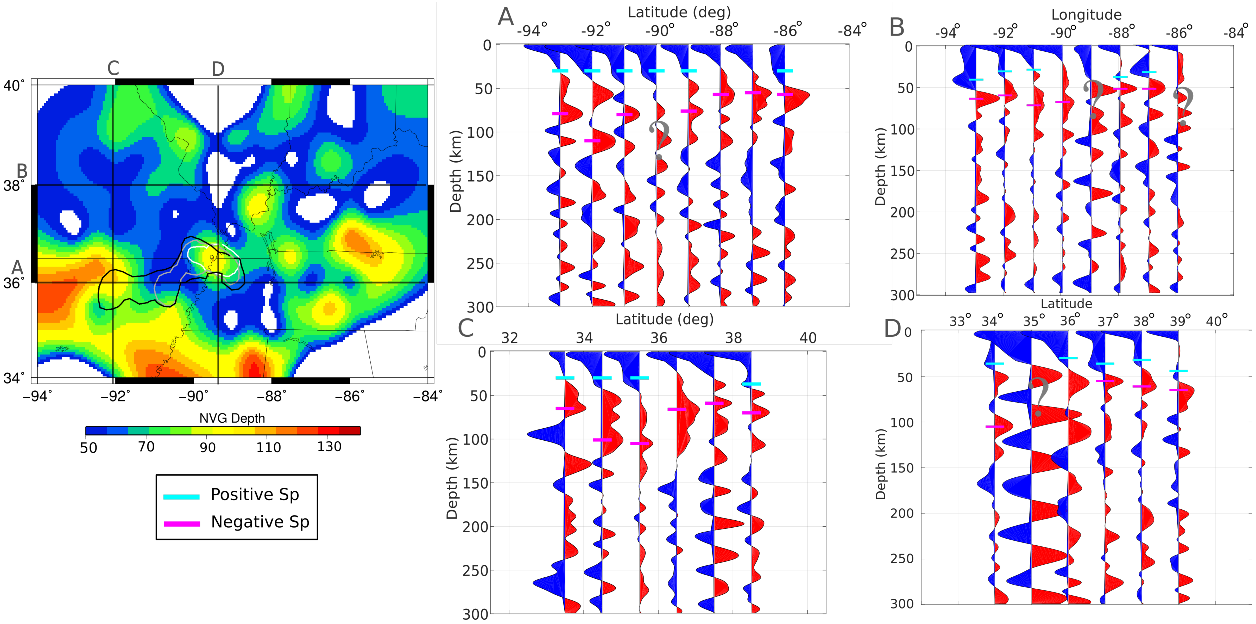

Fig. S1: (left) Inferred depths to the negative velocity gradient, which is estimated after depth migration and stacking the seismogram components following the technique by Abt et al., (2010). The contour of the low-velocity anomaly found by Nyamwandha et al. (2016) at 80, 100 and 160 km depth is marked by grey, white and black, respectively. Black and magenta dashed line marks the boundary of the Mississippi Embayment and the Reelfoot rift, respectively. (right) Latitudinal and longitudinal profiles, corresponding to the letters and locations marked by magenta lines in the map view on the left, showing the stacked RFs. The depth to the Moho and the negative upper mantle discontinuity is picked using cyan and magenta lines, respectively.

Chapter 5

A possible numerical model to explain the unusual Pn anisotropy in the Central and Eastern US

A version of this chapter will be submitted for publication as Saxena, A., Choi, E. and Powell C. A possible numerical model to explain the unusual Pn anisotropy in the Central and Eastern US.

Abstract

A recent Pn anisotropy study finds an intriguing spiral-shaped pattern centered at the New Madrid Seismic Zone (NMSZ), in the northern Mississippi Embayment (ME). However, SKS splitting results for the same region do not show this circular pattern implying a shallow-depth origin for the pattern. We suggest that the mantle flow arising from the combination of a sinking mafic body below the lower crust and a low-velocity asthenospheric upwelling beneath the NMSZ can account for the observed circular anisotropy pattern. We set-up three dimensional forward numerical models, and use appropriate geometries and physical properties of the two anomalous features, the mafic body, and the low-velocity zone, after a careful literature review. The directions of maximum finite strain (ϵ_1) are indicators of seismic anisotropy and ϵ_1 values are computed from the modeled mantle flows. Since Pn can sample the shallow brittle parts of the crust and uppermost mantle, we also calculate the directions of maximum horizontal compressive stress (S_H), which aligns with micro-cracks in the upper crust. We find that roughly 25% of the observed anisotropy could be explained by ϵ_1 output from our model. Model tests varying the density of the mafic intrusion and the viscosity of the lower crust suggest that at least $+200 \mathrm{kg/m^3}$ density differential of the intrusion, and a weak lower crust with viscosity around 10^{19}Pa·s is needed to best-match the observed anisotropic pattern. These findings are consistent with the suggestions made in previous studies.

Introduction

The interior of the Earth has been long proven to be elastically anisotropic (Anderson 1961, Hess 1964, Nicolas & Christensen 1987, Silver 1996, Mainprice et al. 2000, Crampin & Peacock 2008). Within the mantle, the lower mantle is generally assumed to be effectively isotropic (Meade et al. 1995, Wüstefeld et al. 2009), except the D” layer at the core-mantle boundary (e.g., Lay et al. 1998). On the other hand, the upper mantle is highly anisotropic, with the minimum value of anisotropy in depth range 300 to 500 km (Montagner 1998). Crustal anisotropy is usually much smaller: about 20% of the mantle anisotropy (Silver et al. 2001).

Anisotropy in the continental upper mantle is more challenging to explain than the oceanic upper mantle (Becker et al. 2006, Conrad et al. 2007, Becker et al. 2007). The study by Conrad et al. (2007) utilized global density heterogeneity and the surface plate motions to setup numerical mantle models. Comparison of the instantaneous global flow models with the global SKS splitting results at asthenospheric depths ($\sim$ 225 km) in Conrad et al. (2007) showed a much better fit of the oceanic anisotropy than the continental anisotropy. This is because the oceanic lithosphere is thinner and younger such that anisotropy records the dominant asthenospheric flow that can be explained by global mantle circulation models. However, beneath the continents, frozen-in anisotropy (remnant anisotropy) in the lithosphere plays an important role, for which a general model is difficult to develop.

Some models for depth-dependent anisotropy within the continental lithosphere have been suggested. Crampin et al. (1984) proposed that seismic anisotropy is produced from fluid-filled micro-cracks created parallel to the local maximum compressive stress directions. They also suggested that this stress-induced anisotropy is observed only at upper crustal depths (<20 km), where temperature and pressure are relatively low, slowing down or preventing crack healing. Another mechanism for anisotropy in the lithosphere is the alignment of fast-axis along the plane of macroscopic geological features such as faults, sedimentary layers, etc., referred to as structural anisotropy (e.g., Kaneshima 1990, Boness & Zoback 2006, Yang et al. 2011). This type of anisotropy occurs in response to the paleo-stress and tectonics during the formation of these features. At greater depths in the lower crust and upper mantle (> 20 km), rocks can deform in a ductile manner and a lattice preferred orientation (LPO) can be produced in the mantle minerals (Zhang & Karato 1995, Tommasi et al. 2000). The fast-axis of a seismic wave aligns with the strain-induced LPO direction providing information about the mantle deformation history (Ribe 1992). To understand the link between observed anisotropy and its contributing factors, forward modeling of the anisotropy is often utilized (West et al. 2009, Alpert et al. 2013, Li et al. 2014).

Pn anisotropy found by Basu & Powell (2019) beneath the Central and Eastern US (CEUS) presents an intriguing problem; the Pn anisotropy forms an unusual spiral-like pattern as well as shear wave (SKS) splitting found by Nyamwandha & Powell (2016) for the same region approximately aligns with the absolute plate motion directions (Fig. 5.1). This difference implies a depth-dependent source of anisotropy in the CEUS, which has not been investigated previously.

The objective of this study is to suggest an explanation for the observed Pn anisotropy beneath the NMSZ using geodynamic modeling. We set up our numerical models based on the two most prominent velocity features found by previous studies that imaged the lithosphere of the CEUS. This is essential to understand the correlation of the observed Pn anisotropy with the present velocity heterogeneous features or deformation caused by them. A similar approach has been adopted in the western US in the Great Basin, where a circular pattern in the SKS fast-axis orientations is observed (Zandt & Humphreys 2008, Huang & Zhao 2013). It is not clear whether directions of maximum compressive stress (indicating the frozen-in melt cracks) or maximum finite strain (indicating the mantle deformation over time) dominate the Pn anisotropy of this region.

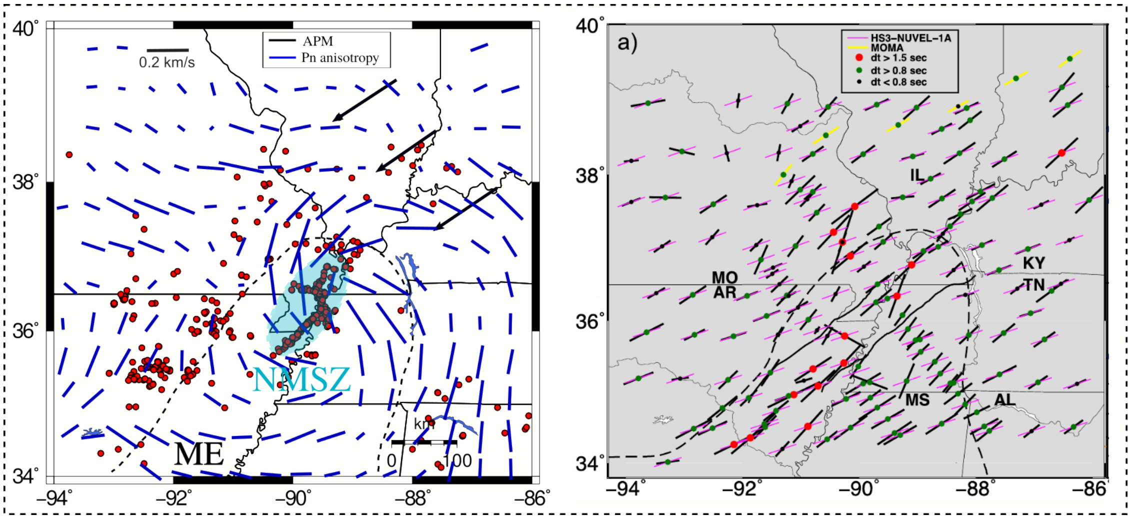

Fig. 5.1: The disparity in the observed Pn anisotropy (left) (Basu & Powell 2019) and SKS splitting results (right) (Nyamwandha & Powell 2016) in the Central and Eastern US. Each subplot also shows the direction of the absolute plate motion (APM) from the HS3-NUVEL-1A model (Gripp & Gordon 2002) in black, and the outline of the Mississippi Embayment (ME) in magenta. The spiral-like Pn anisotropy is centered at the New Madrid Seismic Zone (NMSZ). The lengths of the blue (Pn anisotropy) and green (SKS splitting) lines are proportional to the seismic anisotropy.

Therefore, we consider both stress and strain in our model results for comparison with the observed anisotropy.

Data assimilation strategy

We focus on two prominent seismic anomalies observed in the CEUS. One is a well-known high-density mafic body embedded in the lower crust beneath the New Madrid seismic zone in the northern Mississippi Embayment, observed in various seismic and gravity studies (Hildenbrand 1985, Stuart et al. 1997, Chen et al. 2016, Nyamwandha et al. 2016, Levandowski et al. 2016, Basu & Powell 2019, Geng et al. in-prep). The other feature is a low-velocity region below this mafic body at the depths of 80-200 km (Pollitz & Mooney 2014, Nyamwandha et al. 2016, Chen et al. 2016, Geng et al. in-prep). This low-velocity anomaly was recently imaged after the deployment of a dense seismic network array by EarthScope in the CEUS.

We assimilate the available literature on seismic tomography, gravity, and magnetic data for the CEUS using a technique called "vote maps" (Lekic et al. 2012). The basic principle behind vote maps is to combine the observations acquired using different data sets, inversion parameters, and techniques. We first collect previous studies that delineated the geometry of the observed anomalous feature. We choose a depth range most common for each feature and plot the depth slices of all the collected geometries on one map (Fig. 5.2). A depth-sliced geometry of a feature is a closed set of geographic coordinates (i.e., ordered pairs of latitude and longitude). A rectangular grid of geographic coordinates is created such that it encompasses the union of all the feature geometries. Each point of the grid gets a vote when it belongs to a feature. The total number of votes at a point is equal to the number of studies that imaged the feature at that point. For this study, we define a feature as a set of locations with at least three votes. This threshold value is appropriate for our study region, where high-resolution tomography studies have become available only recently.

The structure of the two anomalies with depth is difficult to compile as the previous studies do not provide the 3-D image, but rather several depth layers. These layers are at different depths in different studies. Therefore, we use the highest resolution study till now

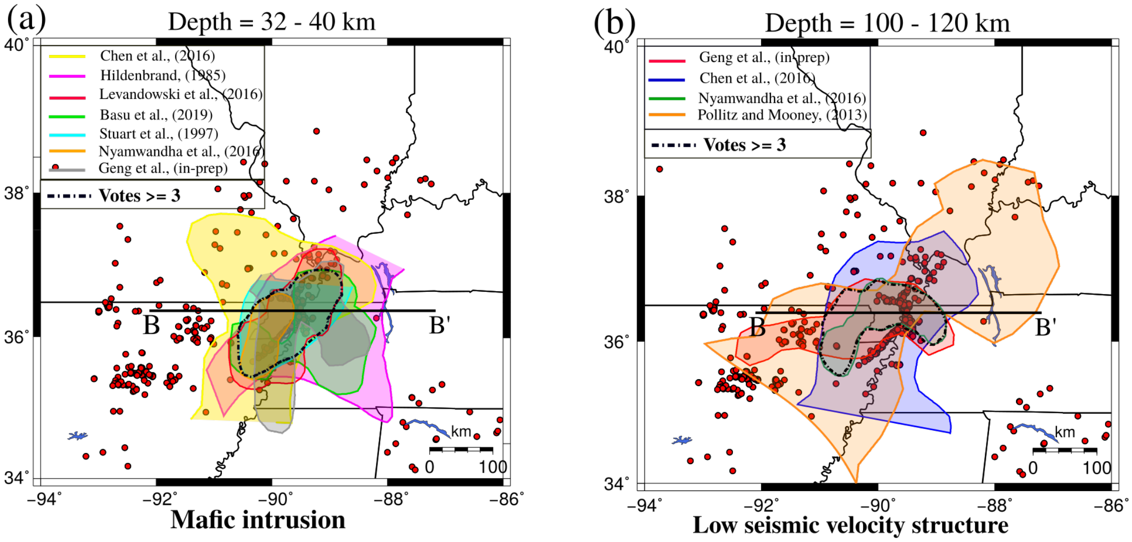

Fig. 5.2: Vote maps outlining (a) the mafic intrusion (MI) in the lower crust and (b) the low-velocity zone (LVZ) in the upper mantle. The geometry of each feature, suggested by a study, is represented by a unique color in the legend. The dashed-dotted line marks the geometry of the MI and the LVZ used in numerical models, where vote count is more than three. The cross-section along BB' is shown in Fig. 5.3.

by Nyamwandha & Powell (2016) to approximate the shape of the low-velocity anomaly with depth. For the mafic intrusion, we use the dimensions from Fig.1 in Stuart et al. (1997), who use seismic and gravity data to image the mafic body in detail. Fig. 5.3 shows the observed anomalies in the cross-section used for the depth structure of these anomalies.

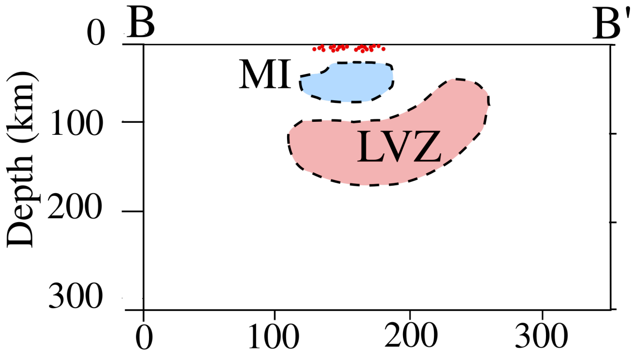

Fig. 5.3: Cross-section BB' through the northern Mississippi Embayment from Nyamwandha et al. (2016) (refer to Fig. 5.2 for plane view) illustrating the depth structure of the low-velocity zone (LVZ) and the mafic intrusion (MI). Red dots represent the approximate hypocenter locations.

Numerical methodology

Model setup

The numerical models are constructed with an open-source finite element code, ASPECT version 2.0.0 (Heister et al. 2017, Kronbichler et al. 2012, Bangerth et al. 2018), which is modified here to include finite strain field calculations in the existing multi-component material model.

The reference model (Fig. 5.4) includes the two anomalous features, the mafic intrusion (MI) and the low-velocity zone (LVZ), and adopts material properties derived from previous studies. The lateral extent of this model is 600 km×600 km to represent the study region (Fig. 5.2), and the depth extends to 200 km to include the two anomalies (Fig. 5.3). The model is divided into three layers, upper crust, lower crust, and mantle. Each layer has a constant density and constant viscosity. The thickness of the upper crust is 16 km, and its viscosity is assumed to be 10^{23} Pa·s to represent the elastic behavior. The viscosity of the 24 km-thick lower crust is based on the theoretical model of Pollitz et al. (2001) on the sinking mafic intrusion in our study region. The representative viscosity of 10^{21} Pa·s is used for the mantle. Densities of the three layers are taken from Burov (2010). The approximate geometries of the two anomalies are constrained, as described in the previous section. The density differential of MI in the reference model is assumed to be $+200$ kg/m^3 with the surrounding lower crust (Levandowski et al. 2016) and that of LVZ to be -70 kg/m^3. The latter corresponds to -6% Vs anomaly according to the empirical velocity-density relationship for the mantle by Levandowski et al. (2015). Without the available constraints, the viscosity of the two anomalies is assumed the same as the mantle, 10^{21} Pa·s. An adiabatic initial temperature distribution with the surface potential temperature of 1600 K is used in the model (Fig. 5.3). The bottom boundary is assumed as free slip and the top boundary as a free surface, and a no-slip boundary condition is imposed at all sides. All boundaries have temperature equal to the initial temperature distribution.

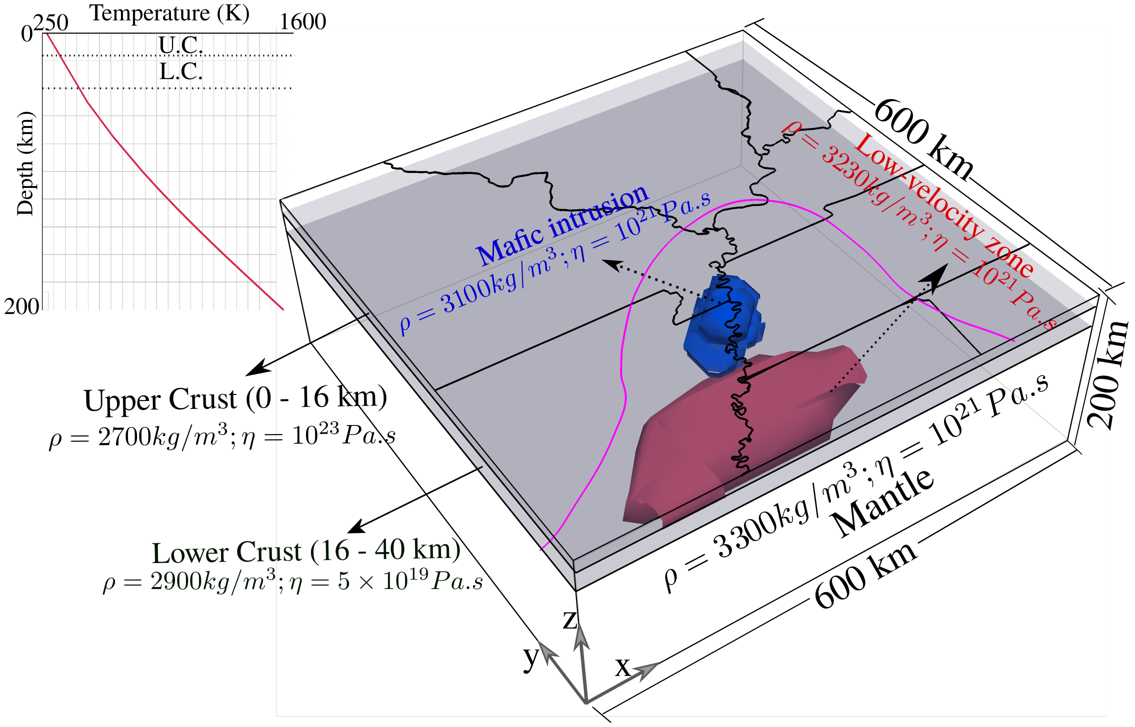

Fig. 5.4: Reference model used in ASPECT for the calculations of stress and strain fields. The model domain consists of three depth layers: upper crust, lower crust, and mantle. Blue and red iso-surfaces represent the anomalous mafic intrusion, and the low-velocity zone, respectively. The corresponding densities and viscosities of all the features are indicated for our reference model. Black lines mark the state boundaries. Magenta line outlines the Mississippi Embayment. The initial adiabatic temperature profile used is shown in the top left corner.

The model is discretized into 32 elements along each direction, and adaptive mesh refinement is used to further refine the two anomalous features by a factor of two. Since we employ a compositional field in ASPECT for the upper crust, the lower crust, the mafic intrusion, and the low-velocity zone, with the additional nine compositional fields for storing the components of the finite strain, the number of degrees of freedom in our model with the current refinement is more than 4 million. We restrict all our calculations with this value of discretization, which ensures that the anomalies are resolved without being computationally too expensive.

We test the effect of the viscosity of the lower crust on the sinking of the high-density mafic intrusion by modifying the viscosity of the lower crust between 10^{18} Pa·s and 10^{21} Pa·s and the density differential of the mafic intrusion from +50 kg/m^3 to +250 kg/m^3 with the lower crust. We also observe the isolated effects of the mafic intrusion and the low-velocity zone on the stress and strain fields.

Model outputs for anisotropy

The two widely used indicators for anisotropy are maximum horizontal compressive stress directions (S_H) (e.g., Yang et al. 2011, Araragi et al. 2015) and maximum finite strain (ϵ_1) (e.g., McKenzie 1979, Ribe 1992). The preference of one indicator over the other is determined by the depths sampled by the seismic waves. At shallower depths (<20 km), anisotropy could parallel S_H (Yang et al. 2011), whereas, at greater depths (>20 km), flow directions represented by finite strain might be the dominant mechanism for the observed anisotropy (Becker et al. 2003). Since Pn travels through the crust into the layer just below the Moho, we compute both ϵ_1 and S_H as measures for the observed anisotropy in our numerical models.

We compute ϵ_1 and S_H for all the model setups at a depth of 40 km, which is an appropriate depth for the Moho in our study region (Basu & Powell 2019). The outputs are determined at time 10^4 years in our model runs. We choose this time because our model is based on the study by Pollitz et al. (2001), where it is suggested that sinking of the mafic intrusion began with the sudden weakening of the lower crust around 9 k.y. ago. Moreover, the models are set up using the present observational studies, and our interest lies in the most recent deformation perturbing the local stress and strain field by the anomalous features investigated in this work.

To facilitate the comparison of model results with the observed anisotropy, we divide model results into four zones, such that each zone has a roughly uniform fast direction (Fig. 5.5). It is straightforward to compare the observed anisotropy in each zone with the corresponding model outputs. Fig. 5.5 shows the division of the region into zones I to IV based on the distinguishable direction in each zone. The spiral-shaped pattern is dominantly represented by zones II and III. Zone II includes most of the New Madrid seismic zone (NMSZ) has an overall direction of NNW-SSE, whereas the zone III north of the NMSZ shows an overall direction of NNE-SSW. Zone I (dominant E-W direction) and zone IV (dominant N-S direction) represent the distant effects of the spiral anisotropy along the model boundary.

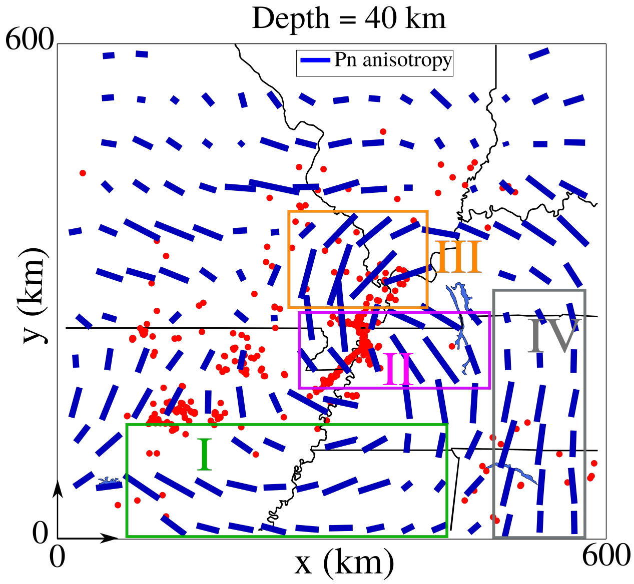

Fig. 5.5: Division of the observed anisotropy results into zones I, II, III and IV. The output stress/strain at 40 km depth is used for comparison with the observations. The zones are distinguished by different bounding box colors.

We quantify the consistency of the model results with the observations with a correlation ratio (C) that is defined as the fraction of model points at which S_H or ϵ_1 coincides with the mean fast direction of each zone within a $\pm$ 10° range.

Results

The reference model shows an overall better correlation of ϵ_1 compared to S_H with the observed anisotropy. Fig. 5.6 shows both ϵ_1 and S_H from the reference model output overlain on top of the observations. Both ϵ_1 and S_H are horizontal within the mafic intrusion (MI). However, further east and west from the mafic intrusion, the ϵ_1 form a semi-circular pattern while S_H is approximately radial (Fig 5.6). The correlation ratio, C, for the reference model within each zone is shown in Fig. 5.7(a). The averaged C for ϵ_1 in all zones is ~ 0.25, varying between 0 at zone II to about 0.6 at zone IV. On the other hand, C is ~ 0.09 averaged over all zones for S_H, reducing consistently from ~ 0.3 in zone I to 0 in zone IV.

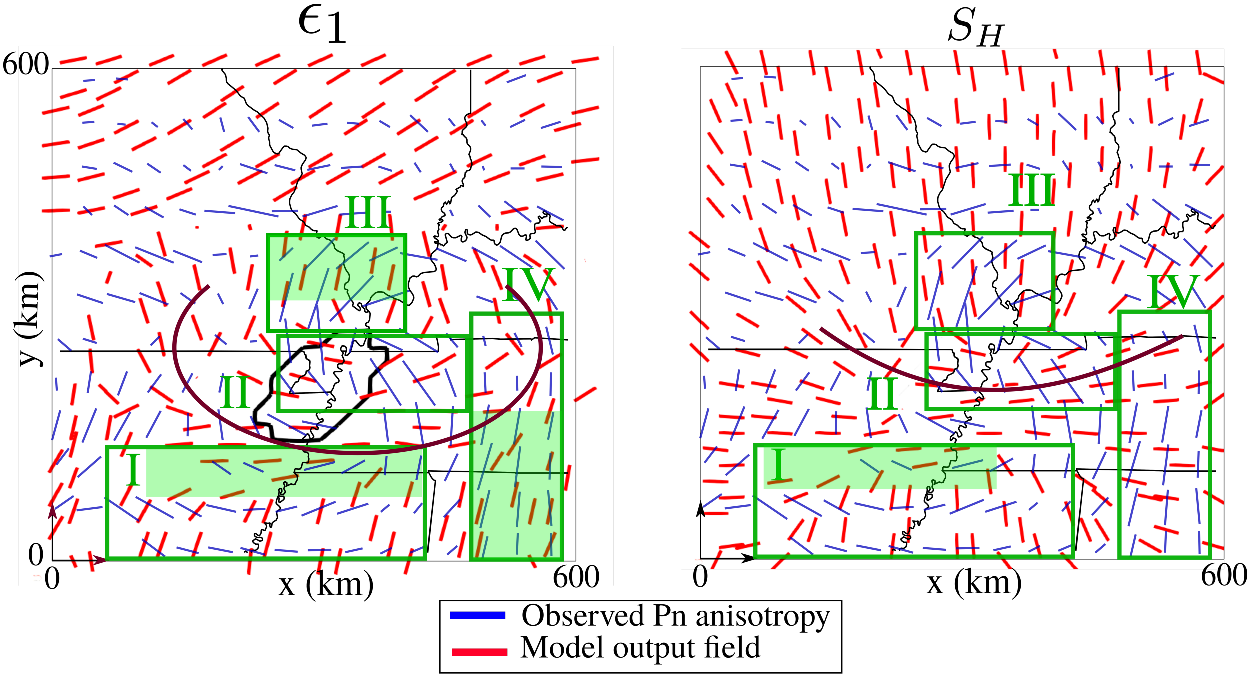

Fig. 5.6: The observed anisotropy results (blue lines) along with the reference model output, ϵ_1 (left) and S_H (right), directions every five model points (red lines). Each zone is bounded by green box and the filled region shows areas with good correspondence between the modeled and the observed anisotropy. The black solid line marks the boundary of the mafic intrusion at depth 40 km. Tangents to the maroon curve in each plot are approximately parallel to the local fast directions, which are circular and radial in the output ϵ_1 and S_H, respectively.

Effects of isolated anomalies

We isolate the two anomalies to observe their respective contributions to anisotropy. The computed correlation ratio, C, of the models for both ϵ_1 and S_H within each zone is shown in Fig. 5.7. The model with the isolated mafic intrusion (MI) has an average C of 0.14 in the output ϵ_1; C is almost zero or very low in zone I (~ 0) and zone II (~ 0.02), and much greater in zone III (~ 0.3) and zone IV (~ 0.2) (Fig. 5.7b). The model with the isolated low-velocity zone (LVZ) has an average C of 0.1 in the output ϵ_1, which is almost zero in zone III and between 0.1 and 0.2 for the other zones (Fig. 5.7c). The output S_H has an overall C as 0.17 and 0.02 for the models with the isolated MI and the LVZ, respectively.

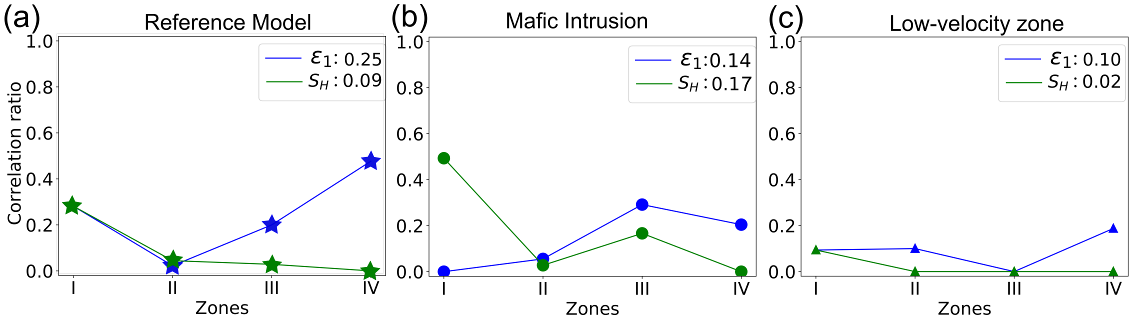

Fig. 5.7: Correlation ratio of the model outputs used as anisotropy indicators, ϵ_1 (blue) and S_H (green) within each zone for different model setups: (a) the reference model, (b) the model with only the high-density MI, and (c) the model with only the LVZ. The average correlation ratio is noted for each model setup in the top right.

Effects of the mafic intrusion density

To observe the effects of the density of the MI on the output stress and strain field, we setup models with different density differential ($\Delta\rho_m$) between the intrusion and the surrounding lower crust. $\Delta\rho$ is systematically varied between +50kg/m^3 and +250kg/m^3 at an interval of +50kg/m^3. The reference model has a $\Delta\rho_m$ of +200kg/m^3. The model results show an increase in the correlation ratio of ϵ_1 with an increase in the $\Delta\rho_m$ in zones III and IV (Fig. 5.8). On the contrary, zones I and II remain largely unaffected with the different density contrasts. The S_H values do not show any apparent trend with $\Delta\rho_m$.

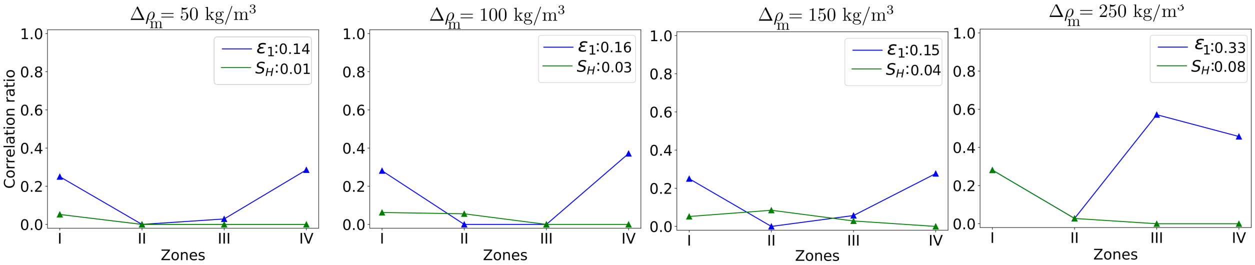

Fig. 5.8: Same as Fig. 5.7(a) but for different density contrasts of the mafic intrusion with the lower crust ($\Delta\rho_m$).

Effects of the lower crustal viscosity

Viscosity of the lower crust (η_{LC}) is systematically varied between 10^{18} Pa·s and 10^{21} Pa·s. η_{LC} is 5×10^{19} Pa·s in the reference model. The C values (Fig. 5.9) show that ϵ_1 for $\eta_{LC} = 10^{19}$ Pa·s has a maximum correlation ratio with the observations in zones III and IV. The S_H correlation ratio increases with η_{LC} up to 10^{20} Pa·s in zone I but such a systematic sensitivity to η_{LC} is not found in the other zones.

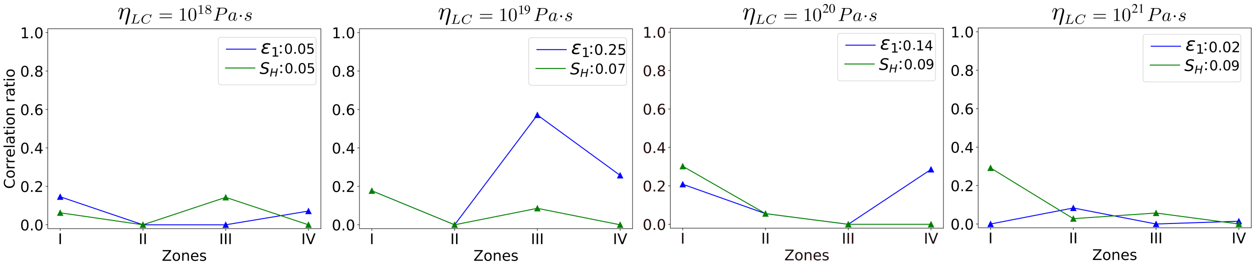

Fig. 5.9: Same as Fig. 5.7(a) but for different viscosities of the lower crust (η_{LC}).

Discussion and summary

Comparison of all the model results in terms of C values indicates that ϵ_1 aligns better with the observed fast directions than the S_H (Fig. 5.7, Fig 5.8, Fig. 5.9). Under our hypothesis that the buoyancy-driven flow from the MI and the LVZ generates stress and strain fields, the results imply that deformation in the upper mantle contributes more to the observed anisotropy than the stress-induced cracks. This conclusion is consistent with the ray-paths of the Pn wave, which travel in the layer just below the crust before being recorded at the surface. At these depths ($>=$ 40 km), almost all cracks heal with high pressure and temperature conditions (Crampin et al. 1984, Brantley et al. 1990, Tenthorey & Cox 2006).

ϵ_1 due to the sinking MI is better correlated with the fast direction of zone III than that of zone II, while ϵ_1 generated by the rising LVZ shows the opposite association. The model with MI only (Fig. 5.7b) produced ϵ_1 directions such that C is low (~ 0.05) in zone II and high (~ 0.3) in zone III. The model with the LVZ only shows a greater C (~ 0.1) in zone II than in zone III (~ 0). This is because the MI produces a radial pattern of ϵ_1

directions around it (Fig. S1), which aligns better with the fast directions in zone III than that of zone II (Fig. 5.5). In contrast, the LVZ produces a circular ϵ_1 pattern (Fig. S1), which aligns slightly better with zone II fast direction than with that of zone III (Fig. 5.5).

The MI-only model shows a better correlation with the observed anisotropy in both output fields, S_H, and ϵ_1 than the LVZ-only model (Fig. 5.7). A possible reason is that the LVZ is located in the depth range 100 to 150 km, and its effect at the depth 40 km used for our models is less significant compared to the MI, lying at depths of 22 to 40 km. Moreover, the buoyancy effect generated by the MI is higher than that of the LVZ, due to its lower density contrast with the surrounding mantle (Fig. 5.4).

The density contrast of the MI with respect to the surrounding lower crust ($\Delta\rho_m$) has minimal impact on ϵ_1 up to +150 kg/m^3 but the ϵ_1 correlation increases to 0.2 in zone III when $\Delta\rho_m$ is +200 kg/m^3 (Fig. 5.7) and to 0.6 when +250kg/m^3 (Fig. 5.8). This suggests that a sufficiently large positive value of $\Delta\rho_m$ is needed for the sinking of the MI to generate significant flow consistent with the observed anisotropy in the time scale considered in our study. This idea is supported by other density modeling studies in the New Madrid seismic zone (e.g., Grana & Richardson 1996, Levandowski et al. 2016), which indicate the $\Delta\rho_m$ to be around +200kg/m^3. Sinking of the high-density MI would cause the radial deformation surrounding it (Fig. S1), which correlates relatively well with the anisotropy in zone III and zone IV.

The models with increasing viscosity of the lower crust do not show any apparent trend in the correlation with the observed anisotropy (Fig. 5.9). However, we observe a peak in the correlation of ϵ_1 when a viscosity of 10^{19}Pa·s is used but low correlation at values higher or lower than it. A possible explanation for this is that with this viscosity, the lower-crust is just weak enough to cause the appropriate deformation pattern from the sinking MI. Higher values of viscosity prohibit the sinking of the MI, while lower values promote sinking, resulting in ϵ_1 directions inconsistent with the anisotropy.

We modify our reference model to test the alignment of the SKS splitting results

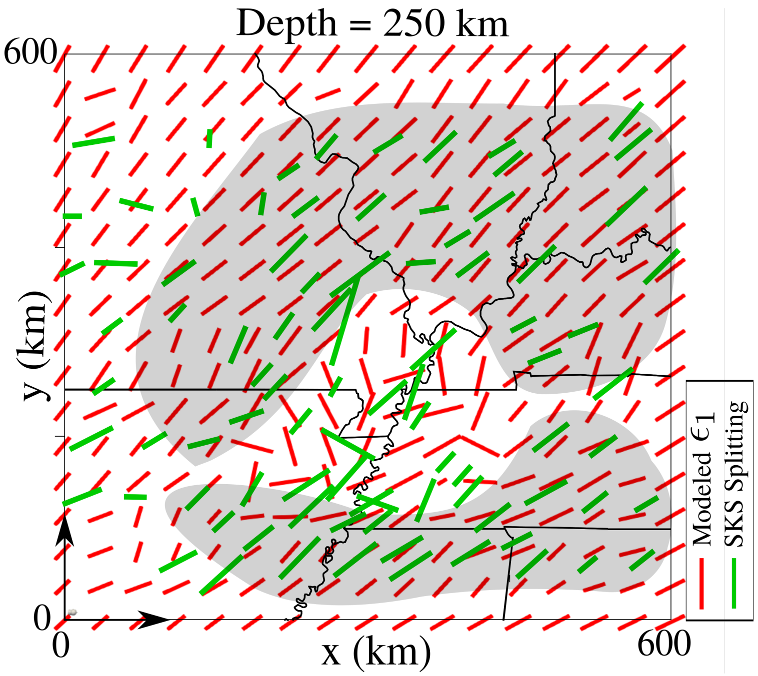

Fig. 5.10: SKS splitting results (green lines) by Nyamwandha & Powell (2016) and the modeled maximum finite strain (red lines) at depth 250 km in our study region. The gray areas shows good correspondence between the observed anisotropy and the model results. State lines are shown in black.

by Nyamwandha & Powell (2016) with the NE-SW oriented absolute plate motion (APM) direction. The modified model extends to a depth of 300 km, and contains a layer from 220 to 300 km with lower viscosity, 10^{20} Pa.s, to represent the asthenosphere. Since SKS ray-paths sample the deep portions of upper-mantle, which can be readily deformed, we only compare the finite-strain model output with the observed SKS splitting directions in Fig. 5.10. We choose the depth layer at 250 km as a proxy for the asthenospheric flow, as the expected thickness of the lithosphere beneath the continental interior is up to 250 km (O'Reilly & Griffin 2010). We then superimpose the APM using an additional NE-SW ϵ_1 direction on the model-predicted directions (Fig. 5.10). A clear correspondence can be seen in Fig. 5.10 in several areas between the SKS splitting results and the finite strain from our model. The locations of mismatch in the observed and the modeled results (Fig. 5.10) are mostly in the Mississippi Embayment and could be attributed to remnant lithospheric anisotropy developed during the past tectonic events (Thomas et al. 2006) or a more complex LVZ structure than the one we used in our model setup.

In summary, the reference numerical model presented in this study explains up to 25% of the observed spiral-shaped anisotropy assuming maximum finite strain as the appropriate anisotropy indicator. Modification of the reference model is made to test the isolated effects of the two anomalies, the mafic intrusion, and the low-velocity zone, as well as various densities of the mafic intrusion, and different viscosities of the lower crust. The model tests suggest that the anisotropy is primarily due to the deformation produced by the sinking of a dense mafic intrusion with a density contrast of at least $+200\text{kg/m}^3$ with the surrounding lower crust. Additionally, we also find that the lower crust is required to be weak, having approximate viscosity of $1\text{-}5 \times 10^{19}\text{Pa}\cdot\text{s}$, to approximately match the observed anisotropic pattern. We also verify that the mechanism of the SKS splitting beneath the Mississippi Embayment is due to the asthenospheric flow in response to the present-day plate motion.

Supplementary figure

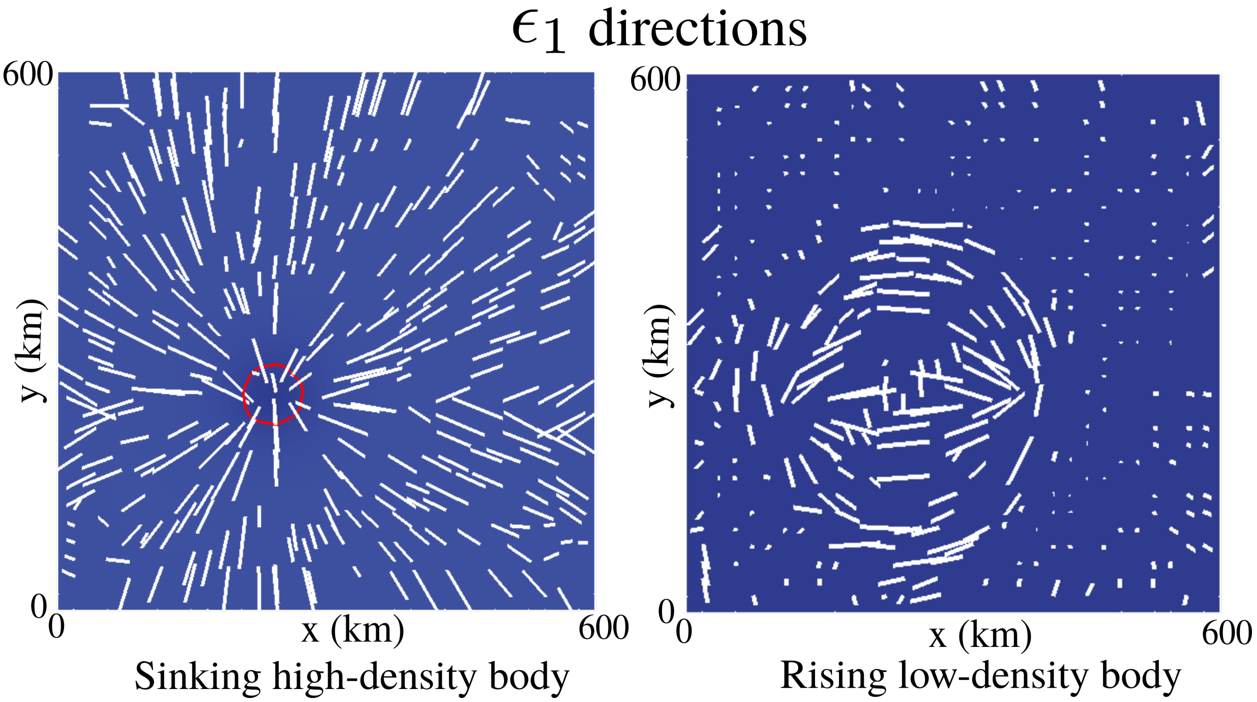

Fig. S1: The computed maximum finite strain directions (ϵ_1) for a simplified models from Fig. 5.4 having an idealized spherical high-density body with density contrast +200kg/m^3 (left), and a model with a semi-spherical low-density body with density contrast −100kg/m^3 (right). The white lines shows the direction of the ϵ_1 and the red contour in the left shows the contour marking the dense body

Chapter 6

Conclusions

This dissertation advances the general understanding of the Central and Eastern US (CEUS), and its associated seismicity using numerical modeling and receiver functions. The presented work focuses on the upper mantle beneath the CEUS. Particular attention is given to the Mississippi Embayment (ME) region that hosts the New Madrid Seismic Zone (NMSZ).

The results from this dissertation are illustrated in Fig. 6.1 and summarized in the subsequent paragraphs.

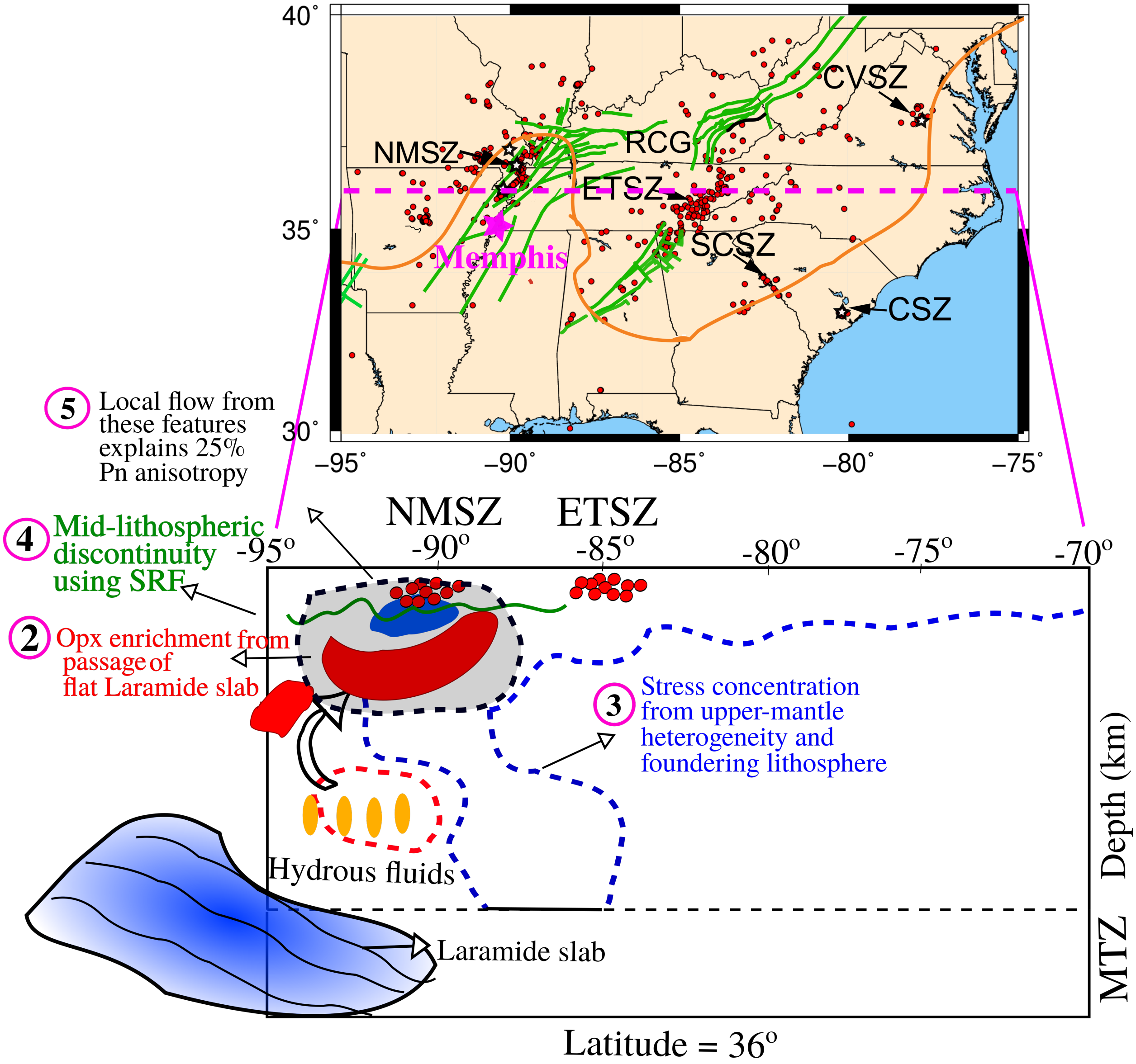

Fig. 6.1: A cartoon showing the conclusions from all the chapters along latitude 36°. Data analysis from Chapter 2 indicates that low-velocity anomaly in the upper mantle below the NMSZ could be explained by orthopyroxene (Opx) enrichment. It is proposed that increased Opx content occurs from the reaction of hydrous fluids rising from a stalled fragment of the Farallon slab. Numerical model results from Chapter 3 demonstrates that the upper-mantle heterogeneity promotes the preexisting faults to slip in the seismic zones of the Central and Eastern US. The S-wave receiver functions (SRF) study in Chapter 4 reveals a negative velocity lithospheric discontinuity around depths 60 to 100 km, interpreted as a mid-lithospheric discontinuity. Chapter 5 explores the origins of observed Pn anisotropy using numerical models incorporating the low-velocity zone and the mafic intrusion observed beneath the NMSZ.

Summary

Orthopyroxene enrichment beneath the NMSZ explains the upper mantle low-velocity zone beneath the NMSZ. Chapter 2 invokes orthopyroxene (Opx) enrichment below the NMSZ to explain the high and similar-magnitude negative Vs and Vp anomaly (-3 to -5%) observed by Nyamwandha et al. (2016) at 80 to 150 km depths. Other factors, such as increased water content and temperature perturbations, are also considered to explain the negative anomalies. However, due to the higher sensitivity of the S-wave velocity with temperature and water content compared to the P-wave velocity, these factors alone are not able to explain the observed anomalies. Increased Opx content (30 to 40%) that reduces the P-wave velocity more than the S-wave velocity, along with higher temperatures (up to 450 K), could simultaneously explain the observed negative velocity anomalies. A fragment of the Farallon slab has been observed stagnant at the mantle-transition depths in other tomography studies (e.g., Sigloch et al. 2008, Liu et al. 2008, Sigloch 2011) east of the NMSZ. Based on the results and the past studies, a model is proposed for the Opx enrichment: hydrous silica-rich fluids from the flat slab alter the composition of the asthenosphere beneath the NMSZ, leading to increased Opx contents.

The upper mantle heterogeneities beneath the CEUS increases stress in the seismic zones. In Chapter 2 and Chapter 3, arguments are presented that the upper-mantle heterogeneity observed in the recent tomography studies by Nyamwandha et al. (2016) and Biryol et al. (2016) increases the stress in the upper-crust of the seismic zones within the CEUS. Chapter 2 focuses on the NMSZ, in which visco-elastic 3D numerical models are set up for the ME region based on the tomography by Nyamwandha et al. (2016). Different models assume that the tomography is represented by equivalent water content, temperature perturbation, Opx content, or their combinations. The differential stress computations show stress increase in the upper crust of the NMSZ for all the possible causes, but the maximum increase is observed when the temperature is the only contributing factor to the velocity anomalies. Chapter 3 explores the stress effects at five seismic zones in the CEUS due to the upper-mantle heterogeneity, including a large positive P-wave velocity anomaly, interpreted as a foundering lithosphere, observed in the tomography study by Biryol et al. (2016). The 3-D tomography results are converted to temperature and density anomalies, which are used in the numerical models employing dislocation and diffusion creep. The crustal stresses generated from the mantle flow are considerably increased in the presence of the upper-mantle heterogeneity. Both differential stress and Coulomb stress for fault geometries—compiled from past studies on focal mechanisms and earthquake relocation—for each seismic zone, are used as the stress metrics. The models also show that the foundering lithosphere increases the stress at the nearby seismic zones, the Eastern Tennessee Seismic Zone, and the New Madrid Seismic Zone.

A new mid-lithospheric discontinuity has been found beneath the ME. Chapter 4 reveals a continuous negative velocity contrast at depths 60 to 100 km beneath the ME using S-wave receiver functions. The converted negative Sp phase is interpreted as a mid-lithospheric discontinuity after a comprehensive analysis using several published velocity models for the ME. A combination of compositional changes and temperature variations are suggested as the likely mechanism for the origin of the observed lithospheric discontinuity.

A high-density intrusive body in a weak lower crust can partly explain the enigmatic spiral pattern of seismic anisotropy beneath the NMSZ. Chapter 5 recommends a numerical model to explain the spiral-shaped Pn anisotropy directions observed by Basu & Powell (2019) at the NMSZ. The presence of two striking anomalies: a high-density sinking mafic intrusion and a low-velocity zone, in the NMSZ, is established by gathering past observational studies. A reference numerical model is setup to represent the study region with these anomalies. Maximum finite strain and maximum horizontal compressive stress directions are used as indicators for the observed anisotropy. Several modifications to the reference model are made to observe the effects of isolating each anomaly, by varying density contrasts of the mafic intrusion, and varying viscosity of the lower crust. A correlation of the model results with the observed anisotropy pattern indicates that a high-density contrast of the intrusion (+200 kg/m^3) and a weak lower crust (10^{19} Pa·s) could explain 25% of the anisotropic directions.

Scope

The presented work has shown the link between the instantaneous upper-mantle flow with the intraplate seismicity. However, time-dependent modeling of the CEUS that could lead to the present-day upper-mantle structure is not explored. Investigating time-dependent modeling can help us answer related research questions such as: what is the geodynamic mechanism for generating a large positive Vp anomaly observed by Biryol et al. (2016)?, whether that anomaly is an ongoing foundering lithosphere (Biryol et al. 2016) or a fragment of a subducted Farallon slab (Schmandt & Lin 2014)?, and how does the ascending hydrous fluids after the subduction of the stagnant slab interact with the asthenosphere, to give the observed tomography results in the NMSZ Nyamwandha et al. (2016)?. These questions can be answered by employing advanced numerical techniques such as backward advection modeling (e.g., Conrad & Gurnis 2003), quasi-reversibility (Glišović & Forte 2016), or adjoint methods (e.g., Liu et al. 2008) to get the initial conditions (density, viscosity) for the numerical model. Another interesting research question is to investigate how much of frozen-in strain from past tectonic events are stored in the upper-mantle, indicated in the observed Pn (Basu & Powell 2019) and SKS (Nyamwandha & Powell 2016) anisotropy results. This could be addressed by using the D-Rex method (Kaminski et al. 2004), which is capable of tracking the evolution of lattice-crystals.

REFERENCES

Aagaard, B. T., Knepley, M. G. & Williams, C. A. (2013), 'A domain decomposition approach to implementing fault slip in finite-element models of quasi-static and dynamic crustal deformation', *Journal of Geophysical Research: Solid Earth* **118**(6), 3059–3079.

Abt, D. L., Fischer, K. M., French, S. W., Ford, H. A., Yuan, H. & Romanowicz, B. (2010), 'North american lithospheric discontinuity structure imaged by ps and sp receiver functions', *Journal of Geophysical Research: Solid Earth* **115**(B9).

Aki, K. & Richards, P. (1980), 'Quantitative seismology, theory and methods, vol. 1 wh freeman & co', *New York* .

Alpert, L. A., Miller, M. S., Becker, T. W. & Allam, A. A. (2013), 'Structure beneath the alboran from geodynamic flow models and seismic anisotropy', *Journal of Geophysical Research: Solid Earth* **118**(8), 4265–4277.

Ammon, C. J., Randall, G. E. & Zandt, G. (1990), 'On the nonuniqueness of receiver function inversions', *Journal of Geophysical Research: Solid Earth* **95**(B10), 15303–15318.

Anderson, D. L. (1961), 'Elastic wave propagation in layered anisotropic media', *Journal of Geophysical Research* **66**(9), 2953–2963.

Anderson, O. L., Isaak, D. & Oda, H. (1992), 'High-temperature elastic constant data on minerals relevant to geophysics', *Reviews of Geophysics* **30**(1), 57–90.

Araragi, K. R., Savage, M. K., Ohminato, T. & Aoki, Y. (2015), 'Seismic anisotropy of the upper crust around mount fuji, japan', *Journal of Geophysical Research: Solid Earth* **120**(4), 2739–2751.

Arcay, D., Tric, E. & Doin, M.-P. (2007), 'Slab surface temperature in subduction zones: Influence of the interplate decoupling depth and upper plate thinning processes', *Earth and Planetary Science Letters* **255**(3-4), 324–338.

Artemieva, I. M., Billien, M., Lévêque, J.-J. & Mooney, W. D. (2004), 'Shear wave velocity, seismic attenuation, and thermal structure of the continental upper mantle', *Geophysical Journal International* **157**(2), 607–628.

Baird, A., McKinnon, S. & Godin, L. (2010), 'Relationship between structures, stress and seismicity in the charlevoix seismic zone revealed by 3-d geomechanical models: Implications for the seismotectonics of continental interiors', *Journal of Geophysical Research: Solid Earth* **115**(B11).

Bakun, W. H. & Hopper, M. G. (2004), 'Historical Seismic Activity in the Central United States', *Seismological Research Letters* **75**(5), 564–574.

Bangerth, W., Dannberg, J., Gassmoeller, R., Heister, T. et al. (2018), 'ASPECT v2.0.0 [software]'.

Basu, U. & Powell, C. (2019), 'Pn tomography and anisotropy study of the central united states', *Journal of Geophysical Research: Solid Earth* **124**(7), 7105–7119.

Becker, T. W., Browaeys, J. T. & Jordan, T. H. (2007), 'Stochastic analysis of shear-wave splitting length scales', *Earth and Planetary Science Letters* **259**(3-4), 526–540.

Becker, T. W., Chevrot, S., Schulte-Pelkum, V. & Blackman, D. K. (2006), 'Statistical properties of seismic anisotropy predicted by upper mantle geodynamic models', *Journal of Geophysical Research: Solid Earth* **111**(B8).

Becker, T. W., Faccenna, C., Humphreys, E. D., Lowry, A. R. & Miller, M. S. (2014), 'Static and dynamic support of western united states topography', *Earth and Planetary Science Letters* **402**, 234–246.

Becker, T. W., Kellogg, J. B., Ekström, G. & OConnell, R. J. (2003), 'Comparison of azimuthal seismic anisotropy from surface waves and finite strain from global mantle-circulation models', *Geophysical Journal International* **155**(2), 696–714.

Bell, D. R., Grégoire, M., Grove, T. L., Chatterjee, N., Carlson, R. W. & Buseck, P. R. (2005), 'Silica and volatile-element metasomatism of Archean mantle: a xenolith-scale example from the Kaapvaal Craton', *Contributions to Mineralogy and Petrology* **150**(3), 251–267.

Billen, M. I. & Hirth, G. (2007), 'Rheologic controls on slab dynamics', *Geochemistry, Geophysics, Geosystems* **8**(8).

Biryol, C. B., Wagner, L. S., Fischer, K. M. & Hawman, R. B. (2016), 'Relationship between observed upper mantle structures and recent tectonic activity across the southeastern united states', *Journal of Geophysical Research: Solid Earth* **121**(5), 3393–3414.

Blackwell, D. D., Negraru, P. T. & Richards, M. C. (2006), 'Assessment of the enhanced geothermal system resource base of the united states', *Natural Resources Research* **15**(4), 283–308.

Bollinger, G. & Sibol, M. (1985), 'Seismicity, seismic reflection studies, gravity and geology of the central virginia seismic zone: Part i. seismicity', *Geological Society of America Bulletin* **96**(1), 49–57.

Boness, N. L. & Zoback, M. D. (2006), 'Mapping stress and structurally controlled crustal shear velocity anisotropy in california', *Geology* **34**(10), 825–828.

Bonnardot, M.-A., Hassani, R. & Tric, E. (2008), 'Numerical modelling of lithosphere–asthenosphere interaction in a subduction zone', *Earth and Planetary Science Letters* **272**(3-4), 698–708.

Boyd, O. S. & Cramer, C. H. (2014), 'Estimating earthquake magnitudes from reported intensities in the central and eastern united states', *Bulletin of the Seismological Society of America* **104**(4), 1709–1722.

Boyd, O. S., Smalley, R. & Zeng, Y. (2015), ‘Crustal deformation in the new madrid seismic zone and the role of postseismic processes’, *Journal of Geophysical Research: Solid Earth* **120**(8), 5782–5803.

Braile, L., Keller, G., Hinze, W. & Lidiak, E. (1982), ‘An ancient rift complex and its relation to contemporary seismicity in the new madrid seismic zone’, *Tectonics* **1**(2), 225–237.

Brantley, S. L., Evans, B., Hickman, S. H. & Crerar, D. A. (1990), ‘Healing of microcracks in quartz: Implications for fluid flow’, *Geology* **18**(2), 136–139.

Bunge, H.-P., Hagelberg, C. & Travis, B. (2003), ‘Mantle circulation models with variational data assimilation: inferring past mantle flow and structure from plate motion histories and seismic tomography’, *Geophysical Journal International* **152**(2), 280–301.

Burov, E. (2010), ‘The equivalent elastic thickness (Te) seismicity and the long-term rheology of continental lithosphere: Time to burn-out “crème brûlée”?’, *Tectonophysics* **484**(1-4), 4–26.

Calais, E., Freed, A., Van Arsdale, R. & Stein, S. (2010), ‘Triggering of new madrid seismicity by late-pleistocene erosion’, *Nature* **466**(7306), 608–611.

Calais, E., Han, J. Y., DeMets, C. & Nocquet, J. M. (2006), ‘Deformation of the North American plate interior from a decade of continuous GPS measurements’, *Journal of Geophysical Research: Solid Earth* **111**(B6).

Cammarano, F., Goes, S., Vacher, P. & Giardini, D. (2003), ‘Inferring upper-mantle temperatures from seismic velocities’, *Physics of the Earth and Planetary Interiors* **138**(3-4), 197–222.

Catchings, R. (1999), ‘Regional vp, vs, vp/vs, and poisson’s ratios across earthquake source zones from memphis, tennessee, to st. louis, missouri', *Bulletin of the Seismological Society of America* **89**(6), 1591–1605.

Chapman, M., Beale, J. N., Hardy, A. C. & Wu, Q. (2016), 'Modern seismicity and the fault responsible for the 1886 charleston, south carolina, earthquake', *Bulletin of the Seismological Society of America* **106**(2), 364–372.

Chapman, M., Powell, C., Vlahovic, G. & Sibol, M. (1997), 'A statistical analysis of earthquake focal mechanisms and epicenter locations in the eastern tennessee seismic zone', *Bulletin of the Seismological Society of America* **87**(6), 1522–1536.

Chen, C., Gilbert, H., Andronicos, C., Hamburger, M. W., Larson, T., Marshak, S., Pavlis, G. L. & Yang, X. (2016), 'Shear velocity structure beneath the central united states: implications for the origin of the illinois basin and intraplate seismicity', *Geochemistry, Geophysics, Geosystems* **17**(3), 1020–1041.

Chen, C., Gilbert, H., Fischer, K. M., Andronicos, C. L., Pavlis, G. L., Hamburger, M. W., Marshak, S., Larson, T. & Yang, X. (2018), 'Lithospheric discontinuities beneath the us midcontinent–signatures of proterozoic terrane accretion and failed rifting', *Earth and Planetary Science Letters* **481**, 223–235.

Chen, C., Zhao, D. & Wu, S. (2014), 'Crust and upper mantle structure of the new madrid seismic zone: Insight into intraplate earthquakes', *Physics of the Earth and Planetary Interiors* **230**, 1–14.

Chiu, J., Johnston, A. & Yang, Y. (1992), 'Imaging the active faults of the central new madrid seismic zone using panda array data', *Seismological Research Letters* **63**(3), 375–393.

Clayton, R. W. & Wiggins, R. A. (1976), 'Source shape estimation and deconvolution of teleseismic bodywaves', *Geophysical Journal International* **47**(1), 151–177.

Connolly, J. & Kerrick, D. (2002), ‘Metamorphic controls on seismic velocity of subducted oceanic crust at 100–250 km depth’, *Earth and Planetary Science Letters* **204**(1-2), 61–74.

Conrad, C. P., Behn, M. D. & Silver, P. G. (2007), ‘Global mantle flow and the development of seismic anisotropy: Differences between the oceanic and continental upper mantle’, *Journal of Geophysical Research: Solid Earth* **112**(B7).

Conrad, C. P. & Gurnis, M. (2003), ‘Seismic tomography, surface uplift, and the breakup of gondwanaland: Integrating mantle convection backwards in time’, *Geochemistry, Geophysics, Geosystems* **4**(3).

Cooley, M. (2015), ‘A new set of focal mechanisms and a geodynamic model for the eastern tennessee seismic zone (ms thesis).’, *The University of Memphis, Memphis, Tennessee* pp. 1–46.

Cottaar, S., Heister, T., Rose, I. & Unterborn, C. (2014), ‘Burnman: A lower mantle mineral physics toolkit’, *Geochemistry, Geophysics, Geosystems* **15**(4), 1164–1179.

Cox, R. T. & Van Arsdale, R. B. (1997), ‘Hotspot origin of the mississippi embayment and its possible impact on contemporary seismicity’, *Engineering Geology* **46**(3-4), 201–216.

Cox, R. T. & Van Arsdale, R. B. (2002), ‘The mississippi embayment, north america: A first order continental structure generated by the cretaceous superplume mantle event’, *Journal of Geodynamics* **34**(2), 163–176.

Crampin, S., Evans, R. & Atkinson, B. K. (1984), ‘Earthquake prediction: a new physical basis’, *Geophysical Journal International* **76**(1), 147–156.

Crampin, S. & Peacock, S. (2008), ‘A review of the current understanding of seismic shear-wave splitting in the earths crust and common fallacies in interpretation’, *Wave Motion* **45**(6), 675–722.

Davies, J. H. (2013), ‘Global map of solid earth surface heat flow’, *Geochemistry, Geophysics, Geosystems* **14**(10), 4608–4622.

Delvaux, D., Moeys, R., Stapel, G., Petit, C., Levi, K., Miroshnichenko, A., Ruzhich, V. & Sankov, V. (1997), ‘Paleostress reconstructions and geodynamics of the baikal region, central asia, part 2. cenozoic rifting’, *Tectonophysics* **282**(1-4), 1–38.

Dixon, J. E., Dixon, T., Bell, D. & Malservisi, R. (2004), ‘Lateral variation in upper mantle viscosity: role of water’, *Earth and Planetary Science Letters* **222**(2), 451–467.

Dueker, K. G. & Sheehan, A. F. (1998), ‘Mantle discontinuity structure beneath the colorado rocky mountains and high plains’, *Journal of Geophysical Research: Solid Earth* **103**(B4), 7153–7169.

Duffy, T. S. & Anderson, D. L. (1989), ‘Seismic velocities in mantle minerals and the mineralogy of the upper mantle’, *Journal of Geophysical Research: Solid Earth* **94**(B2), 1895–1912.

Dziewonski, A. M. & Anderson, D. L. (1981), ‘Preliminary reference earth model’, *Physics of the earth and planetary interiors* **25**(4), 297–356.

Eaton, D. W., Darbyshire, F., Evans, R. L., Grütter, H., Jones, A. G. & Yuan, X. (2009), ‘The elusive lithosphere–asthenosphere boundary (lab) beneath cratons’, *Lithos* **109**(1-2), 1–22.

Efron, B. & Tibshirani, R. (1986), ‘Bootstrap methods for standard errors, confidence intervals, and other measures of statistical accuracy’, *Statistical science* pp. 54–75.

English, J. M. & Johnston, S. T. (2004), ‘The Laramide Orogeny: What Were the Driving Forces?’, *International Geology Review* **46**(9), 833–838.

Farra, V. & Vinnik, L. (2000), ‘Upper mantle stratification by p and s receiver functions’, *Geophysical Journal International* **141**(3), 699–712.

Forte, A., Mitrovica, J., Moucha, R., Simmons, N. & Grand, S. (2007), 'Descent of the ancient farallon slab drives localized mantle flow below the new madrid seismic zone', *Geophysical Research Letters* **34**(4).

Freed, A. M. (2005), 'Earthquake triggering by static, dynamic, and postseismic stress transfer', *Annu. Rev. Earth Planet. Sci.* **33**, 335–367.

Gallen, S. F. & Thigpen, J. R. (2018), 'Lithologic controls on focused erosion and intraplate earthquakes in the eastern tennessee seismic zone', *Geophysical Research Letters* **45**(18), 9569–9578.

Gangopadhyay, A., Dickerson, J. & Talwani, P. (2004), 'A two-dimensional numerical model for current seismicity in the new madrid seismic zone', *Seismological Research Letters* **75**(3), 406–418.

Gangopadhyay, A. & Talwani, P. (2005), 'Fault intersections and intraplate seismicity in charleston, south carolina: Insights from a 2-d numerical model', *Current Science* pp. 1609–1616.

Gao, S. S. & Liu, K. H. (2014), 'Mantle transition zone discontinuities beneath the contiguous United States', *Journal of Geophysical Research: Solid Earth* **119**(8), 6452–6468.

Geng, Y., Powell, C. & Saxena, A. (in-prep), 'Joint local and teleseismic tomography in the central united states and implications for the origin of intraplate seismicity'.

Ghosh, A., Holt, W. E. & Bahadori, A. (2019), 'Role of large-scale tectonic forces in intraplate earthquakes of central and eastern north america', *Geochemistry, Geophysics, Geosystems* .

Gilbert, H. J., Sheehan, A. F., Dueker, K. G. & Molnar, P. (2003), 'Receiver functions in the western united states, with implications for upper mantle structure and dynamics', *Journal of Geophysical Research: Solid Earth* **108**(B5).

Glišović, P. & Forte, A. M. (2016), 'A new back-and-forth iterative method for time-reversed convection modeling: Implications for the cenozoic evolution of 3-d structure and dynamics of the mantle', *Journal of Geophysical Research: Solid Earth* **121**(6), 4067–4084.

Goes, S., Govers, R. & Vacher, P. (2000), 'Shallow mantle temperatures under Europe fromPandSwave tomography', *Journal of Geophysical Research: Solid Earth* **105**(B5), 11153–11169.

Goes, S. & van der Lee, S. (2002), 'Thermal structure of the north american uppermost mantle inferred from seismic tomography', *Journal of Geophysical Research: Solid Earth* **107**(B3), ETG–2.

Gordon, R. B. (1967), 'Thermally activated processes in the earth: Creep and seismic attenuation', *Geophysical Journal International* **14**(1-4), 33–43.

Grana, J. P. & Richardson, R. M. (1996), 'Tectonic stress within the new madrid seismic zone', *Journal of Geophysical Research: Solid Earth* **101**(B3), 5445–5458.

Gripp, A. E. & Gordon, R. G. (2002), 'Young tracks of hotspots and current plate velocities', *Geophysical Journal International* **150**(2), 321–361.

Grollimund, B. & Zoback, M. D. (2001), 'Did deglaciation trigger intraplate seismicity in the new madrid seismic zone?', *geology* **29**(2), 175–178.

Haggerty, S. E. (1995), 'Upper mantle mineralogy', *Journal of Geodynamics* **20**(4), 331–364.

Hammond, W. C. & Humphreys, E. D. (2000), 'Upper mantle seismic wave velocity: Effects of realistic partial melt geometries', *Journal of Geophysical Research: Solid Earth* **105**(B5), 10975–10986.

Hansen, L. N. & Warren, J. M. (2015), 'Quantifying the effect of pyroxene on deformation of peridotite in a natural shear zone', *Journal of Geophysical Research: Solid Earth* **120**(4), 2717–2738.

Hansen, S. M., Dueker, K. & Schmandt, B. (2015), 'Thermal classification of lithospheric discontinuities beneath usarray', *Earth and Planetary Science Letters* **431**, 36–47.

Haskell, N. A. (1962), 'Crustal reflection of plane p and sv waves', *Journal of Geophysical Research* **67**(12), 4751–4768.

Heister, T., Dannberg, J., Gassmöller, R. & Bangerth, W. (2017), 'High accuracy mantle convection simulation through modern numerical methods. II: Realistic models and problems', *Geophysical Journal International* **210**(2), 833–851.

Herrmann, R., Ammon, C. & Julia, J. (2000), Joint inversion of receiver functions and surface-wave dispersion for crustal structure, Technical report, SAINT LOUIS UNIV MO DEPT OF EARTH AND ATMOSPHERIC SCIENCES.

Hess, H. (1964), 'Seismic anisotropy of the uppermost mantle under oceans', *Nature* **203**(4945), 629–631.

Hildenbrand, T. G. (1985), 'Rift structure of the northern mississippi embayment from the analysis of gravity and magnetic data', *Journal of Geophysical Research: Solid Earth* **90**(B14), 12607–12622.

Hildenbrand, T., Kane, M. F. & Stauder, W. (1977), Magnetic and gravity anomalies in the northern mississippi embayment and their spacial relation to seismicity, Technical report.

Hildenbrand, T., Stuart, W. & Talwani, P. (2001), 'Geologic structures related to new madrid earthquakes near memphis, tennessee, based on gravity and magnetic interpretations', *Engineering Geology* **62**(1-3), 105–121.

Hirth, G. & Kohlstedt, D. (2003), Rheology of the upper mantle and the mantle wedge: A view from the experimentalists, *in* 'Inside the Subduction Factory', American Geophysical Union, pp. 83–105.

Hoffman, P. F., Bally, A., Palmer, A. et al. (1989), 'Precambrian geology and tectonic history of north america', *The geology of North Americaan overview* pp. 447–512.

Hopper, E. & Fischer, K. M. (2015), 'The meaning of midlithospheric discontinuities: A case study in the northern us craton', *Geochemistry, Geophysics, Geosystems* **16**(12), 4057–4083.

Hopper, E., Ford, H. A., Fischer, K. M., Lekic, V. & Fouch, M. J. (2014), 'The lithosphere–asthenosphere boundary and the tectonic and magmatic history of the northwestern united states', *Earth and Planetary Science Letters* **402**, 69–81.

Hough, S. E. (2012), 'Initial assessment of the intensity distribution of the 2011 mw 5.8 mineral, virginia, earthquake', *Seismological Research Letters* **83**(4), 649–657.

Huang, J. & Zhao, D. (2006), 'High-resolution mantle tomography of China and surrounding regions', *Journal of Geophysical Research* **111**(B9).

Huang, Z. & Zhao, D. (2013), 'Mapping p-wave azimuthal anisotropy in the crust and upper mantle beneath the united states', *Physics of the Earth and Planetary Interiors* **225**, 28–40.

Humphreys, E. (2009), 'Relation of flat subduction to magmatism and deformation in the western United States', *Geological Society of America Memoirs* **204**(0), 85–98.

Hurd, O. & Zoback, M. D. (2012), 'Intraplate earthquakes, regional stress and fault mechanics in the central and eastern us and southeastern canada', *Tectonophysics* **581**, 182–192.

Ito, T. & Simons, M. (2011), 'Probing asthenospheric density, temperature, and elastic moduli below the western united states', *Science* **332**(6032), 947–951.

Ji, S., Wang, Z. & Wirth, R. (2001), 'Bulk flow strength of forsterite–enstatite composites as a function of forsterite content', *Tectonophysics* **341**(1-4), 69–93.

Johnson, G. A., Horton, S. P., Withers, M. & Cox, R. (2014), 'Earthquake focal mechanisms in the new madrid seismic zone', *Seismological Research Letters* **85**(2), 257–267.

Johnston, A. C. (1996), 'Seismic moment assessment of earthquakes in stable continental regionsiii. new madrid 1811–1812, charleston 1886 and lisbon 1755', *Geophysical Journal International* **126**(2), 314–344.

Kaminski, E., Ribe, N. M. & Browaeys, J. T. (2004), 'D-rex, a program for calculation of seismic anisotropy due to crystal lattice preferred orientation in the convective upper mantle', *Geophysical Journal International* **158**(2), 744–752.

Kaneshima, S. (1990), 'Origin of crustal anisotropy: shear wave splitting studies in japan', *Journal of Geophysical Research: Solid Earth* **95**(B7), 11121–11133.

Karato, S. (1984), 'Grain-size distribution and rheology of the upper mantle', *Tectonophysics* **104**(1-2), 155–176.

Karato, S. (1993), 'Importance of anelasticity in the interpretation of seismic tomography', *Geophysical Research Letters* **20**(15), 1623–1626.

Karato, S. (2003), Mapping water content in the upper mantle, *in* 'Inside the Subduction Factory', American Geophysical Union, pp. 135–152.

Karato, S.-i., Olugboji, T. & Park, J. (2015), 'Mechanisms and geologic significance of the mid-lithosphere discontinuity in the continents', *Nature geoscience* **8**(7), 509–514.

Karato, S. & Jung, H. (1998), 'Water partial melting and the origin of the seismic low velocity and high attenuation zone in the upper mantle', *Earth and Planetary Science Letters* **157**(3-4), 193–207.

Karato, S. & Wu, P. (1993), 'Rheology of the upper mantle: A synthesis', *Science* **260**(5109), 771–778.

Katsura, T., Yoneda, A., Yamazaki, D., Yoshino, T. & Ito, E. (2010), 'Adiabatic temperature profile in the mantle', *Physics of the Earth and Planetary Interiors* **183**(1-2), 212–218.

Katz, R. F., Spiegelman, M. & Langmuir, C. H. (2003), 'A new parameterization of hydrous mantle melting', *Geochemistry, Geophysics, Geosystems* **4**(9).

Keller, G., Lidiak, E., Hinze, W. & Braile, L. (1983), The role of rifting in the tectonic development of the midcontinent, usa, *in* 'Developments in Geotectonics', Vol. 19, Elsevier, pp. 391–412.

Kenner, S. J. & Segall, P. (2000), 'A mechanical model for intraplate earthquakes: Application to the new madrid seismic zone', *Science* **289**(5488), 2329–2332.

Kennett, B. & Engdahl, E. (1991), 'Traveltimes for global earthquake location and phase identification', *Geophysical Journal International* **105**(2), 429–465.

King, G. C., Stein, R. S. & Lin, J. (1994), 'Static stress changes and the triggering of earthquakes', *Bulletin of the Seismological Society of America* **84**(3), 935–953.

Kirby, S. H. & Kronenberg, A. K. (1987), 'Rheology of the lithosphere: Selected topics', *Reviews of Geophysics* **25**(6), 1219.

Kronbichler, M., Heister, T. & Bangerth, W. (2012), 'High accuracy mantle convection simulation through modern numerical methods', *Geophysical Journal International* **191**, 12–29.

Kusky, T. M., Windley, B. F., Wang, L., Wang, Z., Li, X. & Zhu, P. (2014), 'Flat slab subduction trench suction, and craton destruction: Comparison of the North China, Wyoming, and Brazilian cratons', *Tectonophysics* **630**, 208–221.

Langston, C. A. (1977), 'Corvallis, oregon, crustal and upper mantle receiver structure from teleseismic p and s waves', *Bulletin of the Seismological Society of America* **67**(3), 713–724.

Langston, C. A. (1979), 'Structure under mount rainier, washington, inferred from teleseismic body waves', *Journal of Geophysical Research: Solid Earth* **84**(B9), 4749–4762.

Langston, C. A. (1994), 'An integrated study of crustal structure and regional wave propagation for southeastern missouri', *Bulletin of the Seismological Society of America* **84**(1), 105–118.

Langston, C. A. & Hammer, J. K. (2001), 'The vertical component p-wave receiver function', *Bulletin of the Seismological Society of America* **91**(6), 1805–1819.

Laske, G., Masters, G., Ma, Z. & Pasyanos, M. (2013), Update on crust1.0 a 1-degree global model of earths crust, *in* 'Geophys. Res. Abstr', Vol. 15, EGU General Assembly Vienna, Austria, p. 2658.

Lay, T., Williams, Q., Garnero, E. J., Kellogg, L. & Wysession, M. E. (1998), 'Seismic wave anisotropy in the d region and its implications', *The core mantle boundary region* **28**, 299–318.

Le Pourhiet, L., Gurnis, M. & Saleeby, J. (2006), 'Mantle instability beneath the sierra nevada mountains in california and death valley extension', *Earth and Planetary Science Letters* **251**(1-2), 104–119.

Lee, C.-T. A. (2003), 'Compositional variation of density and seismic velocities in natural peridotites at stp conditions: Implications for seismic imaging of compositional heterogeneities in the upper mantle', *Journal of Geophysical Research: Solid Earth* **108**(B9).

Lekic, V., Cottaar, S., Dziewonski, A. & Romanowicz, B. (2012), 'Cluster analysis of global lower mantle tomography: A new class of structure and implications for chemical heterogeneity', *Earth and Planetary Science Letters* **357**, 68–77.

Lekić, V. & Fischer, K. M. (2014), 'Contrasting lithospheric signatures across the western united states revealed by sp receiver functions', *Earth and Planetary Science Letters* **402**, 90–98.

Lekic, V. & Romanowicz, B. (2011), 'Tectonic regionalization without a priori information: A cluster analysis of upper mantle tomography', *Earth and Planetary Science Letters* **308**(1-2), 151–160.

Levandowski, W., Boyd, O. S., Briggs, R. W. & Gold, R. D. (2015), 'A random-walk algorithm for modeling lithospheric density and the role of body forces in the evolution of the m idcontinent rift', *Geochemistry, Geophysics, Geosystems* **16**(12), 4084–4107.

Levandowski, W., Boyd, O. S. & Ramirez-Guzmán, L. (2016), 'Dense lower crust elevates long-term earthquake rates in the new madrid seismic zone', *Geophysical Research Letters* **43**(16), 8499–8510.

Levandowski, W., Herrmann, R. B., Briggs, R., Boyd, O. & Gold, R. (2018), 'An updated stress map of the continental united states reveals heterogeneous intraplate stress', *Nature Geoscience* **11**(6), 433.

Li, Q., Liu, M., Zhang, Q. & Sandvol, E. (2007), 'Stress evolution and seismicity in the central-eastern united states: Insights from geodynamic modeling', *Special Papers-Geological Society of America* **425**, 149.

Li, Z.-H., Di Leo, J. F. & Ribe, N. M. (2014), 'Subduction-induced mantle flow, finite strain, and seismic anisotropy: Numerical modeling', *Journal of Geophysical Research: Solid Earth* **119**(6), 5052–5076.

Li, Z.-X. A., Lee, C.-T. A., Peslier, A. H., Lenardic, A. & Mackwell, S. J. (2008), 'Water contents in mantle xenoliths from the Colorado Plateau and vicinity: Implications for the mantle rheology and hydration-induced thinning of continental lithosphere', *Journal of Geophysical Research* **113**(B9).

Liu, L. & Gao, S. S. (2018), 'Lithospheric layering beneath the contiguous united states constrained by s-to-p receiver functions', *Earth and Planetary Science Letters* **495**, 79–86.

Liu, L., Gurnis, M., Seton, M., Saleeby, J., Mller, R. D. & Jackson, J. M. (2010), 'The role of oceanic plateau subduction in the Laramide orogeny', *Nature Geoscience* **3**(5), 353–357.

Liu, L., Spasojević, S. & Gurnis, M. (2008), 'Reconstructing farallon plate subduction beneath north america back to the late cretaceous', *Science* **322**(5903), 934–938.

Liu, L. & Zoback, M. D. (1997), 'Lithospheric strength and intraplate seismicity in the new madrid seismic zone', *Tectonics* **16**(4), 585–595.

Llenos, A. L. & Michael, A. J. (2013), 'Modeling earthquake rate changes in oklahoma and arkansas: Possible signatures of induced seismicity', *Bulletin of the Seismological Society of America* **103**(5), 2850–2861.

Madabhushi, S. & Talwani, P. (1993), 'Fault plane solutions and relocations of recent earthquakes in middleton place summerville seismic zone near charleston, south carolina', *Bulletin of the Seismological Society of America* **83**(5), 1442–1466.

Mainprice, D., Barruol, G. & Ismail, W. B. (2000), 'The seismic anisotropy of the earth's mantle: from single crystal to polycrystal', *Geophysical monograph-American Geophysical Union* **117**, 237–264.

Marshak, S. & Paulsen, T. (1996), 'Midcontinent U.S. fault and fold zones: A legacy of Proterozoic intracratonic extensional tectonism?', *Geology* **24**(2), 151.

Maruyama, S. & Okamoto, K. (2007), 'Water transportation from the subducting slab into the mantle transition zone', *Gondwana Research* **11**(1-2), 148–165.

Mazzotti, S. & Townend, J. (2010), 'State of stress in central and eastern north american seismic zones', *Lithosphere* **2**(2), 76–83.

McDonnell, R. D., Peach, C. J., van Roermund, H. L. M. & Spiers, C. J. (2000), 'Effect of varying enstatite content on the deformation behavior of fine-grained synthetic peridotite under wet conditions', *Journal of Geophysical Research: Solid Earth* **105**(B6), 13535–13553.

McDonough, W. F. & Rudnick, R. L. (1998), 'Mineralogy and composition of the upper mantle', *Reviews in mineralogy* **37**, 139–164.

McKenzie, D. (1979), 'Finite deformation during fluid flow', *Geophysical Journal International* **58**(3), 689–715.

Meade, C., Silver, P. G. & Kaneshima, S. (1995), 'Laboratory and seismological observations of lower mantle isotropy', *Geophysical Research Letters* **22**(10), 1293–1296.

Minster, J. B. & Anderson, D. L. (1981), 'A model of dislocation-controlled rheology for the mantle', *Philosophical Transactions of the Royal Society of London. Series A, Mathematical and Physical Sciences* **299**(1449), 319–356.

Montagner, J.-P. (1998), 'Where can seismic anisotropy be detected in the earths mantle? in boundary layers...', *Pure and Applied Geophysics* **151**(2-4), 223–256.

Mooney, W., Andrews, M., Ginzburg, A., Peters, D. & Hamilton, R. (1983), Crustal Structure of the Northern Mississippi Embayment and a Comparison with other Continental Rift Zones, *in* ‘Processes of Continental Rifting’, Elsevier, pp. 327–348.

Munsey, J. W. & Bollinger, G. (1985), ‘Focal mechanism analyses for virginia earthquakes (1978-1984)’, *Bulletin of the Seismological Society of America* **75**(6), 1613–1636.

Nicolas, A. & Christensen, N. I. (1987), ‘Formation of anisotropy in upper mantle peridotites-a review’, *Composition, structure and dynamics of the lithosphere-asthenosphere system* **16**, 111–123.

Nuttli, O. W. (1973), ‘The mississippi valley earthquakes of 1811 and 1812: Intesities, ground motion and magnitudes’, *Bulletin of the Seismological Society of America* **63**(1), 227–248.

Nyamwandha, C. A. & Powell, C. A. (2016), ‘Seismic anisotropy beneath the mississippi embayment and the new madrid seismic zone: A study of shear wave splitting’, *Journal of Geophysical Research: Solid Earth* **121**(11), 8239–8253.

Nyamwandha, C. A., Powell, C. A. & Langston, C. A. (2016), ‘A joint local and teleseismic tomography study of the mississippi embayment and new madrid seismic zone’, *Journal of Geophysical Research: Solid Earth* **121**(5), 3570–3585.

O’Reilly, S. Y. & Griffin, W. L. (2010), ‘The continental lithosphere–asthenosphere boundary: can we sample it?’, *Lithos* **120**(1-2), 1–13.

Pasyanos, M. E., Masters, T. G., Laske, G. & Ma, Z. (2014), ‘Litho1. 0: An updated crust and lithospheric model of the earth’, *Journal of Geophysical Research: Solid Earth* **119**(3), 2153–2173.

Pollitz, F. F., Kellogg, L. & Brgmann, R. (2001), ‘Sinking mafic body in a reactivated lower crust: a mechanism for stress concentration at the new madrid seismic zone', *Bulletin of the Seismological Society of America* **91**(6), 1882–1897.

Pollitz, F. F. & Mooney, W. D. (2014), 'Seismic structure of the central us crust and shallow upper mantle: Uniqueness of the reelfoot rift', *Earth and Planetary Science Letters* **402**, 157–166.

Pollitz, F. F. & Mooney, W. D. (2016), 'Seismic velocity structure of the crust and shallow mantle of the central and eastern united states by seismic surface wave imaging', *Geophysical Research Letters* **43**(1), 118–126.

Porritt, R. W., Allen, R. M. & Pollitz, F. F. (2014), 'Seismic imaging east of the Rocky Mountains with USArray', *Earth and Planetary Science Letters* **402**, 16–25.

Powell, C. A., Bollinger, G., Chapman, M. C., Sibol, M. S., Johnston, A. C. & Wheeler, R. L. (1994), 'A seismotectonic model for the 300-kilometer-long eastern tennessee seismic zone', *Science* **264**(5159), 686–688.

Powell, C. A. & Thomas, W. A. (2016), 'Grenville basement structure associated with the eastern tennessee seismic zone, southeastern usa', *Geology* **44**(1), 39–42.

Pujol, J., Johnston, A., Chiu, J.-M. & Yang, Y.-T. (1997), 'Refinement of thrust faulting models for the Central New Madrid seismic zone', *Engineering Geology* **46**(3-4), 281–298.

Quinquis, M. E., Buiter, S. J. & Ellis, S. (2011), 'The role of boundary conditions in numerical models of subduction zone dynamics', *Tectonophysics* **497**(1-4), 57–70.

Ribe, N. M. (1992), 'On the relation between seismic anisotropy and finite strain', *Journal of Geophysical Research: Solid Earth* **97**(B6), 8737–8747.

Rudnick, R. L., McDonough, W. F. & O'Connell, R. J. (1998), 'Thermal structure, thickness and composition of continental lithosphere', *Chemical Geology* **145**(3-4), 395–411.

Rychert, C. A. & Shearer, P. M. (2009), ‘A global view of the lithosphere-asthenosphere boundary’, *Science* **324**(5926), 495–498.

Rydelek, P. A. & Pollitz, F. F. (1994), ‘Fossil strain from the 1811–1812 new madrid earthquakes’, *Geophysical research letters* **21**(21), 2303–2306.

Santosh, M., Zhao, D. & Kusky, T. (2010), ‘Mantle dynamics of the Paleoproterozoic North China Craton: A perspective based on seismic tomography’, *Journal of Geodynamics* **49**(1), 39–53.

Saxena, S. K. & Shen, G. (1992), ‘Assessed data on heat capacity, thermal expansion, and compressibility for some oxides and silicates’, *Journal of Geophysical Research: Solid Earth* **97**(B13), 19813–19825.

Schmandt, B. & Humphreys, E. (2010), ‘Seismic heterogeneity and small-scale convection in the southern california upper mantle’, *Geochemistry, Geophysics, Geosystems* **11**(5).

Schmandt, B. & Lin, F.-C. (2014), ‘P and S wave tomography of the mantle beneath the United States’, *Geophysical Research Letters* **41**(18), 6342–6349.

Schutt, D. L. & Lesher, C. E. (2006), ‘Effects of melt depletion on the density and seismic velocity of garnet and spinel lherzolite’, *Journal of Geophysical Research: Solid Earth* **111**(B5).

Schutt, D. L. & Lesher, C. E. (2010), ‘Compositional trends among Kaapvaal Craton garnet peridotite xenoliths and their effects on seismic velocity and density’, *Earth and Planetary Science Letters* **300**(3-4), 367–373.

Shumway, A. M. (2008), ‘Focal mechanisms in the northeast new madrid seismic zone’, *Seismological Research Letters* **79**(3), 469–477.

Sibson, R. H. (1990), ‘Rupture nucleation on unfavorably oriented faults’, *Bulletin of the Seismological Society of America* **80**(6A), 1580–1604.

Sigloch, K. (2011), 'Mantle provinces under North America from multifrequencyPwave tomography', *Geochemistry Geophysics, Geosystems* **12**(2).

Sigloch, K., McQuarrie, N. & Nolet, G. (2008), 'Two-stage subduction history under North America inferred from multiple-frequency tomography', *Nature Geoscience* **1**(7), 458–462.

Silver, P. G. (1996), 'Seismic anisotropy beneath the continents: Probing the depths of geology', *Annual review of earth and planetary sciences* **24**(1), 385–432.

Silver, P. G., Gao, S. S., Liu, K. H. & Group, K. S. (2001), 'Mantle deformation beneath southern africa', *Geophysical Research Letters* **28**(13), 2493–2496.

Simpson, R. W. (1997), 'Quantifying anderson's fault types', *Journal of Geophysical Research: Solid Earth* **102**(B8), 17909–17919.

Smith, D., Riter, J. A. & Mertzman, S. A. (1999), 'Water–rock interactions orthopyroxene growth, and Si-enrichment in the mantle: evidence in xenoliths from the Colorado Plateau, southwestern United States', *Earth and Planetary Science Letters* **165**(1), 45–54.

Sobolev, S. V., Zeyen, H., Granet, M., Achauer, U., Bauer, C., Werling, F., Altherr, R. & Fuchs, K. (1997), 'Upper mantle temperatures and lithosphere-asthenosphere system beneath the french massif central constrained by seismic, gravity, petrologic and thermal observations', *Tectonophysics* **275**(1-3), 143–164.

Sobolev, S. V., Zeyen, H., Stoll, G., Werling, F., Altherr, R. & Fuchs, K. (1996), 'Upper mantle temperatures from teleseismic tomography of french massif central including effects of composition, mineral reactions, anharmonicity, anelasticity and partial melt', *Earth and Planetary Science Letters* **139**(1-2), 147–163.

Soto-Cordero, L., Meltzer, A. & Stachnik, J. (2018), 'Crustal structure, intraplate seismicity, and seismic hazard in the mid-atlantic united states', *Seismological Research Letters* **89**(1), 241–252.

Spieker, K., Rondenay, S., Ramalho, R., Thomas, C. & Helffrich, G. (2018), 'Constraints on the structure of the crust and lithosphere beneath the azores islands from teleseismic receiver functions', *Geophysical Journal International* **213**(2), 824–835.

Steckler, M. S., Agostinetti, N. P., Wilson, C. K., Roselli, P., Seeber, L., Amato, A. & Lerner-Lam, A. (2008), 'Crustal structure in the southern apennines from teleseismic receiver functions', *Geology* **36**(2), 155–158.

Stixrude, L. & Lithgow-Bertelloni, C. (2005), 'Thermodynamics of mantle mineralsi. physical properties', *Geophysical Journal International* **162**(2), 610–632.

Stoddard, P. R. & Abbott, D. (1996), 'Influence of the tectosphere upon plate motion', *Journal of Geophysical Research: Solid Earth* **101**(B3), 5425–5433.

Stuart, W. D., Hildenbrand, T. G. & Simpson, R. W. (1997), 'Stressing of the new madrid seismic zone by a lower crust detachment fault', *Journal of Geophysical Research: Solid Earth* **102**(B12), 27623–27633.

Sundberg, M. & Cooper, R. F. (2008), 'Crystallographic preferred orientation produced by diffusional creep of harzburgite: Effects of chemical interactions among phases during plastic flow', *Journal of Geophysical Research* **113**(B12).

Sykes, L. R. (1978), 'Intraplate seismicity, reactivation of preexisting zones of weakness, alkaline magmatism, and other tectonism postdating continental fragmentation', *Reviews of Geophysics* **16**(4), 621–688.

Tang, Y.-J., Zhang, H.-F., Deloule, E., Su, B.-X., Ying, J.-F., Xiao, Y. & Hu, Y. (2012), 'Slab-derived lithium isotopic signatures in mantle xenoliths from northeastern North China Craton', *Lithos* **149**, 79–90.

Tasaka, M., Hiraga, T. & Zimmerman, M. E. (2013), 'Influence of mineral fraction on the rheological properties of forsterite+enstatite during grain-size-sensitive creep: 2. Deformation experiments', *Journal of Geophysical Research: Solid Earth* **118**(8), 3991–4012.

Tenthorey, E. & Cox, S. F. (2006), 'Cohesive strengthening of fault zones during the interseismic period: An experimental study', *Journal of Geophysical Research: Solid Earth* **111**(B9).

Tharimena, S., Rychert, C. A. & Harmon, N. (2016), 'Seismic imaging of a mid-lithospheric discontinuity beneath ontong java plateau', *Earth and Planetary Science Letters* **450**, 62–70.

Thomas, W. A. et al. (2006), 'Tectonic inheritance at a continental margin', *GSA today* **16**(2), 4–11.

Thybo, H. & Perchuć, E. (1997), 'The seismic 8 discontinuity and partial melting in continental mantle', *Science* **275**(5306), 1626–1629.

Tikoff, B., Larson, C. E., Newman, J. & Little, T. (2010), 'Field-based constraints on finite strain and rheology of the lithospheric mantle Twin Sisters, Washington', *Lithosphere* **2**(6), 418–422.

Tommasi, A., Mainprice, D., Canova, G. & Chastel, Y. (2000), 'Viscoplastic self-consistent and equilibrium-based modeling of olivine lattice preferred orientations: Implications for the upper mantle seismic anisotropy', *Journal of Geophysical Research: Solid Earth* **105**(B4), 7893–7908.

Turcotte, D. & Schubert, G. (2014), *Geodynamics*, Cambridge university press.

Tuttle, M. P. (2002), 'The Earthquake Potential of the New Madrid Seismic Zone', *Bulletin of the Seismological Society of America* **92**(6), 2080–2089.

Vinnik, L. (1977), 'Detection of waves converted from p to sv in the mantle', *Physics of the Earth and planetary interiors* **15**(1), 39–45.

Vlahovic, G., Powell, C. A., Chapman, M. C. & Sibol, M. (1998), 'Et1d: New one dimensional p-and s-wave velocity models for the eastern tennessee seismic zone', *Seismological Research Letters* **69**(5), 441–449.

Wagner, L. S., Anderson, M. L., Jackson, J. M., Beck, S. L. & Zandt, G. (2008), 'Seismic evidence for orthopyroxene enrichment in the continental lithosphere', *Geology* **36**(12), 935.

Wang, Z., Kusky, T. M. & Capitanio, F. A. (2018), 'Water transportation ability of flat-lying slabs in the mantle transition zone and implications for craton destruction', *Tectonophysics* **723**, 95–106.

Watt, J. P., Davies, G. F. & O'Connell, R. J. (1976), 'The elastic properties of composite materials', *Reviews of Geophysics* **14**(4), 541–563.

West, J. D., Fouch, M. J., Roth, J. B. & Elkins-Tanton, L. T. (2009), 'Vertical mantle flow associated with a lithospheric drip beneath the great basin', *Nature Geoscience* **2**(6), 439–444.

Whitmeyer, S. J. & Karlstrom, K. E. (2007), 'Tectonic model for the proterozoic growth of north america', *Geosphere* **3**(4), 220–259.

Wilson, D. C., Angus, D., Ni, J. F. & Grand, S. P. (2006), 'Constraints on the interpretation of s-to-p receiver functions', *Geophysical Journal International* **165**(3), 969–980.

Wirth, E. A. & Long, M. D. (2014), 'A contrast in anisotropy across mid-lithospheric discontinuities beneath the central united statesa relic of craton formation', *Geology* **42**(10), 851–854.

Wölbern, I., Rümpker, G., Link, K. & Sodoudi, F. (2012), ‘Melt infiltration of the lower lithosphere beneath the tanzania craton and the albertine rift inferred from s receiver functions’, *Geochemistry, Geophysics, Geosystems* **13**(8).

Wolin, E., Stein, S., Pazzaglia, F., Meltzer, A., Kafka, A. & Berti, C. (2012), ‘Mineral, virginia, earthquake illustrates seismicity of a passive-aggressive margin’, *Geophysical Research Letters* **39**(2).

Wu, Q., Chapman, M. & Beale, J. (2015), ‘The aftershock sequence of the 2011 mineral, virginia, earthquake: Temporal and spatial distribution, focal mechanisms, regional stress, and the role of coulomb stress transfer’, *Bulletin of the Seismological Society of America* **105**(5), 2521–2537.

Wüstefeld, A., Bokelmann, G., Barruol, G. & Montagner, J.-P. (2009), ‘Identifying global seismic anisotropy patterns by correlating shear-wave splitting and surface-wave data’, *Physics of the Earth and Planetary Interiors* **176**(3-4), 198–212.

Xiao, Y., Zhang, H.-F., Fan, W.-M., Ying, J.-F., Zhang, J., Zhao, X.-M. & Su, B.-X. (2010), ‘Evolution of lithospheric mantle beneath the Tan-Lu fault zone eastern North China Craton: Evidence from petrology and geochemistry of peridotite xenoliths’, *Lithos* **117**(1-4), 229–246.

Xu, L., Rondenay, S. & van der Hilst, R. D. (2007), ‘Structure of the crust beneath the southeastern tibetan plateau from teleseismic receiver functions’, *Physics of the earth and planetary interiors* **165**(3-4), 176–193.

Yang, Z., Sheehan, A. & Shearer, P. (2011), ‘Stress-induced upper crustal anisotropy in southern california’, *Journal of Geophysical Research: Solid Earth* **116**(B2).

Yuan, H. & Romanowicz, B. (2010), ‘Lithospheric layering in the north american craton’, *Nature* **466**(7310), 1063.

Yuan, X., Kind, R., Li, X. & Wang, R. (2006), 'The s receiver functions: synthetics and data example', *Geophysical Journal International* **165**(2), 555–564.

Zandt, G. & Humphreys, E. (2008), 'Toroidal mantle flow through the western us slab window', *Geology* **36**(4), 295–298.

Zhan, Y., Hou, G., Kusky, T. & Gregg, P. M. (2016), 'Stress development in heterogenetic lithosphere: Insights into earthquake processes in the new madrid seismic zone', *Tectonophysics* **671**, 56–62.

Zhang, J.-J., Zheng, Y.-F. & Zhao, Z.-F. (2009), 'Geochemical evidence for interaction between oceanic crust and lithospheric mantle in the origin of Cenozoic continental basalts in east-central China', *Lithos* **110**(1-4), 305–326.

Zhang, Q., Sandvol, E. & Liu, M. (2009), 'Tomographic pn velocity and anisotropy structure in the central and eastern united states', *Bulletin of the Seismological Society of America* **99**(1), 422–427.

Zhang, S. & Karato, S.-i. (1995), 'Lattice preferred orientation of olivine aggregates deformed in simple shear', *Nature* **375**(6534), 774–777.

Zoback, M., Apel, R., Baumgätner, J., Brudy, M., Emmermann, R., Engeser, B., Fuchs, K., Kessels, W., Rischmller, H., Rummel, F. & Vernik, L. (1993), 'Upper-crustal strength inferred from stress measurements to 6 km depth in the KTB', *Nature* **365**(6447), 633–635.

Zoback, M. L. (1992), 'Stress field constraints on intraplate seismicity in eastern north america', *Journal of Geophysical Research: Solid Earth* **97**(B8), 11761–11782.

Zoback, M. & Zoback, M. (1989), Chapter 24: Tectonic stress field of the continental United States, *in* 'Geological Society of America Memoirs', Geological Society of America, pp. 523–540.